

Spectral induced polarization of calcite precipitation in porous media

Satoshi Izumoto

Energie & Umwelt / Energy & Environment

Band / Volume 569

ISBN 978-3-95806-614-4

Forschungszentrum Jülich GmbH
Institut für Bio- und Geowissenschaften
Agrosphäre (IBG-3)

Spectral induced polarization of calcite precipitation in porous media

Satoshi Izumoto

Schriften des Forschungszentrums Jülich
Reihe Energie & Umwelt / Energy & Environment

Band / Volume 569

ISSN 1866-1793

ISBN 978-3-95806-614-4

Bibliografische Information der Deutschen Nationalbibliothek.
Die Deutsche Nationalbibliothek verzeichnet diese Publikation in der
Deutschen Nationalbibliografie; detaillierte Bibliografische Daten
sind im Internet über <http://dnb.d-nb.de> abrufbar.

Herausgeber
und Vertrieb: Forschungszentrum Jülich GmbH
 Zentralbibliothek, Verlag
 52425 Jülich
 Tel.: +49 2461 61-5368
 Fax: +49 2461 61-6103
 zb-publikation@fz-juelich.de
 www.fz-juelich.de/zb

Umschlaggestaltung: Grafische Medien, Forschungszentrum Jülich GmbH

Druck: Grafische Medien, Forschungszentrum Jülich GmbH

Copyright: Forschungszentrum Jülich 2022

Schriften des Forschungszentrums Jülich
Reihe Energie & Umwelt / Energy & Environment, Band / Volume 569

D 93 (Diss. Stuttgart, Univ., 2021)

ISSN 1866-1793
ISBN 978-3-95806-614-4

Vollständig frei verfügbar über das Publikationsportal des Forschungszentrums Jülich (JuSER)
unter www.fz-juelich.de/zb/openaccess.



This is an Open Access publication distributed under the terms of the [Creative Commons Attribution License 4.0](https://creativecommons.org/licenses/by/4.0/),
which permits unrestricted use, distribution, and reproduction in any medium, provided the original work is properly cited.

Acknowledgements

This PhD work was funded by European Union's Horizon 2020 research and innovation programme under the Marie Skłodowska-Curie Grant Agreement N°722028 to the project entitled "ENIGMA (European training Network for In situ imaGing of dynaMic processes in heterogeneous subsurfAce environments)". This project gave me the opportunity to work in the Agrosphere (IGB-3), Institute of Bio- and Geosciences, Forschungszentrum Jülich, as a host institute and in Geosciences Rennes, University of Rennes 1 as a secondment institute.

First, I would like to express my sincere gratitude to my supervisor, Prof. Dr. Johan Alexander (Sander) Huisman for his warm and detailed support and guidance throughout my PhD, ranging from research direction to the working environment. Sander has never hesitated to spend long times for discussion, regularly once in a week and often more, that made me feel sure about what I should do. Sander also gave me appropriate support to do what I want and helped me with all the writing. Thanks to Sander's long and hard thinking, I was able to work quite comfortably.

My sincere gratitude also goes to Prof. Dr. Tanguy Le Borgne for his supervision and extraordinary support in Rennes. Tanguy connected me and some specialists, so that I was able to get help for specific issues, learn efficiently and save time. Tanguy also shared his knowledge of fluid mechanics with me, which is one of the core topics in this thesis. Tanguy advised me to keep thinking about research, which has been motivating me a lot.

I would like to thank the team members in Jülich, Dr. Egon Zimmermann, Odilia Esser, Dr. Franz-Hubert Haegel, the computer technicians in IGB-3, and the technicians in the Central Institute of Engineering, Electronics and Analytics (ZEA-2). They helped me a lot with practical matters, such as fabricating the experimental materials, sending packages, setting up experiments, getting materials, buying stuff and computer simulations. I could not do anything without them in practice. Especially, Egon helped me with most of the design of 2D millifluidic set-up and the initial setup of the simulations, which also helped me to obtain solid knowledge of SIP from him. In fact, it was one of the best experiences in my PhD to learn from him.

I would also like to thank the team members in Geosciences Rennes, Asst. Prof. Dr. Yves Méheust, Dr. Joris Heyman, Francesco Gomez, Dr. Julien Farasin, Dr. Romain Laniel and Dr. Hervé Tabuteau. Joris and Francesco spent a lot of time with me in the laboratory and we discussed a lot. They shared their knowledge, such as coding, image processing, setting up of experiments and the way to use technical tools, with me. They have improved my way of thinking about how to solve issues in research. Yves kept caring about image processing and how I can stay in Rennes comfortably by solving many practical issues. Julien taught me how to work on microbiology, which was necessary for my future research.

Acknowledgement

Romain helped with using profilometer that was used in Chapter 4, and Hervé helped with the fabrication of the 2D porous medium.

I also thank Dr. Cyprien Soullain in CNRS Orleans Campus, Dr. Adrian Mellage in University of Tuebingen, Kevin de Vriendt, who is a PhD student in Spanish National Research Council and Dr. Yuxin Wu in Lawrence Berkeley National Laboratory. They guided me with their very solid specialities. Thanks to that, I was able to learn effectively and to make a progress in short time. Cyprien helped me to appropriately use OpenFOAM from a numerical and fluid mechanical point of view. Adrian helped me to initiate experimental work for SIP and microbiology, and to consider the future study. Kevin taught me how to use chemiluminescence, which was the key technical aspect to study mixing and reaction in Chapter 5. Yuxin gave me the key preliminary experimental results, which gave the essential idea for the column experiments in Chapter 3.

I would like to thank Prof. Dr. Harry Vereecken and Prof. Dr. Jan Vanderborght for maintaining good working condition for PhD students in IBG 3 institute in Jülich. Harry made me think about something fundamental in short questions many times, through the discussions in the PhD reports and in PhD seminars. I am also grateful to Prof. Dr. Frédéric Nguyen in Université de Liège for his quick and thorough review of this thesis. That helped me a lot to make a next step in my career.

Finally, I thank all my friends in Jülich and in Rennes and the ENIGMA members. I was surprised to see how welcoming they are when I arrived in Europe. Even when I was not used to talking in English at the beginning of PhD, they took care of me and tried to communicate with me. I felt relaxed to stay with them during lunch time or dinner time, in weekends and in the office. That helped me to keep a good mind condition even when I was struggling with some difficulties in my work. I came to like my stay in Europe thanks to my friends.

Abstract

Precipitation and dissolution dynamics of calcite in response to variations in groundwater pH and alkalinity are important in a range of subsurface engineering applications. In the context of geotechnical engineering and subsurface remediation applications, induced calcite precipitation is widely used. The effectiveness of induced calcite precipitation is typically investigated by measuring hydraulic pressure, analysing biochemical properties of sampled solution, and cone penetration tests. However, these methods are spatially and temporally limited, expensive and laborious. Geophysical methods have potential to overcome these limitations. In particular, Spectral Induced Polarization (SIP) measurements have been shown to be sensitive to calcite precipitation. However, previous experimental studies showed inconsistent SIP responses and have not explored what controls the SIP response of calcite. In this context, the overall aim of this thesis was to better understand how spatially variable and temporally dynamic calcite precipitation processes affect the SIP response.

In a first step, the effect of solute concentration on the SIP response of calcite precipitation was investigated by a four-phase experiment with SIP measurements on a column filled with sand. In phase I, Na_2CO_3 and CaCl_2 solutions were co-injected, which resulted in a calcite precipitation front that increased the imaginary part of the electrical conductivity (σ''). In phase II, several diluted (but still oversaturated) solutions were injected into the sample with calcite precipitation from phase I, which resulted in a decrease of σ'' . The results suggested that the σ'' associated with calcite depends more strongly on the solute conductivity than in the case of sand and sandstone. In phase III, the solutions from phase I were injected first and then the injection was stopped. Since calcite precipitation continued after stopping the flow, this resulted in a decrease of the solute concentration in the mixing zone and an associated decrease of σ'' . In phase IV, the injection rate of the Na_2CO_3 solution was reduced relative to that of the CaCl_2 solution. This shifted the mixing zone away from the calcite precipitation front and again the σ'' decreased. These results clearly suggested that the SIP response of calcite is sensitive to the solute concentration near the precipitates.

In a second step, a novel laboratory experimental setup was developed to directly visualize calcite precipitation processes while making SIP measurements. The setup consisted of a transparent millifluidic cell with a 2D porous media and current and potential electrodes for SIP measurements. One camera was used to monitor calcite precipitation processes in the entire measurement region and a second camera on a motorized stage was used to monitor the development of individual crystals using high-zoom images. This novel set-up was then used to investigate how spatial variation and temporal dynamics of calcite precipitation affect the SIP response. Calcite precipitation was induced by co-injecting the same Na_2CO_3 and CaCl_2 solutions as in the column experiment and the SIP response was monitored in three distinct regions. The image analysis and SIP measurements suggested two distinct

Abstract

phases in the experimental results. In the first phase, the mass of calcite precipitates increased due to the creation of a wall-like calcite precipitation front along the mixing front. However, the σ'' in the three regions did not substantially increase. In the second phase, the mass of calcite increased only slightly (2%) in the area with the wall-like calcite precipitation, but the σ'' strongly increased and almost doubled. Key characteristics of the SIP response during the second phase were interpreted using electric field simulations based on the imaged distribution of calcite precipitation. It was found that the observed negative values for σ'' could be explained by variations in the strength of the polarization along the calcite precipitation. It was also observed that the peak frequency of σ'' was higher for the upstream measurement region, which was related to the shape of the calcite precipitation front. Based on the experimental results, it was hypothesized that the closing of the gap space between the top of the calcite precipitation and the inner wall of the sample holder (i.e. the height of the calcite precipitation) largely determined the increase of σ'' . This was confirmed by simulations using a simplified electrical circuit model. This model also suggested that Maxwell-Wagner polarization could have played an important role in determining σ'' . Overall, it was found that the spatial distribution and temporal dynamics of calcite precipitation instead of the total mass of calcite were the important factors that determined the SIP response.

In a third and final step, the understanding of the SIP response of calcite precipitation in porous media was supported by improving the understanding of chemical reactions at stagnation points that widely occur in flow fields within porous media. For this, experiments using the millifluidic set-up and pore-scale modelling were used. In particular, the scaling of the width of the reaction zone, the maximum reaction rate and the reaction intensity were investigated as a function of the Péclet (Pe) and Damköhler (Da) number. First, scaling laws at the stagnation point were theoretically derived by applying mixing theory to a bimolecular reaction system. It was found that the width of the reaction zone scales following $Pe^{-1/6} Da^{-1/3}$, the maximum reaction rate scales following $Pe^{2/3} Da^{1/3}$ and the reaction intensity scales following $Pe^{1/2}$. Next, reactive transport experiments were performed using the millifluidic set-up. The results showed that these scaling laws were valid for a Hele-Shaw cell configuration without porous media. The scaling laws were also globally applicable in the presence of a 2D porous medium, although considerable fluctuations and compression were observed in the experimental results. In relation to the SIP response of calcite, these results suggested that the temporal dynamics of the SIP response will be a function of Pe following the scaling of the maximum reaction rate ($\propto Pe^{2/3}$) because this reaction rate controls the closing of the pore space.

Overall, this thesis provides five key findings about the SIP response associated with spatially variable and temporally dynamic calcite precipitation. First, the solute concentration near the calcite precipitation largely affects the SIP response. Second, the closing of the pore space largely increases the SIP response. Third, the spatial distribution of the calcite precipitation results in different peak frequencies in different measurement regions and a negative σ'' . Fourth, Maxwell-Wagner polarization

plays an important role in determining the strength of the SIP response. Finally, the temporal dynamics of the SIP response will be a function of Pe following the scaling of the maximum reaction rate ($\propto Pe^{2/3}$) because this reaction rate controls the closing of the pore space. Taken together, these five findings describe key factors controlling the SIP response of calcite, and help to understand previously reported inconsistent experimental results.

Zusammenfassung

Die Ausfällungs- und Auflösungs-dynamik von Kalzit als Reaktion auf Schwankungen des pH-Werts und der Alkalinität des Grundwassers sind für eine Reihe von Anwendungen wichtig. Im Zusammenhang mit Geotechnik und Untergrundsanie rung wird die induzierte Kalzitausfällung häufig eingesetzt. Die Effektivität der induzierten Ausfällung wird typischerweise durch die Messung des hydraulischen Drucks, die Analyse der biochemischen Eigenschaften der beprobten Lösung und durch Drucksondierungen untersucht. Diese Methoden sind jedoch räumlich und zeitlich eingeschränkt, teuer und aufwändig. Geophysikalische Methoden haben das Potenzial, diese Einschränkungen zu überwinden. Insbesondere haben sich Messungen der spektralen induzierten Polarisation (SIP) als empfindlich gegenüber Kalzitniederschlag erwiesen. Frühere experimentelle Studien zeigten jedoch inkonsistente SIP-Messergebnisse und haben nicht untersucht, was die SIP-Antwort von Kalzit kontrolliert. In diesem Zusammenhang war es das übergeordnete Ziel dieser Arbeit, besser zu verstehen, wie räumlich variable und zeitlich dynamische Kalzitausfällungsprozesse SIP-Messungen beeinflussen.

In einem ersten Schritt wurde der Einfluss der gelösten Konzentration auf die Antwort des SIP-Signals des Kalzitniederschlags in einem Vier-Phasen-Experiment in einer mit Sand gefüllten Säule untersucht. In Phase I wurden Na_2CO_3 - und CaCl_2 -Lösungen gemeinsam injiziert, was zu einer Kalzitniederschlagsfront führte, die den Imaginärteil der elektrischen Leitfähigkeit (σ'') erhöhte. In Phase II wurden mehrere verdünnte (aber immer noch übersättigte) Lösungen in die Probe mit dem Kalzitniederschlag aus Phase I injiziert, was zu einer Abnahme von σ'' führte. Die Ergebnisse deuteten darauf hin, dass das mit Kalzit verbundene σ'' stärker von der elektrischen Leitfähigkeit der Lösung abhängt als im Fall von Sand und Sandstein. In Phase III wurden zuerst die Lösungen aus Phase I injiziert, dann wurde die Injektion gestoppt. Da die Kalzitausfällung nach dem Stoppen der Strömung weiter fortschritt, führte dies zu einer Abnahme der gelösten Konzentration in der Mischzone und einer damit verbundenen Abnahme von σ'' . In Phase IV wurde die Injektionsrate der Na_2CO_3 -Lösung relativ zu der CaCl_2 -Lösung reduziert. Dadurch verlagerte sich die Mischzone von der Kalzitniederschlagsfront weg und σ'' nahm wiederum ab. Diese Ergebnisse deuten eindeutig darauf hin, dass die SIP-Antwort von Kalzit empfindlich auf die Konzentration der gelösten Stoffe in der Nähe des Kalzitniederschlags reagiert.

In einem zweiten Schritt wurde ein neuartiger Labor-Versuchsaufbau entwickelt, um Kalzit-Ausfällungsprozesse bei der Durchführung von SIP-Messungen direkt sichtbar zu machen. Der Aufbau bestand aus einer transparenten millifluidischen Zelle mit einem 2D-porösen Medium und Strom- und Potentialelektroden für SIP-Messungen. Eine erste Kamera wurde zum Monitoring von Kalzit-Ausfällungsprozessen in der gesamten Messregion eingesetzt. Eine zweite Kamera auf einem motorisierten Tisch wurde zur Beobachtung der Entwicklung von Einzelkristallen mit starker Vergrößerung genutzt. Mit diesem neuartigen Aufbau wurde dann untersucht, wie räumliche Variation

und zeitliche Dynamik des Kalzitniederschlags die SIP-Antwort beeinflussen. Der Kalzitniederschlag wurde durch Ko-injektion der gleichen Lösungen wie im Säulenexperiment (Na_2CO_3 - und CaCl_2 -Lösungen) induziert, und die SIP-Antwort wurde in drei verschiedenen Regionen beobachtet. Die Bildanalyse und die SIP-Messungen ließen auf zwei verschiedene Phasen in den experimentellen Ergebnissen schließen. In der ersten Phase nahm die Masse des Kalzitniederschlags aufgrund der Bildung einer wandartigen Kalzitniederschlagsfront entlang der Mischungsfront zu. Die Werte von σ'' in den drei Regionen nahmen jedoch nicht wesentlich zu. In der zweiten Phase nahm die Kalzitmasse in dem Gebiet mit dem wandartigen Kalzitniederschlag nur geringfügig (2%) zu, aber die σ'' -Werte nahmen stark zu und verdoppelten sich fast. Schlüsselmerkmale der SIP-Antwort während der zweiten Phase wurden mit Hilfe von Simulationen des elektrischen Feldes auf der Grundlage der beobachteten Verteilung des Kalzitniederschlags interpretiert. Es wurde festgestellt, dass die beobachteten negativen Werte für σ'' durch Variationen in der Stärke der Polarisation entlang der Kalzitniederschlagsfront erklärt werden können. Es wurde auch beobachtet, dass die Frequenz am Maximum von σ'' für die stromaufwärts gelegene Messregion höher war, was mit der Form der Kalzitniederschlagsfront zusammenhing. Basierend auf den experimentellen Ergebnissen wurde die Hypothese aufgestellt, dass das Schließen des Spaltes zwischen dem oberen Rand der Kalzitniederschlagsfront und der Innenwand des Probenhalters (d. h. die Höhe des Kalzitniederschlags) den Anstieg von σ'' weitgehend bestimmt. Dies wurde durch Simulation mit einem vereinfachten elektrischen Schaltungsmodell bestätigt. Dieses Modell legte auch nahe, dass die Maxwell-Wagner-Polarisation eine wichtige Rolle bei der Bestimmung von σ'' gespielt haben könnte. Insgesamt wurde festgestellt, dass die räumliche Verteilung und die zeitliche Dynamik des Kalzitniederschlags anstelle der Gesamtmasse des Kalzits die wichtigen Faktoren waren, die die SIP-Antwort bestimmten.

In einem dritten und letzten Schritt wurde das Verständnis der SIP-Antwort auf den Kalzitniederschlag in porösen Medien durch die Verbesserung des Verständnisses chemischer Reaktionen an Staupunkten unterstützt, die in den Strömungsfeldern in porösen Medien häufig auftreten. Hierzu wurden Experimente im millifluidischen Aufbau und porenskalige Modellierung genutzt. Insbesondere wurde die Skalierung der Breite der Reaktionszone, der maximalen Reaktionsrate und der Reaktionsintensität als Funktion der Péclet- (Pe) und der Damköhler-Zahl (Da) untersucht. Zunächst wurden die Skalierungsgesetze am Staupunkt theoretisch abgeleitet, indem die Mischungstheorie auf ein bimolekulares Reaktionssystem angewendet wurde. Es wurde festgestellt, dass die Breite der Reaktionszone nach $Pe^{-1/6}Da^{-1/3}$ skaliert, die maximale Reaktionsgeschwindigkeit nach $Pe^{2/3}Da^{1/3}$ und die Reaktionsintensität nach $Pe^{1/2}$. Anschließend wurden Experimente zum reaktiven Transport mit dem millifluidischen Aufbau durchgeführt. Die Ergebnisse zeigten, dass diese Skalierungsgesetze für eine Hele-Shaw-Zellenkonfiguration ohne poröse Medien gültig waren. Die Skalierungsgesetze waren auch bei Vorhandensein eines 2D-porösen Mediums global anwendbar, obwohl in den experimentellen Ergebnissen erhebliche Schwankungen beobachtet wurden. In Bezug

auf die SIP-Antwort von Kalzit legen diese Ergebnisse nahe, dass die zeitliche Dynamik der SIP-Antwort eine Funktion von Pe sein wird, die der Skalierung der maximalen Reaktionsrate ($\propto Pe^{2/3}$) folgt, da diese Reaktionsrate das Schließen des Porenraums kontrolliert.

Insgesamt liefert diese Arbeit fünf wichtige Erkenntnisse über die SIP-Antwort im Zusammenhang mit räumlich variablen und zeitlich dynamischen Kalzitniederschlägen. Erstens beeinflusst die gelöste Konzentration in der Nähe des Kalzitniederschlags weitgehend die SIP-Antwort. Zweitens erhöht im Wesentlichen das Schließen des Porenraums die SIP-Antwort. Drittens führt die räumliche Verteilung des Kalzitniederschlags zu unterschiedlichen Frequenzen für die Maxima von σ in verschiedenen Messregionen und zu einem negativen σ . Viertens spielt die Maxwell-Wagner-Polarisation eine wichtige Rolle bei der Bestimmung der Stärke der SIP-Antwort. Schließlich wird die zeitliche Dynamik der SIP-Antwort eine Funktion von Pe sein, die der Skalierung der maximalen Reaktionsrate ($\propto Pe^{2/3}$) folgt, da diese Reaktionsrate das Schließen des Porenraums kontrolliert. Zusammengefasst beschreiben diese fünf Erkenntnisse Schlüsselfaktoren, die die SIP-Antwort von Kalzit steuern, und helfen zuvor berichtete widersprüchliche experimentelle Ergebnisse zu verstehen.

Contents

Acknowledgements.....	i
Abstract.....	iii
Zusammenfassung.....	vii
Contents	xi
List of figures.....	xiii
List of tables.....	xvii
List of abbreviations	xviii
1. Introduction.....	1
1.1. Motivation.....	1
1.2. Spectral induced polarization and biochemical reactions	2
1.3. Chemical reactions and mixing theory.....	4
1.4. Aims and organization of thesis.....	5
2. Theory of spectral induced polarization.....	9
2.1. SIP measurements.....	9
2.2. SIP measurement system	11
2.3. Polarization mechanisms	14
2.4. Grain polarization model	15
2.5. Empirical models to describe complex electrical conductivity.....	19
3. Effect of solute concentration on the SIP response of calcite precipitation.....	21
3.1. Methods.....	22
3.2. Results and discussion	26
3.3. Conclusions.....	34
4. Millifluidic experiments to understand SIP response during calcite precipitation	35
4.1. Materials and methods	36
4.1.1. Sample holder	36
4.1.2. 2D porous media	38
4.1.3. Visualization of pore-scale processes	39
4.1.4. Experimental procedure	40

Contents

4.1.5. Image processing.....	42
4.1.6. Simulation.....	43
4.2. Results and discussion	44
4.2.1. Precipitation process	44
4.2.2. SIP response.....	50
4.2.3. SIP response of calcite precipitation in homogeneous solution.....	54
4.2.4. Electrical field simulations.....	57
4.3. Discussion.....	61
4.4. Conclusions.....	64
5. Enhancement of mixing-induced reactions at stagnation points in pore scale flow fields.....	67
5.1. Theory.....	68
5.1.1. Derivations for $Da > 1$ regime	70
5.1.2. Derivations for $Da < 1$ regime	71
5.2. Experimental setup to investigate reaction dynamics	72
5.3. Numerical simulations	74
5.4. Results and discussion	75
5.4.1. Conservative mixing	75
5.4.2. Reactive mixing	77
5.4.3. Stretching and compression	79
5.5. Conclusions.....	82
6. Conclusions and Outlook.....	83
6.1. Conclusions.....	83
6.2. Outlook	87
References.....	95

List of figures

Figure 2.1. (a) Schematic overview of SIP measurement set-up with electrodes in yellow, (b) the phase shift between the injected current and measured voltage, (c) typical change in real and imaginary part of the electrical conductivity as a function of frequency.....	10
Figure 2.2. Schematic illustration of the SIP measurement system of Zimmermann et al. (2008).....	11
Figure 2.3. Cross-section of triaxial cable connected to an amplifier and the ground.....	12
Figure 2.4. Schematic illustration showing the ratio of the distances to ensure a homogeneous potential field at the position of the potential electrodes.....	12
Figure 2.5. Schematic illustration of capacitances between the sample and the surrounding environment.....	13
Figure 2.6. (a) Polarization at the surface of potential electrode (b) retracted potential electrode, which is not polarized.....	13
Figure 2.7. Schematic showing input capacitance of the amplifiers, position of the potential measurement and the position of the estimated potential within the sample.....	14
Figure 2.8. Summary of possible polarization mechanisms.....	15
Figure 2.9. (a) Electric double layer (EDL) of calcite (Al Mahrouqi et al., 2017) (b) Illustration of streaming potential measurement (Li et al., 2016).....	17
Figure 2.10. Grain polarization associated with Stern layer and diffuse layer (Leroy et al., 2008).....	18
Figure 3.1. Schematic drawing of the column with electrode positions and a photo of the column at day 12. The injection tube for Na ₂ CO ₃ was bent to inject solution in the middle between the potential electrodes.....	25
Figure 3.2. Simulated streamlines of Na ₂ CO ₃ and CaCl ₂ solution in the entire column and a close-up of the area near the injection tube for (a) phase I, (b) phase II, and (c) phase IV.....	26
Figure 3.3. Change in (a) σ' and (b) σ'' caused by calcite precipitation during the first 12 days of phase I. Open symbols represent the measured values in the initial condition before starting the injection.....	27
Figure 3.4. Change in (a) σ' and (b) σ'' when the column was flushed with solution pairs with different saturation index (solution pair 2-5 in Table 3.2) in phase II.....	29
Figure 3.5. Relationship between σ_w and σ'' in phase II for different frequencies by assuming that the injected solutions were (a) reacting slowly and thus not in equilibrium with calcite and (b) reacting quickly and thus in equilibrium with calcite. The associated fits of Eq. (7) to the measured values are also presented.....	30
Figure 3.6. The development of (a) σ' and (b) σ'' as a function of time when solute injection was stopped in phase III. Open symbols represent the measured values before flow was stopped at t=0 h. Darker colour represents longer elapsed time. The grey symbols represent measured values after re-establishment of the condition at the start of this phase by injecting solution pair 2 of Table 3.2.....	31
Figure 3.7. Change in σ'' at 1 kHz over time after stopping injection of both CaCl ₂ and Na ₂ CO ₃ solution in phase III.....	31
Figure 3.8. Development of (a) σ' and (b) σ'' when the injection rate of the Na ₂ CO ₃ solution was reduced relative to that of the CaCl ₂ solution. Darker colour represents longer elapsed time.....	32
Figure 4.1. Overview of the experimental setup. (a) Entire setup including 1) overview camera, 2) high-zoom camera, 3,4) 3-axis stage, 5) 2-axis moving table, 6) lenses, 7) millifluidic set-up, 8) backlight, (b) sample holder with porous media and electrodes, (c) plan view of the middle plate of sample holder, and (d) 2D porous media made of PDMS.....	36
Figure 4.2. Cross-section of the sample holder in (a) flow direction and (b) perpendicular to the flow direction. The dimensions of the top plate, middle plate, bottom plate, PDMS flat plate and 2D porous media are given, and key features of the sample holder are also indicated. Please note that the vertical dimension is not to scale.....	37

Figure 4.3. Cumulative distribution function for grain diameter, pore throat size and pore diameter size for the 2D porous media and (b) top view of 2D porous media (black: pore space, white: pillars)..... 39

Figure 4.4. Digital images taken at different times for the entire measurement area (left column), a selected area along the calcite precipitation front in a composite image (center column) and calcite crystals in high-zoom images (right column)..... 45

Figure 4.5. Microscopic images of calcite precipitates (a) top view with the focus set on the bottom of the 2D porous medium, (b) top view with the focus set on the top of the calcite precipitation and (c) side view..... 45

Figure 4.6. Relationship between image grey level and the height of the precipitation from the profilometer and the fitted calibration curve to calculate height of precipitation from image grey level with 95% prediction intervals. 46

Figure 4.7 (a) Change in mass of precipitation over time in the entire measurement zone. (b) Change in mass of precipitation in the upper (near potential electrodes) and lower half of the measurement setup in Figure 4.4. 47

Figure 4.8 (a) Cumulative volume of calcite precipitation at a given height as a function of time. (b) Cumulative volume of calcite precipitation at a given height as a function of time normalized with the volume at 20 h..... 47

Figure 4.9. Spatial distribution of the development of calcite precipitation before 20 h as a function of distance along the precipitation front for the a) upper and b) lower branch of the precipitation front. The lines indicate the time required to reach a given percentage of the volume of calcite precipitation at 20 h. 48

Figure 4.10. High-zoom images that exemplify calcite wall extended in downstream direction (a,b) and continued vertical development of the calcite wall (c). 49

Figure 4.11. Conceptual model to explain reduced speed of calcite precipitation during the formation of the calcite wall. The colours represent the zone with CaCl_2 solution (blue), the zone with Na_2CO_3 solution (yellow), calcite wall (grey) and the mixing zone (orange). 49

Figure 4.12. High-zoom images showing calcite crystals in different parts of the measurement domain. 50

Figure 4.13. SIP response as a function of time for the three different measurement zones in experiment I. 52

Figure 4.14. SIP response as a function of time for the three different measurement zones in the duplicate experiment II. 53

Figure 4.15. Key characteristics of the SIP response as a function of time for the three measurement zones: (a) peak frequency, (b) σ'' at peak frequency, (c) σ' at 1 Hz and (d) σ' at 45 kHz. 54

Figure 4.16. Change in normalized grey level in the entire measurement zone in the experiment with intermediate injections with MgCO_3 solution (blue zones). 55

Figure 4.17. SIP response as a function of time for the three measurement zones in the experiment with intermediate injection of MgCO_3 solution. 56

Figure 4.18. SIP response after the first and second injection of MgCO_3 solution..... 56

Figure 4.19. Simulation domains for three different scenarios: (a) continuous calcite precipitation front, (b) discontinuous calcite precipitation front, and (c) spatially variable complex electrical conductivity of calcite. The yellow colour represents the background and the blue colour represents the distribution of calcite precipitation. 58

Figure 4.20. The simulated SIP responses in different measurement zones depending on chargeability and $R\sigma$ value. 59

Figure 4.21. Simulated SIP response for different measurement zones for the three simulation scenarios shown in Figure 4.19: (a) continuous calcite precipitation front, (b) discontinuous calcite precipitation front, and (c) spatially variable complex electrical conductivity of calcite... 60

Figure 4.22. The normalized imaginary part of the potential field for different simulation scenarios: (a) continuous precipitation front with $m = 0.995$ and $R\sigma = 0.9$ and (b) continuous precipitation

front with $m = 0.995$ and $R\sigma = 0.005$ (c) discontinuous precipitation front at 193 Hz, and (d) heterogeneous complex electrical properties of calcite at 233 Hz.	61
Figure 4.23. (a) Conceptual model to explain Maxwell-Wagner polarization associated with the calcite precipitation front, (b) equivalent electric circuit of the conceptual model, and (c) simulated σ' and σ'' as a function of the height of the calcite precipitation front.	63
Figure 5.1. Schematic illustration showing (a) deformation of small fluid elements near the stagnation point where blue and orange represent different solutes (b) the concentration profile of species A (orange) and B (blue) near the stagnation point. The black line represents the conservative component F. The green line represents the linear approximation of the error function (F) near the stagnation point.	68
Figure 5.2. (a) Illustration of the overall experimental setup, (b) Cross-section of the millifluidic set-up, (c) Example of a photo of the porous medium taken during the conservative tracer experiment.	73
Figure 5.3. (a) Measured concentration profiles and fitted curves for conservative tracer experiments in the Hele-Shaw cell configuration and (b) measured concentration gradient profiles (dots) and fitted curves (lines) for conservative tracer experiments in the porous medium.	75
Figure 5.4. (a) Scaling of the conservative mixing width as a function of Pe for Hele-Shaw cell and porous medium experiments. (b) Calculated ratio of the compression rate in the porous medium compared to the Hele-Shaw cell based on the measured Bachelor scale.	76
Figure 5.5. Examples of images around the stagnation point at the maximum Pe for reactive tracer experiments and the measured lines for analysis of the stagnation points in the (a) Hele-Shaw cell and (b) porous medium (both $Pe = 14$). The scale bars show the normalized reaction rate.	77
Figure 5.6. Reaction rate profiles across the stagnation points (dots) for different flow conditions in the (a) Hele-Shaw cell and (b) porous medium. Fitted Gaussian curves are shown as continuous lines.	77
Figure 5.7. Scaling of the reaction front in the chemiluminescence experiments as a function of Pe . (a) Width of the reaction front, (b) maximum reaction rate normalized by the depth of the images (c) Reaction intensity normalized by the depth of the images.	78
Figure 5.8. Calculated ratio of the compression rate in the porous medium and the Hele-Shaw cell for (a) stagnation point 1 and (b) stagnation point 2.	79
Figure 5.9. Simulated streamlines and velocity fields normalized by the total injection flow velocity in the (a) Hele-Shaw cell and (b) porous medium near the stagnation points. The yellow circles indicate the stagnation points. In addition, the calculated compression rate field around stagnation points normalized by the total injection flow velocity is shown for the (c) Hele-Shaw cell and (d) porous medium, where negative compression rates indicate stretching. The yellow dotted lines represent the position where the concentration profiles for the two stagnation points were determined in the experiments. The yellow lines around the grains indicate the absence of a calculated compression rate. The white squares represent the positions where the average compression rate was calculated for the reactive transport experiment.	80
Figure 5.10. (a) Calculated compression rate based on the simulations at the stagnation point. (b) Calculated ratio of compression rate relative to Hele-Shaw cell.	81
Figure 5.11. (a) The velocity field in the Hele-Shaw cell and (b-d) in the porous medium with different positions of the point injection. The background flow is from left to right. The point injection is located at the center of the high flow velocity zone. The white bar represents 5 mm.	81
Figure 6.1. Photos of porous media (a) at the start of the experiment and (b) just before flushing.	91
Figure 6.2. Change in (a) σ'' and (b) normalized grey value of the porous media. The dotted line indicates the time when the millifluidic set-up was flushed. It should be noted that the SIP measurements showed a sudden jump in σ'' at 22 hours due to an unknown error.	91
Figure 6.3. SEM images of flushed porous media after the experiment (a) near the grain and (b) on the bottom of the sample holder where some bacteria streamers can be observed.	91

Figure 6.4. Example of pore scale electric field simulation using OpenFOAM, where electric current was injected from right boundary. (a) red part has non-zero imaginary conductivity, representing the shape of calcite precipitation front. (b) Simulated electric current flow, where brighter color represents higher current. Simulated (c) real part and (d) imaginary part of the electric potential where the red color represents larger absolute values. 94

List of tables

Table 3.1. Summary of previous researches about SIP response of calcite precipitation in laboratory experiments. Increase in imaginary part of the conductivity and solute concentrations used in the experiments are shown.....	22
Table 3.2. Electrical conductivity, pH and concentration of injected solution pairs. Solution pair 1 with a saturation index of 3.18 was used to generate calcite precipitation until day 12, and solution pair 2 with a saturation index of 3.18 was used for rest of the experiments.	25

List of abbreviations

SIP	Spectral induced polarization
Pe	Péclet number
Da	Damköhler number

Chapter 1

Introduction

1.1. Motivation

Precipitation and dissolution dynamics of calcite in response to variations in groundwater pH and alkalinity are important in a range of subsurface engineering applications. In the context of geotechnical engineering and subsurface remediation applications, calcite precipitation can have both positive and negative effects. A range of studies have reported undesirable effects of calcite precipitation associated with well clogging, i.e. the reduction of hydraulic conductivity around wells. This leads to the need for regular well redevelopment in aquifer storage and recovery applications (Pavelic et al., 2007) and reduces the accessible depth of a well for fluids in geothermal applications (Regenspurg et al., 2015). Calcite precipitation has also been reported to affect the working lifetime of permeable reactive barriers using Fe^0 (Liang et al., 2003). Besides these undesirable effects of calcite precipitation, beneficial effects of calcite precipitation have also been widely explored (DeJong et al., 2013). For example, field tests with microbially-induced calcite precipitation have demonstrated its potential for bioremediation (Fujita et al., 2008, 2010), stabilization of soil (Burbank et al., 2011; Gomez et al., 2015) and the reduction of liquid permeability (Cuthbert et al., 2013; Phillips et al., 2016). In many of these studies, the extent or effectiveness of calcite precipitation was monitored by measuring hydraulic pressure, analysing biochemical properties of sampled solution, or with cone penetration tests. However, these methods are spatially and temporally limited, expensive and laborious. Geophysical methods that make use of non-invasive electromagnetic and seismic wave propagation with sensors deployed on the boundary of the area of interest have potential to overcome these limitations. Some studies have used seismic methods for real-time and non-destructive monitoring of calcite precipitation (e.g. Mujah et al., 2017; Saneiyani et al., 2020). However, seismic methods are less suitable for long-term monitoring in field applications because this method is not easily automated and involves substantial manual procedures. Wu et al. (2010) showed that Spectral Induced Polarization (SIP), which determines the complex electrical conductivity in the mHz to kHz frequency range, is sensitive to calcite precipitation. Compared to seismic monitoring of calcite precipitation, SIP measurements have the advantage that

1. Introduction

they are able to provide a higher spatial and temporal resolution, and additionally are suitable for long term monitoring due to the relatively straightforward automation (Slater & Sandberg, 2000).

1.2. Spectral induced polarization and biochemical reactions

SIP determines the complex electrical conductivity by measuring the amplitude and phase of the voltage within a sample while injecting a sinusoidal current with a known frequency in the mHz to kHz frequency range (Kemna et al., 2012). The real part of the electrical conductivity represents the sample's resistivity, while the imaginary part of the electrical conductivity is related to the sample's ability to temporally store electric charge. Various laboratory studies have explored the possibility to monitor dynamic biochemical reactions in porous media using SIP measurements in biotic and abiotic conditions. In abiotic conditions, previous studies have mainly focused on iron mineral precipitation. Several studies showed a strong relationship between the SIP response and the amount, specific surface area and transformation of iron minerals (Slater et al., 2005, 2006; Wu et al., 2005). Follow-up studies explored the possibility of detecting the type of iron minerals, the mineral size and different processes associated with iron minerals. For example, Ntarlagiannis et al. (2010) observed an increase in SIP response due to the secondary formation of iron sulfide precipitation in sand. Placencia-Gomez et al. (2013) found that oxidation of iron sulfide decreased the SIP response. The mechanism behind the strong polarization response of iron precipitation was clarified by Hubbard et al. (2014). In this study, the SIP response of mixtures of sand and magnetite in contact with solutions with redox-active (Fe^{2+}) or redox-inactive ions (Ni^{2+} , Ca^{2+}) was measured. They found that the SIP response was insensitive to the surface charge, but it was sensitive to redox reactions. Thus, it was inferred that the polarization contribution of migration of charges within the magnetite particle dominates the contribution from the electrical double layer. In addition to iron minerals, there are also studies that investigated the SIP response of calcite precipitation although mechanistic understanding is still limited in this case. Wu et al. (2010) were the first to report a clear SIP response associated with calcite precipitation in a laboratory study. Several follow-up studies have reported much smaller and less clear SIP responses to calcite precipitation (Saneiyan et al., 2018; Zhang et al., 2012). It is clear that more research is required to clarify what environmental conditions or mineral properties determine the SIP response of calcite precipitation.

In biotic conditions, a range of studies investigated the SIP response associated with bacteria and biofilms. Ntarlagiannis et al. (2005) and Davis et al. (2006) cultivated bacteria and biofilms in column experiments and highlighted the possibility of applying SIP measurements to observe bacteria and biofilms. Abdel Aal et al. (2010) studied bioclogging and the associated change in hydraulic conductivity during cultivation, and suggested that the SIP response associated with biofilms is related mostly to clogging of pore throats. Zhang et al. (2014) measured the SIP response of bacterial

suspensions with and without sand and obtained quantitative relationships between bacteria cell density and SIP response. They showed that the mechanistic model for the SIP response of bacteria proposed by Revil et al. (2012) cannot accurately reproduce the SIP response of bacteria in suspension. They also showed that the SIP response of bacteria in sand has a lower peak frequency than in suspension.

In addition to the SIP response directly associated with bacteria and biofilm, it has also been shown that SIP has potential to detect mineral precipitation associated with microbial activity. Williams et al. (2005) and Ntarlagiannis et al. (2005) were the first to report that the SIP response varied over time due to mineralization associated with microbial activity and bacterial growth. Slater et al. (2007) used sulfate-reducing bacteria to generate precipitation and subsequent dissolution of iron sulfide. They found that the SIP response increased with the amount of precipitation and decreased with dissolution of iron sulfide, and concluded that iron sulfide precipitation around sand grains was responsible for the observed SIP response. Wu et al. (2011) investigated the potential of monitoring microbially-induced calcite precipitation with SIP using a sand column filled with sampled water from a field site. They found that the SIP response was weak and did not compare well with results from previous column experiments by Wu et al. (2010) that focussed on calcite precipitation associated with mixing of two solutes. Again, this suggests that further research focussed on the continuous measurement of the SIP response and the relevant environmental conditions is required because both mineral precipitation reactions and microbial activity are dynamic in time and variable in space.

Finally, laboratory experiments have been conducted to more directly replicate bioremediation processes in order to develop more direct applications of field SIP measurements. Abdel Aal et al. (2004) were the first to report that the SIP response can be affected by microbial activity during biodegradation of diesel-contaminated sediments. Abdel Aal et al. (2006) and Mewafy et al. (2013) took samples from a hydrocarbon-contaminated site and observed the SIP response of biodegradation. They showed the potential of SIP measurements to monitor biodegradation by relating the SIP response to the accumulation of microbial cells (Abdel Aal et al., 2006) and bio-metallic minerals (Mewafy et al., 2013). The SIP response of bioremediation has also been investigated in the field. The work on the Rifle Integrated Field Research Challenge (IFRC) site in the U.S. is a prime example. This site is contaminated by radioactive uranium from a former uranium processing facility. A possible remediation strategy is to immobilize the uranium by stimulating the microorganisms that reduce uranium from soluble form U^{+6} to the insoluble form U^{+4} . Flores Orozco et al. (2011) studied this site with SIP imaging, and suggested that mineral precipitation can be understood by combining SIP imaging and chemical analysis. They also suggested that the SIP response is related to the activity of the Fe^{2+} ion and speculated that calcite precipitation additionally affected the SIP response. Based on the data of Flores Orozco et al. (2011), Chen et al. (2013) used a data-driven statistical model to obtain information about the biochemical stages of subsurface remediation.

1. Introduction

As reviewed above, most research on the relationship between the SIP response and biochemical reactions is rather qualitative, and quantitative information about in-situ biochemical reactions has not yet been obtained from SIP measurements. This is related to the fact that reaction processes have rarely been directly observed in SIP experiments. Many previous studies relied on indirect information (e.g. fluid samples) and assumed that processes occur homogeneously in the measurement zone. Furthermore, the resolution in time and space are limited in many experimental setups used in SIP studies even though biochemical reactions are spatially and temporally highly variable. One of the starting points of this thesis is that such indirect information and the low spatial and temporal resolution of previous laboratory setups have been a limiting factor for exploring the potential of SIP measurements to obtain information about dynamic biochemical reactions in porous media.

1.3. Chemical reactions and mixing theory

A second starting point of this thesis is that understanding the SIP response associated with biochemical reactions requires improved understanding of the spatial distribution and temporal dynamics of the chemical reactions themselves. Chemical reactions in porous media determine the transport, transformation and degradation of chemical and biological substances in subsurface environments, such as soils and aquifers (Chapelle, 2001). The spatial and temporal dynamics of chemical reactions in such natural systems show rich phenomena such as the creation of hotspots for reaction (Bochet et al., 2020; Kolbe et al., 2019; McClain et al., 2003), intensive reactions in short time periods ('hot moments') (Briggs et al., 2014; Gu et al., 2012), and long-lasting reactions at geological time scales (Hilley & Porder, 2008). Such reaction dynamics also play an important role in a range of engineering applications, including remediation of contaminated ground water (Fu et al., 2014) and geological carbon sequestration (Zoback & Gorelick, 2012).

The interpretation of SIP measurements made in the context of reactive transport investigations have invariably assumed well-mixed reactors with a homogeneous solute concentration. In such a system, reaction kinetics determine the overall reaction behaviour. However, in many realistic cases, reactants are partly separated and thus transport of the chemical species matters for the reaction behavior (Rolle & Le Borgne, 2019; Valocchi et al., 2019). The homogenization of initially separated reactants by the interplay of diffusion and advection is referred to as mixing (Dentz et al. 2011). Mixing is enhanced by velocity field heterogeneity, which acts to elongate mixing interfaces and increase chemical gradients (Le Borgne et al., 2014). Stagnation points, which are present at all scales from flow in pore networks (Lester et al., 2016), flow in hyporheic zones (Hester et al., 2017), density driven flow (Hidalgo et al., 2015) and groundwater flow (Bresciani et al., 2019), are thought to play an important role for mixing and reaction in porous media as they induce exponential elongations. However, the dynamics of coupled

mixing and reaction at stagnation points is poorly understood and has not been documented experimentally.

The dynamics of diffusion-reaction fronts in case of the bimolecular reaction $A + B \rightarrow C$ have been extensively studied in the absence of advective transport (Gálfi & Rácz, 1988; Larralde et al., 1992). For this case, the dynamics of the reaction front were derived theoretically and numerically (Havlin et al., 1995; Larralde et al., 1992) and confirmed using laboratory experiments (Koo & Kopelman, 1991; Park et al., 2001). A few studies have investigated mixing-induced reaction dynamics in the presence of diffusive and advective transport. In particular, de Anna et al. (2014) developed a millifluidic experimental setup containing a 2D porous media that allows quantification of the reaction rate at an invading front. They showed that high reaction rates were localized in stretched parts of the invading front that formed a lamellar structure. The role of stretching in the enhancement of mixing has been quantified in the lamella theory of mixing, which provides accurate predictions of mixing rates in heterogeneous flows (Le Borgne et al. 2013, 2014). Bandopadhyay et al. (2017) coupled this theory to chemical reactions and derived analytical expressions for bimolecular reactions in shear flows based on a reactive lamella approach. In this thesis, it will be explored to what extent improved knowledge of chemical reactions at stagnation points helps to improve understanding of the SIP response of biochemical reactions in porous media.

1.4. Aims and organization of thesis

Among the possible application areas of SIP measurements, the detection of calcite precipitation is one of the least studied even though calcite precipitation is important in a range of subsurface engineering applications. Thus, the calcite precipitation process will be used in this thesis as an example of how novel experimental and modelling approaches can be used to improve mechanistic understanding of how biochemical reactions affect the SIP response. The overall aim of this thesis is to better understand how spatially variable and temporally dynamic calcite precipitation processes affect the SIP response. To achieve this, three sub-objectives are defined.

The first sub-objective is to investigate the effect of solute concentration on the SIP response of calcite precipitation. The literature review revealed that only a few studies have investigated the SIP response of calcite precipitation since the first study ten years ago by Wu et al. (2010). Follow-up studies have partly provided different results, which suggests that important factors influencing the SIP response are not yet understood. Here, it is hypothesized that the observed differences in SIP response may be related to differences in solute concentration around the calcite precipitation. In order to test this hypothesis, laboratory column experiments similar to Wu et al. (2010) will be performed to investigate the effect of varying solute concentration.

1. Introduction

The second sub-objective is to develop a novel laboratory experimental setup that enables direct visual observation of calcite precipitation processes while making SIP measurements, and to use this novel set-up to investigate how spatial variation and temporal dynamics of calcite precipitation affect the SIP response. The novel set-up will make use of a 2D porous media that allows visual observation of pore scale processes, and will be referred to as a millifluidic set-up in the thesis.

The third sub-objective is to investigate the scaling of the width, maximum reaction rate and reaction intensity at the stagnation point for different Péclet (Pe) numbers, and to explore the difference of these reaction characteristics at the stagnation point with and without the presence of a porous medium. The stagnation point is the key to understand chemical reactions in porous media because it acts to elongate mixing interfaces and increase chemical gradients in porous media. Using the millifluidic set-up, novel experiments will be performed to investigate mixing and reaction at stagnation points in a Hele-Shaw configuration as well as in a porous medium. In addition to the laboratory experiments, mixing theory and pore-scale simulations of flow velocity will be combined to investigate how flow affects the width, maximum reaction rate and overall reaction intensity. These results are expected to improve understanding of the SIP response in different environmental conditions.

The organization of this thesis is as follows. In Chapter 2, the principles of SIP will be reviewed and the SIP measurement equipment used in this thesis will be described. This will provide a fundamental understanding of SIP in geosciences including measurement technology, available theories for the mechanisms of SIP in non-conductive materials, and the relationship between local material properties and the bulk SIP response.

In Chapter 3, the effect of solute concentration on SIP response of calcite precipitation (first sub-objective) will be analyzed. This chapter will first discuss inconsistent results in previous studies about the SIP response of calcite precipitation in detail. This will be followed by a description of a sand column experiment, including the methods that will be used to vary the solute concentration without disturbing calcite precipitation induced in the sand column. The presented results will show the importance of solute concentration for the SIP response of calcite precipitation. The chapter will end with a possible interpretation of previous inconsistent results considering the effect of solute concentration.

Chapter 4 deals with the second sub-objective. In particular, the design of the novel experimental setup including visualization tools and the millifluidic set-up with a 2D porous medium will be presented first. This will be followed by the experimental procedures used to investigate calcite precipitation processes, including the effect of solute concentration already explored in Chapter 3. In addition, numerical simulation methods for electrical field simulations used for data interpretation will be introduced. Next, the spatial variation and dynamic changes in the calcite precipitation process will be analyzed using images obtained during calcite precipitation within the 2D porous media. Then, the measured SIP

response will be analyzed in the context of the insights obtained from the imaging of the calcite precipitation process. Finally, electric field simulations and a conceptual model of the polarization process relevant to calcite precipitation will be used to explain the measured SIP response in more detail.

In Chapter 5, the third sub-objective will be explored. This chapter will be dedicated to investigating scaling laws that describe the reaction front in relation to front width, maximum reaction rate, and overall reaction intensity depending on Péclet number. The chapter starts with a theory section, where it will be shown how mixing theory can be applied to an $A + B \rightarrow C$ reaction system with advective transport with a focus on the stagnation point where the mixing interface is exponentially elongated. Using these insights, scaling laws at the stagnation point will be derived. Next, the experimental and numerical procedures for the validation of the derived scaling laws will be introduced. The experimental results will be compared with the theoretical expectations and further interpreted using pore-scale numerical simulations of the flow field in the known 2D structure of the porous medium.

This thesis will conclude with Chapter 6, which will provide a synthesis of the thesis and an outlook for future studies including preliminary results about the SIP response of bacteria growth using the novel millifluidic set-up developed in this thesis.

1. Introduction

Chapter 2

Theory of spectral induced polarization

In this chapter, essential background information related to SIP will be provided. First, the principles of SIP measurements will be explained, including key features of SIP measurement setups and associated experimental design considerations. Next, previous work on the origin of the SIP response will be reviewed in detail. Finally, models to describe the SIP response of porous media will be introduced in more detail, also considering the surface chemistry of the investigated material.

2.1. SIP measurements

SIP measures the voltage within a sample while injecting a sinusoidal current with a known frequency in the mHz to kHz frequency range (Kemna et al., 2012) (Figure 2.1a). The SIP response of geological materials is considered to be due to polarization processes involving macroscopic movement of ions in addition to conductive (free) movement of ions that does not cause polarization. In a typical SIP measurement set-up (Figure 2.1a), four electrodes are used for SIP measurements. Current is injected from the top electrode and flows to the grounded bottom electrode, where the amount of current flow is determined. The top and bottom electrodes are called current electrodes, and their size and position determine the volume through which electric current flows. Two additional electrodes between the current electrodes are used to measure the voltage and they are called potential electrodes. The complex conductivity (σ^*) is obtained from the measured voltage (V^*), the injected current (I^*), the area of the measured volume (A) and the distance (d) between the potential electrodes:

$$\sigma^* = \frac{I^* d}{V^* A} \quad (2.1)$$

Complex numbers are used to take into account the time lag between the injected current and the resulting voltage, i.e. the phase shift (Figure 2.1b). The complex electrical conductivity can be expressed as:

$$\sigma^*(\omega) = \sigma'(\omega) + i\sigma''(\omega) \quad (2.2)$$

2. Theory of spectral induced polarization

where i indicates an imaginary number, σ' and σ'' are the real and imaginary part of the electrical conductivity (S m^{-1}), and f is the frequency (Hz). In the SIP frequency range, σ' of a porous medium with a non-conducting solid phase is mainly related to electrolytic conduction in the water-filled pore space of the measured sample, whereas σ'' is related to polarization of the measured sample in an alternating electric field. An alternative formulation for the complex electrical conductivity is:

$$\sigma^* = |\sigma|e^{-i\varphi} \quad (2.3)$$

where $|\sigma|$ is the magnitude of the electrical conductivity and φ is the phase shift between the applied current and the resulting measured voltage. The phase shift is related to σ' and σ'' through:

$$\varphi = \tan^{-1}\left(\frac{\sigma''}{\sigma'}\right) \approx \frac{\sigma''}{\sigma'} \quad (2.4)$$

where the approximation is valid for $\varphi < 100$ mrad, which is the case in almost all SIP applications in natural sediments. For many porous materials, the complex electrical conductivity is frequency dependent. The real part of the electrical conductivity typically increases with frequency and the imaginary part will then show a peak at the frequency where the change in the real part of the conductivity is the largest (Figure 2.1c).

In the geophysical research community, the complex electrical resistivity, which is defined as the reciprocal of the complex electrical conductivity, is also widely used. In other research communities (e.g. chemistry, biology), the complex dielectric permittivity (ϵ^*) is also often used as the measure of polarization. The complex dielectric permittivity and the complex electrical conductivity are directly related through:

$$\sigma^* = i\omega\epsilon^* \quad (2.5)$$

Thus, the information contained in the complex electrical conductivity and dielectric permittivity is equivalent. In this thesis, the complex conductivity is consistently used.

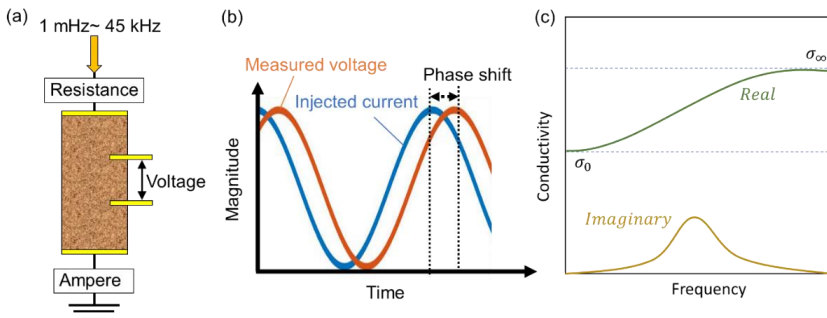


Figure 2.1. (a) Schematic overview of SIP measurement set-up with electrodes in yellow, (b) the phase shift between the injected current and measured voltage, (c) typical change in real and imaginary part of the electrical conductivity as a function of frequency.

2.2. SIP measurement system

The SIP measurement system developed by Zimmermann et al. (2008) was used for all the measurements in this thesis (Figure 2.2). This system uses four electrode channels. The injected current is generated by applying a sinusoidal voltage wave of $\pm 10\text{V}$ at maximum in the frequency range from 1 mHz to 45 kHz using a function generator (Agilent 33120A, Agilent Technologies, Santa Clara, CA). The current is injected from electrode number 1 in Figure 2.2. The amount of injected current is measured using a shunt resistor (R_s in Figure 2.2) connected to the top current electrode (electrode number 4). The electrodes number 2 and 3 are used to measure the electric potential. The measured voltages are digitized with data acquisition cards (NI4472, National Instruments, Austin, TX). The function generator and data acquisition cards are controlled by LabVIEW (National Instruments, Austin, TX).

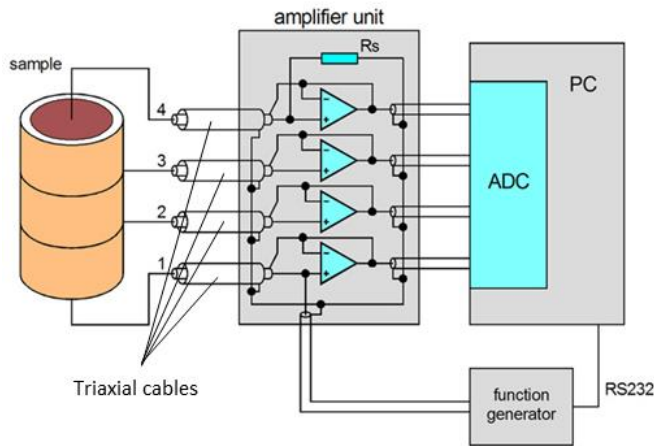


Figure 2.2. Schematic illustration of the SIP measurement system of Zimmermann et al. (2008).

For accurate SIP measurements, it is important to reduce interaction between the sample, the measuring system and the environment. One of the key features of the design is the driven guard technique with triaxial cables (Figure 2.2). The triaxial cable is composed of signal wire, conductive guard, and an outer ground shield (Figure 2.3) with insulating material between the different components. The difference between standard coaxial cables and triaxial cables is the conductive guard. During a measurement, the voltage in the signal wire and the conductive guard are adjusted to be the same in order to minimize the effective cable capacity. The ground shield works to inhibit capacitive coupling between the cable and the sample or the surrounding environment.

2. Theory of spectral induced polarization

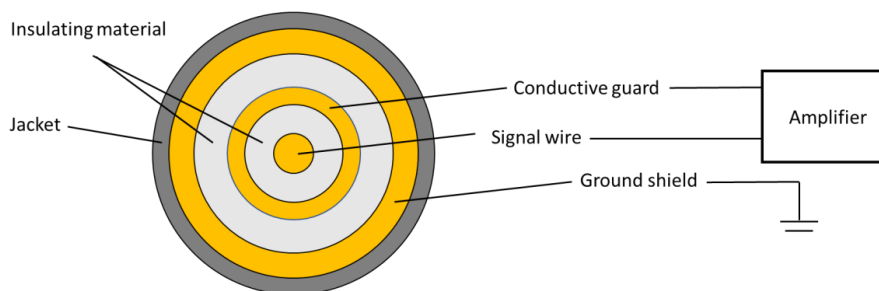


Figure 2.3. Cross-section of triaxial cable connected to an amplifier and the ground.

There are a range of additional considerations for making accurate SIP measurements as summarized in the following.

1) Appropriate distance between the potential electrodes and the current electrodes

Many SIP studies use plate electrodes at the top and bottom of the sample. In this case, the contact impedance between the current electrodes and the sample is often not homogeneous over the sample surface. This results in inhomogeneous injection of electric current with more current in areas with lower contact impedance. Because of this, the electric potential field is not homogeneous near the current electrode. This inhomogeneity in the electrical potential field decreases with distance from the current electrode. According to simulations presented in Zimmermann et al. (2008), accurate SIP measurements with a measurement accuracy below 0.1 mrad can be obtained when the ratio of the distance between the potential and current electrodes and the width of the sample is larger than 2:1, which makes sure that the electrical field is homogeneous at the position of the potential electrodes (Figure 2.4). Since the ratio of 2:1 between length and width should be maintained for the three zones between the four electrodes, it is thus recommended to keep the ratio of the sample width and length below 1/6 in order to obtain a homogeneous electric field in the vicinity of the potential electrodes.

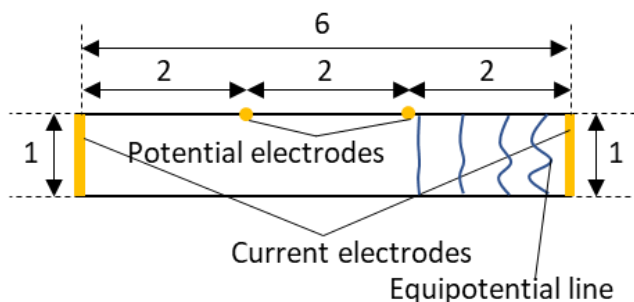


Figure 2.4. Schematic illustration showing the ratio of the distances to ensure a homogeneous potential field at the position of the potential electrodes.

2) Reduction of capacitive (current) leakage

Additional stray capacitances between the sample to the surrounding environment causes capacitive current leakage (tables etc.) (Figure 2.5) that affect the accuracy of the phase measurements. A simple measure to reduce this source of error is to increase the distance between the sample holder and the surrounding environment in order to reduce the capacitance. Therefore, it is recommended to use insulating materials with low permittivity to increase separation between the sample holder and the surroundings (e.g. working bench, clamps, etc.). An example of such a low-permittivity insulating material is polystyrene foam, which is widely available, easy to handle, and affordable.

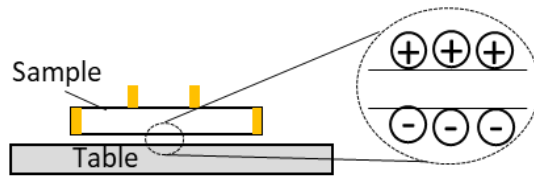


Figure 2.5. Schematic illustration of capacitances between the sample and the surrounding environment.

3) Reduction of polarization of the potential electrodes

The potential electrodes are often made of metal, and are thus easily polarized. If the potential electrodes are placed within the sample, the surface of the electrodes may polarize due to the injected current even when there is only a small electric potential difference across the electrodes (Figure 2.6a). To avoid this polarization, the potential electrodes should be retracted outside the sample whenever possible (Figure 2.6b). This is typically achieved using a small water-filled channel between the sample and the retracted potential electrodes. This channel ensures that the potential electrodes are electrically connected to the sample. According to Zimmermann et al. (2008), the ratio of the width and the length of this channel should be more than 1:2 to avoid polarization of the potential electrodes.

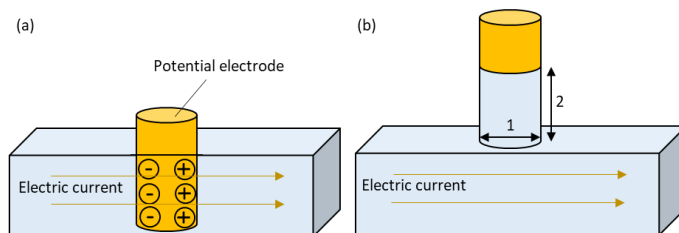


Figure 2.6. (a) Polarization at the surface of potential electrode (b) retracted potential electrode, which is not polarized.

2. Theory of spectral induced polarization

4) Contact impedance and the impedance of the sample

Due to the need to retract the potential electrodes, the contact impedance of the potential electrodes is dominated by the impedance of the channel described above. If the contact impedances and the sample impedance are large, small differences in the input capacitance of the amplifiers (Figure 2.7) result in large differences in the measured phase. This effect is associated with the fact that the measured potential at the potential electrode depends on the potential inside the sample, the impedance of the water-filled channel and the input capacitance (Figure 2.7) (Zimmermann et al., 2008). Thus, it is desirable that both the contact impedance and the sample impedance are low, which is in conflict with the need to retract the potential electrodes. Therefore, the dimensions of the sample holder and the channel used to retract the electrodes should be selected carefully.

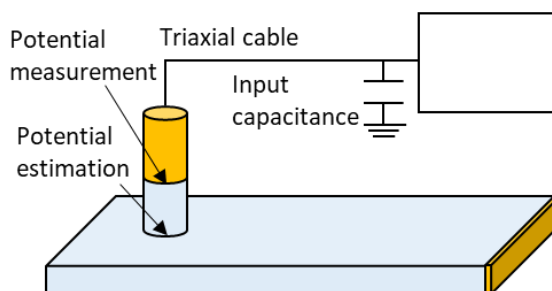


Figure 2.7. Schematic showing input capacitance of the amplifiers, position of the potential measurement and the position of the estimated potential within the sample.

2.3. Polarization mechanisms

The imaginary part of the complex electrical conductivity is related to polarization processes in the porous media. In the most general sense, polarization is associated with a separation of positive and negative charges by some distance. Depending on the mechanism that separates these charges, the polarization can be categorized (Figure 2.8) (Kemna et al., 2012). A first category is permanent polarization at the molecular scale with the water molecule as a prime example. The permanent polarization of the water molecule is caused by the higher electronegativity of oxygen compared to hydrogen. This permanent polarization thus exists without an external electric field. The rotational relaxation of the water molecule occurs at frequency of around 19.2 GHz at 25 °C (Tanaka & Sato, 2007). Since SIP measurements make use of much lower frequency range (<100 kHz), the contribution of permanent polarization can be represented by a frequency-independent permittivity of the investigated medium.

Other sources of polarization are referred to as induced polarization because polarization only occurs when an external electric field is applied. Induced polarization involving dielectric materials with

different permittivity is caused by the displacement of bound charge, which is often referred to as Maxwell-Wagner polarization. This polarization dominates in the kHz to MHz frequency range.

Induced polarization can also be due to the macroscopic movement of ions, which typically occurs at much lower frequencies (< 100 kHz) because ions require a few microseconds to reach equilibrium. At higher frequencies, ions are not able to follow the change in electric field anymore and thus do not contribute to polarization (Gagnon, 2011). Different sources of ionic polarization have been proposed to explain the SIP response of porous media, which are often referred to as grain polarization and membrane polarization. Grain polarization is associated with ions that preferentially move tangentially to the grain surface when an electric field is applied. This results in an accumulation of positive charges (cations) on one side of the grain, and the accumulation of negative charges (anions) on the other side of the grain (Revil et al., 2012). In the case of membrane polarization, polarization is attributed to the different mobility of ions in the narrow part of the pore space (i.e. pore throats) that leads to a separation of charges (Kemna et al., 2012). For example, negative charges on the surface of the pore throat might reduce the mobility of negative charges in the bulk solution, leading to an accumulation of positive charges in the pore throat (Marshall & Madden, 1959). In all cases, polarization is established by competing against diffusion of molecules, which acts to equilibrate the distribution of charges.

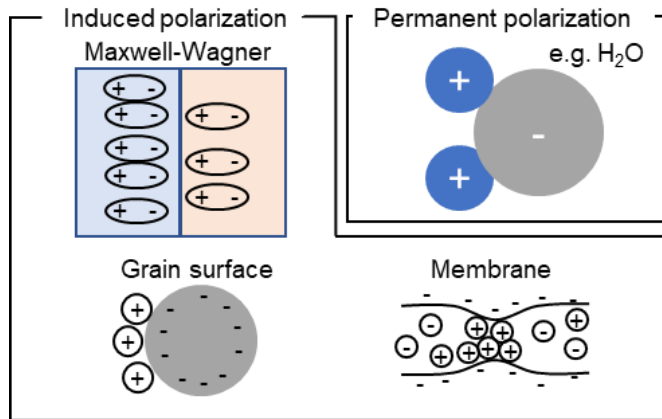


Figure 2.8. Summary of possible polarization mechanisms.

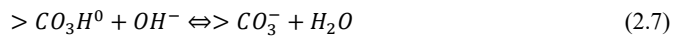
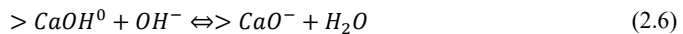
2.4. Grain polarization model

The grain polarization model has been used to explain the source of polarization of calcite precipitation in previous studies (Leroy et al., 2017; Wu et al., 2010). The grain polarization model explains electrical polarization using the movement of charges accumulating at the mineral-solution interface. This accumulation is caused by local excess of charge at the mineral surface, which attracts counter-ions (ions with the opposite charge as the interface) in the electrolyte. The attraction force is thus due to the

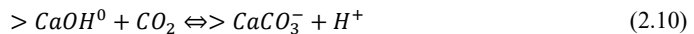
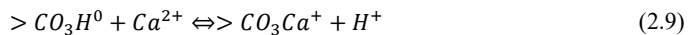
2. Theory of spectral induced polarization

electrostatic force arising between the mineral surface and bulk ions. This arrangement of ions at the interface is often described using two layers and is thus widely called the electric double layer (EDL) (Figure 2.9a). The first layer is composed of ions closely associated with the surface (typically without hydration shell) and is referred to as the Stern layer. The Stern layer usually does not fully balance the surface charge. This leads to the presence of a second so-called diffuse layer outside of the Stern layer, which contains the excess charges to make the EDL electrically neutral. Ions in the diffuse layer are typically hydrated and cannot enter the Stern layer.

The EDL properties can be inferred from electrokinetic experiments using streaming potential measurements (Figure 2.9b). In such experiments, charged particles (e.g. calcite powder) are packed into a sample holder, and a solution with known water chemistry is forced to flow through the packed particles. This results in a potential difference between the two ends of the packed calcite sample because excess charge near the mineral surface is moved due to the flow of the solution. From this type of experiment, a key physicochemical parameter called the zeta potential, which is the potential at the shear plane in the diffuse layer, can be obtained. Although the surface charge properties of calcite have been studied extensively (Al Mahrouqi et al., 2017), the properties of the EDL of calcite are still not fully understood. It is expected that that pH strongly affects the surface charge of calcite because the pH defines the concentration of H^+ and OH^- in the solution, which can adsorb on negatively or positively charged surface site, and thus should control protonation and deprotonation on the surface according to the following reactions:



where > denotes crystal lattice. However, a recent review on previous studies of the zeta potential of calcite summarized that the calcite surface charge is only weakly dependent on pH (Al Mahrouqi et al., 2017). Instead, it was argued that Ca^{2+} , Mg^{2+} and CO_3^{2-} are the important ions that control the zeta potential of the calcite surface with surface complexation reactions such as:



Heberling et al. (2014) presented a surface complexation model to calculate surface charge and EDL properties of calcite immersed in solution using the relevant chemical reactions with given equilibrium constants. In this model, the reactions given by Equations (2.9), (2.10) and (2.11) were not yet considered.

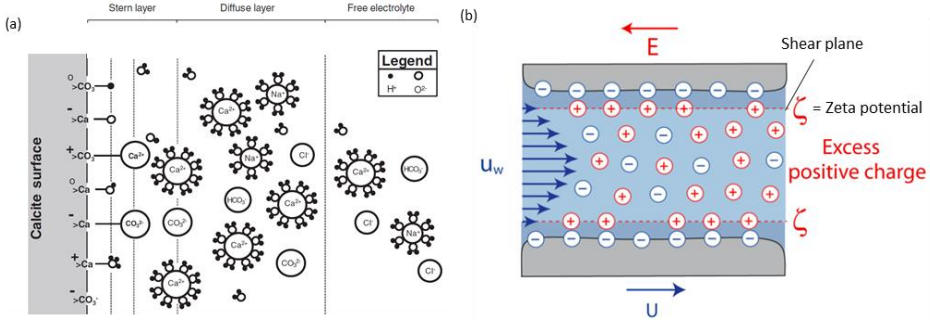


Figure 2.9. (a) Electric double layer (EDL) of calcite (Al Mahrouqi et al., 2017) (b) Illustration of streaming potential measurement (Li et al., 2016).

Leroy et al. (2017) used the surface complexation model of Heberling et al. (2014) to predict the SIP response of porous media with calcite using the grain polarization model (Figure 2.10). At the core of this model, there is a mathematical expression derived by Schwarz (1962) that describes the complex conductivity of a charged colloidal particle assuming that the counter-ions can only move tangentially along the surface of the colloid move when an electric potential is applied. No distinction was made between the role of the Stern layer and the diffuse layer. Lyklema et al. (1983) argued that ions in the diffuse layer move in the direction opposite to the ions in the Stern layer in order to maintain electroneutrality in total, and that this movement results in an electric field that counteracts ion movement in the Stern layer. Leroy et al. (2017) assumed that polarization of the Stern layer controls the imaginary part of the conductivity, and that the diffuse layer only affects the relaxation time and real part of the conductivity as follows:

$$\sigma_s^* = \frac{4}{d} \left[\pm \beta_b Q_b \left(\frac{i\omega\tau_b}{1 + i\omega\tau_b} \right) + \sum_{i=1}^N e z_i B_i^d \Gamma_i^d \right] + i\omega\alpha\rho_s\varepsilon_0 \quad (2.12)$$

Here, the term $\pm\beta_b Q_b \left(\frac{i\omega\tau_b}{1 + i\omega\tau_b} \right)$ represents the contribution of the Stern layer, $\sum_{i=1}^N e z_i B_i^d \Gamma_i^d$ represents the DC conductivity of the diffuse layer, and $i\omega\alpha\rho_s\varepsilon_0$ is an empirical term linking the complex conductivity of the mineral and its volumetric density. In this equation, d is the diameter of the calcite particle, β_b is the averaged ion mobility in the Stern layer, Q_b is the surface charge density of the adsorbed ions in the Stern layer ($\pm\beta_b Q_b$ is always positive), $i^2 = -1$, ω is the angular frequency ($2\pi f$), N is the number of different ions in the diffuse layer, e is the elementary charge of the electron, z_i is the ion valence, B_i^d is the effective ion mobility in the diffuse layer, Γ_i^d is the surface site density of the adsorbed ions in the diffuse layer, α is an empirical coefficient, ρ_s is the volumetric density of calcite, and ε_0 is the dielectric permittivity of vacuum. The relaxation time of the polarization of the Stern layer τ_b is associated with the time for the ions to diffuse back to the original position when the electric field

2. Theory of spectral induced polarization

is switched off, and thus is a function of the shape and size of the particle. The averaged diffusion coefficient in the Stern layer is D_b is given by:

$$\tau_b = \frac{d^2}{8D_b M} \quad (2.13)$$

$$M = 1 + \frac{qQ_b}{k_b T C_d} \quad (2.14)$$

where M is a factor accounting for the effect of the polarization of the diffuse double layer on the relaxation time of the Stern layer, q is the averaged electrical charge of the counter-ions in the Stern layer, k_b is the Boltzmann constant, T is temperature and C_d is the differential capacitance of the diffuse layer, which is the derivative of the charge density with respect to the electrical potential over the diffuse layer. The link between the surface complexation model of Heberling et al. (2014) and the above expressions is through Γ_i^d and Q_b , which are related to charge density of diffuse layer and Stern layer.

In order to interpret experimental results with a mixture of substances, for example water and calcite, Equation 2.12 needs to be upscaled to obtain the complex electrical conductivity of the bulk porous medium σ^* . This can be achieved using the Hanai-Bruggeman equation obtained from effective medium theory (Hanai, 1960):

$$\sigma^* = \frac{\sigma_w^*}{\phi^{-m}} \left(\frac{1 - \sigma_s^*/\sigma_w^*}{1 - \sigma_s^*/\sigma^*} \right) \quad (2.15)$$

where σ_w^* is the complex conductivity of the bulk water, σ_s^* is the complex surface conductivity, ϕ is the porosity and m is the cementation exponent of the particles, which is 1.5 for spheres. The model of Leroy et al. (2017) is difficult to apply to actual measured SIP data because there are a lot of parameters (e.g. $\sum_{i=1}^N e z_i B_i^d \Gamma_i^d$ for N chemical species, at least ones in equilibrium with calcite, Ca^{2+} , CO_3^{2-} , HCO_3^- , H^+ and OH^-) including empirical coefficients (α) that need to be specified.

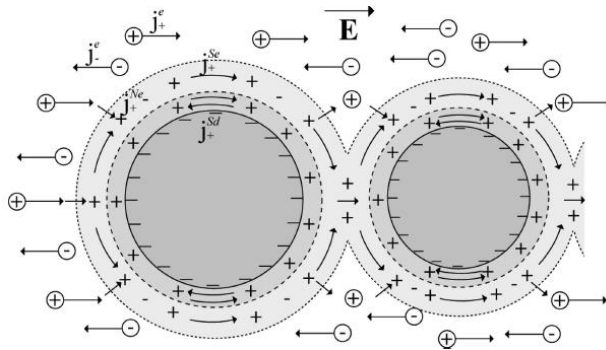


Figure 2.10. Grain polarization associated with Stern layer and diffuse layer (Leroy et al., 2008).

2.5. Empirical models to describe complex electrical conductivity

Many studies have used much simpler empirical models to interpret experimental results. The widely used Cole-Cole model (e.g. Tarasov & Titov, 2013) is given by:

$$\sigma^* = \sigma_\infty + \frac{\sigma_0 - \sigma_\infty}{1 + (i\omega\tau)^c} \quad (2.16)$$

where σ_0 and σ_∞ are the low-frequency and high-frequency conductivity, respectively, and τ is the relaxation time. This model can fit both the real and imaginary part of the complex electrical conductivity of many SIP measurements. The parameters of the Cole-Cole model have been widely used to characterize the SIP response (e.g. Slater et al., 2007). In previous studies, the fitted relaxation time has been interpreted using:

$$\tau = \frac{r^2}{2D} \quad (2.17)$$

where r is the radius of the polarizing particle and D is the diffusion coefficient of the ions (Schwarz, 1962). Here, smaller polarization length scales and larger diffusion coefficients result in smaller relaxation times. This makes sense because it takes less time to establish the equilibrium condition after the polarization if the length scale is smaller or when the ions move faster. The Cole-Cole model is of interest here because it can be used irrespective of polarization mechanism and there are no upscaling issues. However, the model does not have predictive capability due to its empirical nature.

2. *Theory of spectral induced polarization*

Chapter 3

Effect of solute concentration on the SIP response of calcite precipitation

In this chapter*, the SIP response of calcite precipitation will be investigated using column-scale experiments. This was motivated by the limited amount of studies focussed on the SIP response of calcite, and the inconsistency in the presented results (Table 3.1). Wu et al. (2010) mixed two solutions in a column filled with glass beads to induce calcite precipitation and observed a strong increase in σ'' with an increasing amount of calcite precipitation. The maximum σ'' and φ were about 4 mS m^{-1} and 50 mrad , respectively. However, other studies observed considerably weaker SIP responses due to calcite precipitation. For example, Saneiyani et al. (2018) induced calcite precipitation by mixing of two saline solutions in a sand column and observed a maximum σ'' of 0.45 mS m^{-1} . Wu et al. (2011) used natural groundwater amended with urea to induce calcite precipitation in a column filled with natural sediment. The induced calcite precipitation resulted in an increase in σ'' of about 0.02 mS m^{-1} and a 1 mrad increase in φ . Zhang et al. (2012) investigated a column filled with silica gel amended with the urease enzyme, and induced calcite precipitation by injecting urea. In this experiment, σ'' and φ decreased when calcite precipitation was induced. Although the SIP response of calcite precipitation is expected to depend on the amount of calcite precipitation (Wu et al., 2010), additional factors controlling the SIP response have not yet been systematically investigated.

It is well known that SIP is determined by the surface chemistry of the investigated sample (Lesmes & Frye, 2001; Merriam, 2007). Therefore, the relatively large differences in SIP response obtained in previous studies may have been related to different chemical conditions near the precipitated calcite surfaces. Recently, Leroy et al. (2017) proposed a mechanistic grain polarization model considering the polarization of the electrical double layer of calcite, which was introduced in Chapter 2. This model

* This chapter is adapted from a journal article published as:
Izumoto, S., Huisman, J. A., Wu, Y., & Vereecken, H. (2019). Effect of solute concentration on the spectral induced polarization response of calcite precipitation. *Geophysical Journal International*, 220, 1187–1196.
<https://doi.org/10.1093/gji/ggz515>

3. Effect of solute concentration

predicts that σ'' increases as the surface charge density of the calcite increases, which in turn is controlled by the solute concentration and the equilibrium constants of the complexation reactions at the calcite/water interface as defined in the model of Heberling et al. (2014). Leroy et al. (2017) parameterized their model using measured outflow data by Wu et al. (2010) after the chemical composition of the outflow became roughly constant, and solute concentration was assumed to be homogeneous throughout the column. However, this assumption may not be fully appropriate since calcite precipitation was induced under highly oversaturated conditions in the absence of chemical equilibrium between the solution and the calcite phase. In such a situation, it is likely that the concentration of the outlet solution only partly represents the solute concentration in contact with the calcite. Within this context, the aim of this study is to investigate the sensitivity of the SIP response of calcite to changes in solute concentration using laboratory column experiments.

Table 3.1. Summary of previous researches about SIP response of calcite precipitation in laboratory experiments. Increase in imaginary part of the conductivity and solute concentrations used in the experiments are shown.

Reference	Observed increase in imaginary part of conductivity (mS m ⁻¹)	Solute concentration
Wu et al. (2010)	4	CaCl ₂ : 26.2 mM Na ₂ CO ₃ : 29.0 mM
Wu et al. (2011)	0.02	Ca ²⁺ : 1 mM Total dissolved carbonate: 4 mM
Zhang et al. (2012)	Decreased	Ca ²⁺ : 10 mM Urea: 10 mM
Saneiyan et al. (2018)	0.45	CaCl ₂ : 20 mM Na ₂ CO ₃ : 20 mM

3.1. Methods

Laboratory experiments were conducted using an acrylic column with an inner diameter of 3.0 cm and a height of 18 cm (Figure 3.1), and the SIP measurement system developed by Zimmermann et al. (2008), which is shown in Chapter 2. This SIP system uses four electrode channels. Two channels were connected to porous brass plates at the top and bottom of the column that were used to inject current into the sample. The other two channels of the SIP system were connected to two potential electrodes placed at 6.0 cm and 12.0 cm height between the current electrodes to measure voltages. These electrodes had a diameter of 0.8 cm and were made of brass. Cable glands with an inner diameter of 0.8 cm were used to connect the column and potential electrodes without water leakage. To avoid electrode

polarization during the SIP measurements, the potential electrodes were retracted by 1.6 cm (twice the inner diameter of the cable gland) following recommendations of Zimmermann et al. (2008) and Huisman et al. (Huisman et al., 2016), as in Chapter 2.

The column was equipped with two solute injection ports at the bottom and side, and one solute outlet port at the top (see Figure 3.1). For the injection port at the side of the column, an additional injection tube was inserted into the sample such that the injection point was in the middle between the potential electrodes. The column was filled with F36 sand (0.09-0.25 mm, Quarzwerke Frechen, Germany) up to 1.4 cm below the top current electrode using a wet-packing procedure. The water-filled space between the sand surface and the top current electrode was used to prevent clogging of the current electrode by calcite precipitation in the flow experiments. Initially, the sample was saturated with 26.2 mM CaCl₂ solution (Solution pair 1 in Table 3.2).

The flow experiments with the sand column were separated in four phases. In phase I, 29.0 mM Na₂CO₃ and 26.2 mM CaCl₂ solutions (Solution pair 1 in Table 3.2) were injected with a flow rate of 2.93 ml h⁻¹. The CaCl₂ solution was injected from the bottom and the Na₂CO₃ solution was injected from the side, which resulted in a clear precipitation front within the sample (see Figure 3.1). The solute concentrations and flow rates were selected to be close to the values used in Wu et al. (2010). In that study, it was confirmed that the observed precipitation was calcite by direct observation with a scanning electron microscopy. Given the similar experimental conditions, we assumed that the precipitation observed in the experiment also was calcite. The precipitation of calcite is described by



The degree of oversaturation can be described by the saturation index SI (Appelo & Postma, 2007):

$$SI = \log(IAP/K) \quad (3.2)$$

where IAP is the ion activity product and K is the solubility product (10^{-8.48} for calcite). For calcite, the IAP is defined as:

$$IAP_{Calcite} = a_{Ca^{2+}} a_{CO_3^{2-}} \quad (3.3)$$

where $a_{Ca^{2+}}$ is the activity of the calcium ion and $a_{CO_3^{2-}}$ is the activity of the carbonate ion. The saturation indices of the injected solutions (Table 3.2) were calculated based on chemical speciation by PhreeqC (Parkhurst & Appelo, 2013). Throughout all experimental phases, the observed pH of the CaCl₂ solution (Table 3.2) was slightly below the expected pH calculated using PhreeqC (7.0), which indicated that CO₂ from the atmosphere dissolved into the solution. However, PhreeqC calculations showed that the total amount of dissolved CO₂ was less than 0.01% of the carbonate added as Na₂CO₃ in all the solution pairs. In addition, the maximum difference between the measured and calculated pH of the Na₂CO₃ solution was only 0.1. For these reasons, dissolution of the CO₂ into the solutions was ignored in the calculation of the saturation indices. It is important to note that calcite precipitation was expected to be mainly induced in the zone where the two injected solutions mixed. Therefore, the

3. *Effect of solute concentration*

calculated saturation index based on the assumption of two fully mixed solutions may not be fully representative for the conditions near the precipitates since the ongoing calcite precipitation in the reaction front will locally reduce ion activity and the saturation index. In this first experimental phase, SIP measurements were made every 2 days for 12 days in order to investigate the SIP response associated with the development of calcite precipitates in the column. Additionally, the electrical conductivity of the outlet solution was measured every day.

After phase I, three additional experimental phases (phase II to phase IV) were implemented to investigate the effect of solute concentration on the SIP response. Na_2CO_3 and CaCl_2 solutions with the same salt concentrations as used in phase I (Solution pair 2 in Table 3.2) were injected between each of these experimental phases in order to approximately come to the same SIP response as at the end of phase I at the start of phase II - IV. This was only partly successful since the σ'' increased substantially between the start of phase II and III. This likely indicates additional calcite precipitation between phase II and phase III, which is difficult to avoid when working with oversaturated solutions. For this reason, care should be taken when comparing SIP measurements between phases.

In phase II, the injected solutions were increasingly diluted in steps. First, the solution pair with a saturation index of 3.18 (more than 1500 times higher concentration than the equilibrium condition) was injected for 3 hours (solution pair 2 in Table 3.2), followed by the injection of solution pairs diluted by a factor of 1.9 for the first 2 steps and 2.5 for the last step (solution pair 3-5 in Table 3.2). The duration of the injection of each solution pair was 3 or 4 hours (Table 3.2). SIP measurements were made after each dilution step. To limit the amount of additional calcite precipitation in this experimental phase, the entire phase lasted only 13 hours. In order to sufficiently flush the column within the limited available experimental time, the injection rate was increased to 28.2 ml h^{-1} for both ports. With this higher flow rate, the total volume of the injected solution was at least 3.5 times larger than the pore volume of the sand (48.6 ml). In phase III, the injection of the two solutions was stopped for 50 hours and SIP measurements were made at regular time intervals. In phase IV, the injection rate of the Na_2CO_3 solution was reduced to 45% of the original injection rate (1.31 ml h^{-1}) for 7 hours. This change in flow rate was expected to shift the position of solute mixing zone away from the original calcite precipitation front and thus change the solute concentration of the water in contact with the precipitated calcite.

Because of the assumed importance of the position of the mixing zone of the two injected solutions, the streamlines and velocity fields within the column in phase I, II and IV were simulated using the open-source simulation platform OpenFOAM® (<http://www.openfoam.org>). In these simulations, the hydraulic conductivity of the F36 sand was assumed to be $2.0 \times 10^{-2} \text{ cm s}^{-1}$ as determined by Koch et al. (2011). Porosity was $0.41 \text{ (cm}^3 \text{ cm}^{-3}\text{)}$ based on the measured weight of the packed sand.

Table 3.2. Electrical conductivity, pH and concentration of injected solution pairs. Solution pair 1 with a saturation index of 3.18 was used to generate calcite precipitation until day 12, and solution pair 2 with a saturation index of 3.18 was used for rest of the experiments.

Solution pair No.	1	2	3	4	5
Saturation index	3.18	3.18	2.85	2.50	2.00
Electrical conductivity (mS cm^{-1})	4.95	4.95	2.69	1.46	0.62
CaCl ₂ pH	6.07	6.64	6.76	6.38	6.98
Concentration (mmol L^{-1})	26.2	26.2	13.6	7.1	2.9
Electrical conductivity (mS cm^{-1})	4.43	4.44	2.51	1.44	0.62
Na ₂ CO ₃ pH	11.2	11.2	11.2	11.1	11.0
Concentration (mmol L^{-1})	29.0	29.0	15.1	7.8	3.2
Injection time in phase II (h)		3.0	4.0	3.0	3.0

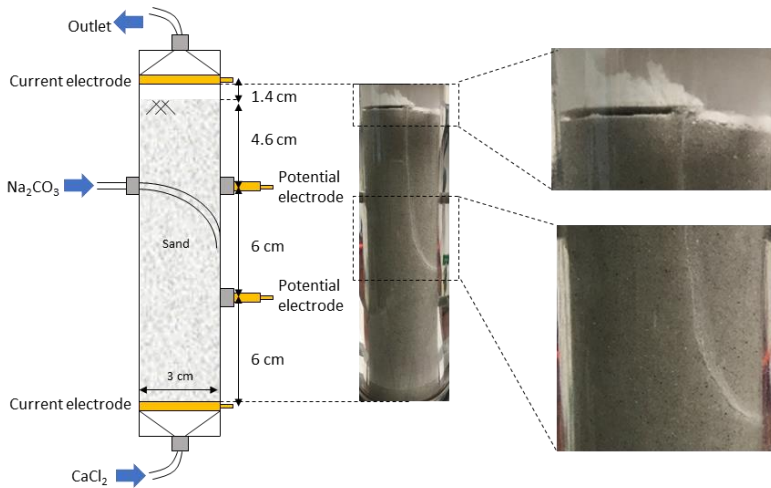


Figure 3.1. Schematic drawing of the column with electrode positions and a photo of the column at day 12. The injection tube for Na₂CO₃ was bent to inject solution in the middle between the potential electrodes.

3.2. Results and discussion

Figure 2a shows the simulated streamlines for the injected Na_2CO_3 and CaCl_2 solution in phase I indicating that the two solutions were not fully in contact with each other and thus incompletely mixed, which implies that only a part of the injected solutions reacted within the sand column. It is important to note that this simulation result should only be interpreted in a qualitative manner since the feedback of the calcite precipitation on the flow and the associated reaction kinetics in such a highly oversaturated solution have not been considered here. Figure 1 shows a photo of the column at the end of phase I (day 12). The white area in the column indicates the calcite precipitation front at the position where the two solutions were expected to mix. The observed shape of the precipitation front was similar to the shape of the boundary between the streamlines of the two injected solutions. Also, it was visually observed that precipitation was strongest just below the injection point (Figure 3.1). This is consistent with the low simulated pore water velocity in this area (Figure 3.2a), which resulted in the largest residence time of the injected Na_2CO_3 solution. Additional calcite precipitation was observed on the surface of the sample, which also emphasizes the incomplete mixing in the sand column (Figure 3.1).

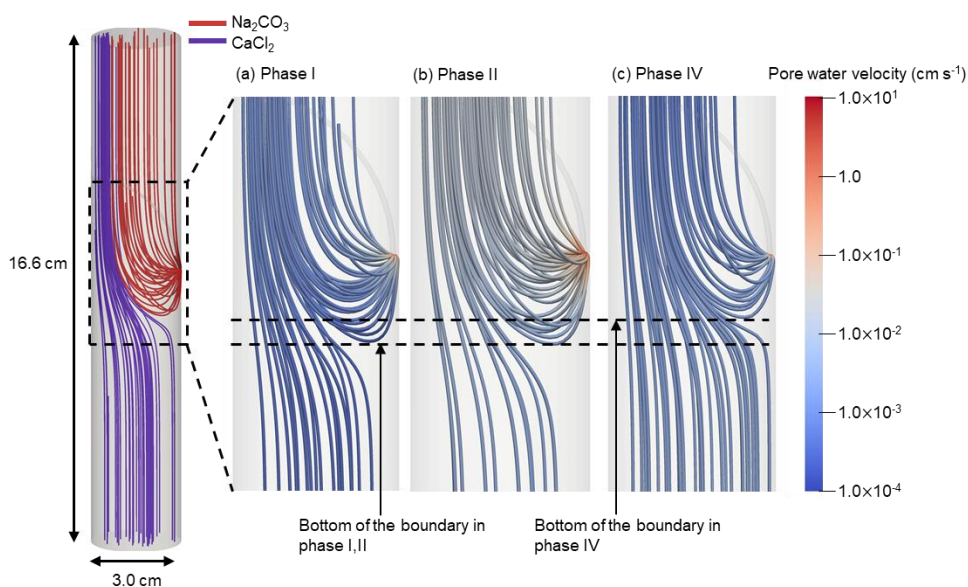


Figure 3.2. Simulated streamlines of Na_2CO_3 and CaCl_2 solution in the entire column and a close-up of the area near the injection tube for (a) phase I, (b) phase II, and (c) phase IV.

The conductivity of the outlet solution varied between 2.83 and 2.92 mS cm^{-1} except for the first day where it was 3.73 mS cm^{-1} . A solution in equilibrium with calcite was calculated to have an electrical conductivity of 2.95 mS cm^{-1} using PhreeqC, which is near the observed conductivity values. However,

it should be noted that the outlet solution likely did not represent the solute concentration within the SIP measurement zone between the potential electrodes, because the injected solutions were only fully mixed in the water layer above the sample material as indicated by the calcite precipitation on the surface of the sample (Figure 3.1) and by the simulated streamlines (Figure 3.2).

Figure 3.3 shows the development of σ' and σ'' during phase I. For the initial conditions at day 0, the cementation factor m in Archie's law (Archie, 1942) was calculated to be 1.5 using:

$$\lim_{\sigma_s \rightarrow 0} \left(\frac{\sigma_w}{\sigma} \right) = \phi^{-m} \quad (3.4)$$

where σ_s is the surface conductivity, σ_w is the solution conductivity of the CaCl_2 solution in the column (4.95 mS cm^{-1}), σ is the real part of the conductivity at 1 kHz (1.33 mS cm^{-1}), and ϕ is the porosity ($0.41 \text{ cm}^3 \text{ cm}^{-3}$). σ' decreased between day 0 and day 2 after the injection of the Na_2CO_3 solution was initiated. This was expected because the conductivity of the Na_2CO_3 solution was smaller than the conductivity of the CaCl_2 solution that was initially present (Table 3.2). Between day 2 and day 4, σ' did not change significantly. The porosity ϕ at day 2 and day 4 can be estimated by assuming that σ_w can be approximated by the average conductivity of the injected solutions and assuming that m is constant, which is reasonable given that m is only related to the shape of the grains (Bussian, 1983; Sen et al., 1981). No significant changes in porosity were obtained using this approach.

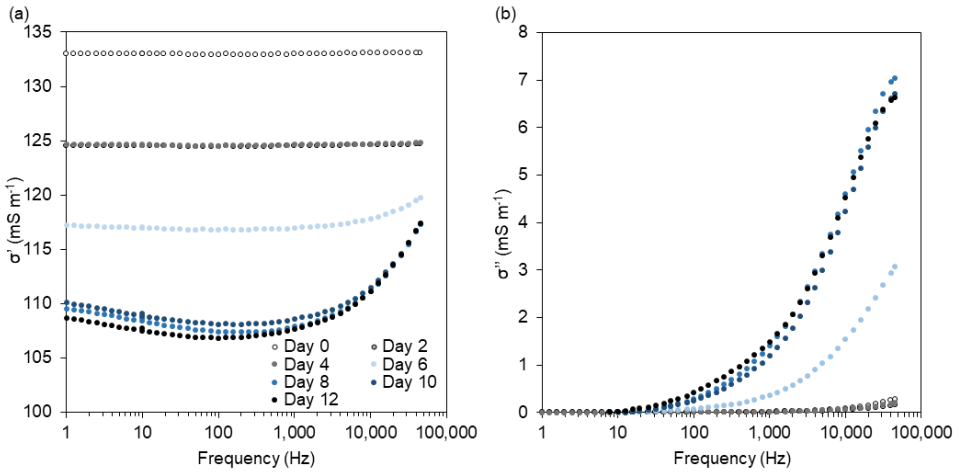


Figure 3.3. Change in (a) σ' and (b) σ'' caused by calcite precipitation during the first 12 days of phase I. Open symbols represent the measured values in the initial condition before starting the injection.

For the first four days, σ'' was almost constant although calcite precipitation was observed visually. The lack of change in σ'' and estimated porosity perhaps suggests that the amount of calcite precipitation may not have been sufficient to generate a SIP response in the early stages of the

3. *Effect of solute concentration*

experiment as will be discussed below. The lack of response may also have been affected by the initial formation of meta-stable amorphous calcium carbonate, which is reportedly first formed when CaCl_2 and Na_2CO_3 solutions with a saturation index larger than 2.1 are mixed (Rodriguez-Navarro et al., 2016). This was confirmed for the two solutions used in phase I by mixing them in a beaker. This resulted in a white opaque solution that was created within some minutes after mixing. This metastable amorphous phase disappeared again after some hours, after which the solution became transparent again. Kinetic effects directly associated with calcite precipitation may also have played a role in the weak SIP response in the first days. It has been shown that the growth of calcite crystals highly depends on the availability of nucleation sites on calcite surfaces, because calcite crystals mainly grow through the attachment of ions or amorphous calcium carbonate to the surface of calcite (Morse et al., 2007; Rodriguez-Navarro et al., 2016). For all these reasons, the growth rate of calcite may have been small in the first days of the experiment.

σ' slightly decreased between day 4 to day 8, and σ'' markedly increased in this period. The observed strong increase in σ'' is consistent with the results presented in Wu et al. (2010), who mixed CaCl_2 and Na_2CO_3 solutions with the same concentrations as used here in a column filled with glass beads. After day 8, σ' and σ'' remained almost constant despite continuous input of solutes, indicating that the amount of calcite was almost constant within the measurement zone. This may be due to the limited further mixing and reaction between the injected solutions in the measurement zone because of the growth of the calcite precipitation within the pore space. This feedback between precipitation and reaction rate was already observed in a previous microfluidic experiment (Zhang et al., 2010).

In phase II, the column was flushed with solutions with a different saturation index (Solution pair 2-5 in Table 3.2) and a higher injection rate. Figure 2b shows the simulated streamlines and pore water velocity in phase II (again neglecting effects of calcite precipitation on the flow field). A comparison with the simulated streamlines of phase I (Figure 3.2a) shows that the boundary between the injected Na_2CO_3 and CaCl_2 solutions did not change between these two experimental phases. Obviously, the pore water velocity was higher in phase II due to the higher injection rate. These simulation results suggest that the calcite precipitation generated in phase I was expected to be in contact with the injected Na_2CO_3 and CaCl_2 solutions in phase II. This was further confirmed by the SIP measurements for solution pair 2, where it was found that the increase in injection rate only resulted in a maximum decrease of 1.2 mS m^{-1} at 40 kHz for σ'' within the first hour. This initial small decrease may be because some calcite precipitation was dislodged and flushed out of the sample due to the increased shear stress associated with higher flow velocities.

When the column was flushed with solution pairs with decreasing saturation index, σ' and σ'' both decreased (Figure 3.4). The decrease in σ' is directly related to the decrease in the electrical conductivity of the two solutions (Table 3.2). In addition, it is well known that σ'' depends strongly on solution conductivity for several geological media (Revil & Skold, 2011; Weller & Slater, 2012). The

relationship between σ'' and the electrical conductivity of the solution (σ_w) is shown in Figure 5 for three different frequencies. As the reaction kinetics of the calcite precipitation were not clear in the experiment, σ_w was calculated by assuming that the reaction rate is either very slow (Figure 3.5a) or very fast (Figure 3.5b). In the first case, σ_w equals the average electrical conductivity of the injected solution. In the second case, the σ_w was calculated using PhreeqC assuming that the solution is in equilibrium with calcite. In both cases, a simple power law function was fitted to the observed σ'' (1 kHz, 10 kHz and 45 kHz) and σ_w :

$$\sigma''(f) = a(\sigma_w)^b \quad (3.5)$$

where a and b are fitting parameters (Weller & Slater, 2012). The b value in the fitted power law varied from 0.83 to 1.05 with increasing frequency. Weller and Slater (2012) reported b values for sand and sandstone that ranged from 0.10 to 0.64, with a mean value of 0.34 for solute conductivities less than 1000 mS m^{-1} . Although the values of Weller and Slater (2012) were obtained for a lower frequency (less than 30 Hz), the larger b values in the experiment suggest that the SIP response of calcite has a stronger dependence on the solute conductivity than sand and sandstone. It is important to note that the petrophysical model from Weller and Slater (2012) is for equilibrium conditions, while the system in this chapter is not in equilibrium and precipitation of calcite is occurring continuously during the experiment.

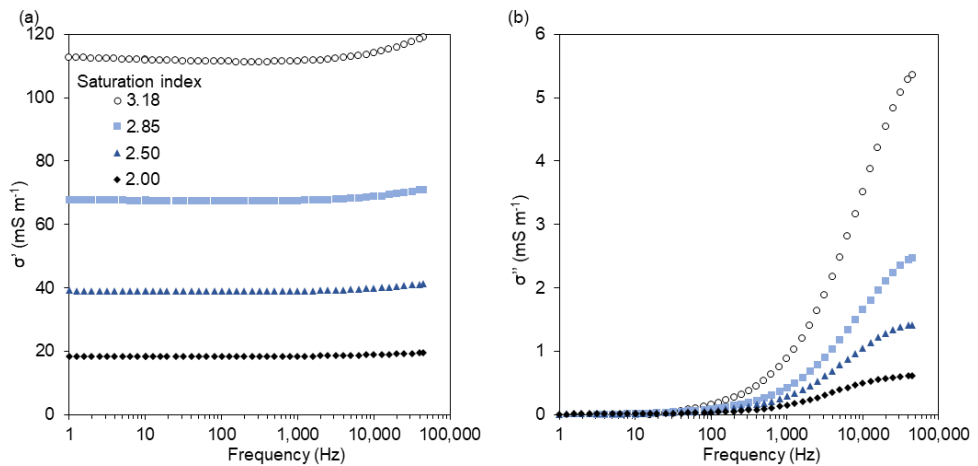


Figure 3.4. Change in (a) σ' and (b) σ'' when the column was flushed with solution pairs with different saturation index (solution pair 2-5 in Table 3.2) in phase II.

3. Effect of solute concentration

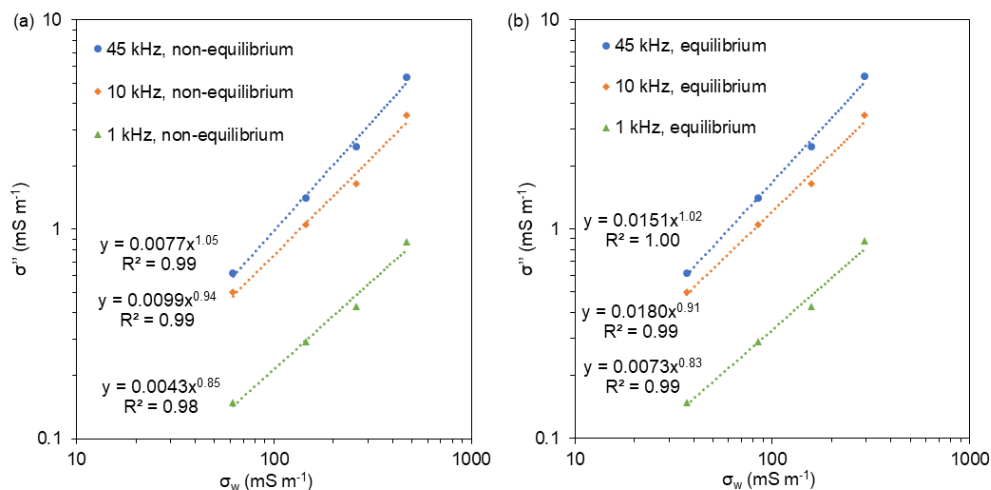


Figure 3.5. Relationship between σ_w and σ'' in phase II for different frequencies by assuming that the injected solutions were (a) reacting slowly and thus not in equilibrium with calcite and (b) reacting quickly and thus in equilibrium with calcite. The associated fits of Eq. (7) to the measured values are also presented.

When the injection of both solutions was stopped in phase III, the σ' varied only $\pm 5\%$ and showed an initial increase and a subsequent small decrease (Figure 3.6a). This change was much smaller than the difference between σ' at the start and at the end of phase III. Thus, this change in σ' was not attributed to the formation of calcite precipitation, but to a moderate change in solute concentration. Considering that σ' varied only $\pm 5\%$, only a small part of the ions in the column could have been consumed due to calcite precipitation after flow was stopped. Nevertheless, σ'' significantly decreased over time (Figure 3.6b) albeit with a decreasing rate as shown exemplary in Figure 3.7 for a frequency of 1 kHz. We hypothesize that this strong decrease in σ'' is related to a decrease of the solute concentration in contact with the calcite in the precipitation front. When injection and flow was stopped, calcite precipitation continued and the concentration of Ca^{2+} and carbonate species (HCO_3^- and CO_3^{2-}) in the mixing zone decreased, whereas Na^+ and Cl^- did not react. Such a decrease in the concentration of Ca^{2+} and carbonate species will lead to a decrease in σ'' as already shown in phase II of the experiment. Interestingly, this decrease in σ'' is fully reversible since the σ'' returned to very similar values 21 hours after injection was started again (Figure 3.6). It should be noted that σ'' continued decreasing even 50 hours after stopping the injection. This long duration probably reflects the slow change in solute concentration near the calcite precipitation as a result of a balance between the kinetics of the precipitation reaction and the continuous supply of solutes from outside the mixing zone through diffusion. This interpretation of the experimental data suggests that it is important to consider the solute concentration in contact with

calcite, and not the solute concentration in the bulk water or the outflow. While direct evidence is absent to support this interpretation, it is speculated that the concentration of calcium and carbonate near the calcite surface have a large effect on the surface charge properties of calcite and thus on σ'' .

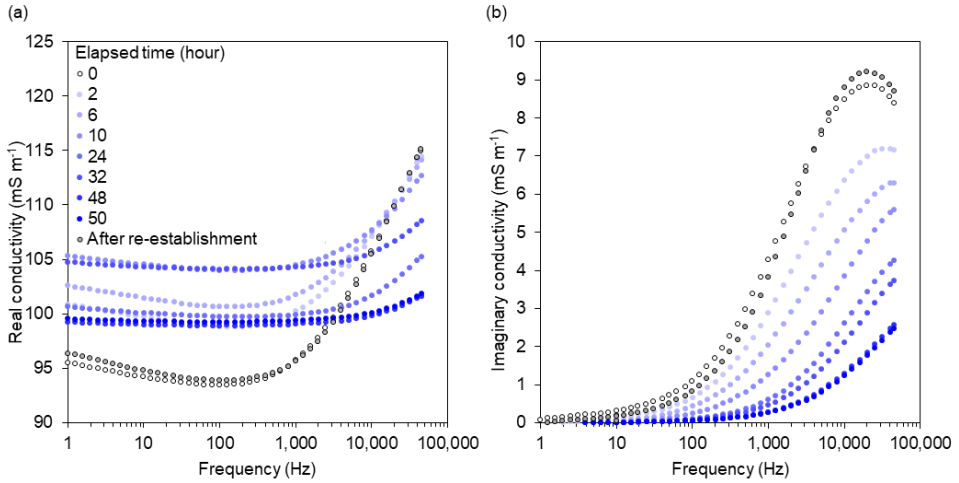


Figure 3.6. The development of (a) σ' and (b) σ'' as a function of time when solute injection was stopped in phase III. Open symbols represent the measured values before flow was stopped at $t=0$ h. Darker colour represents longer elapsed time. The grey symbols represent measured values after re-establishment of the condition at the start of this phase by injecting solution pair 2 of Table 3.2.

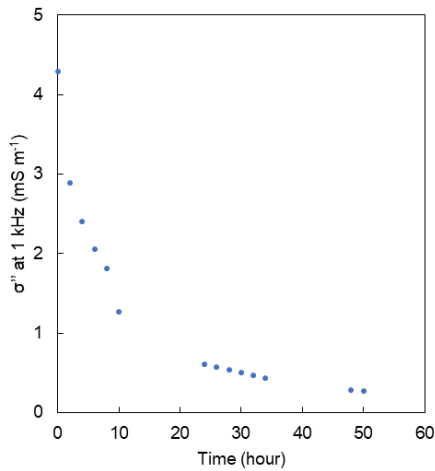


Figure 3.7. Change in σ'' at 1 kHz over time after stopping injection of both CaCl_2 and Na_2CO_3 solution in phase III.

3. Effect of solute concentration

In phase IV, the injection rate of the Na_2CO_3 solution was reduced. Compared to the streamlines in phase I and II (Figure 3.2a,b), this reduction shifted the mixing zone upward and slightly to the right (Figure 3.2c). σ' increased slightly during phase IV (Figure 3.8a) because the more conductive CaCl_2 solution occupied a larger volume of the sample. Again, σ'' was found to decrease strongly (Figure 3.8b) despite the slight increase in mean electric conductivity of the pore water. These results apparently contradict the results of phase II and III. However, it is important to realize that the pore water solution in contact with the calcite in phase IV was probably different from that in phase II and III because the mixing zone was moved as shown in the simulation results (Figure 3.2). Part of the calcite precipitated before phase IV is now only in contact with CaCl_2 solution, which has larger σ_w , lower pH, higher concentration of Ca^{2+} and lower concentration of carbonate species than the Na_2CO_3 solution. The observed decrease in σ'' can thus reasonably be explained by assuming that changes in solute concentration of the water in contact with the calcite affected the surface chemistry of the calcite. Although previous studies have shown a large variation in pH dependence of surface charges of calcite (Wolthers et al., 2008), it is generally agreed that a decreasing pH leads to an increase of protonation on the calcite surface. For example, Eriksson et al. (2007) showed that the net proton charge on the calcite surface strongly increased below a pH of 8. Since the pH of the CaCl_2 solution in the experiment was 6.64, this increase in proton charge may have decreased the number of negatively charged sites on the calcite surface and thus decreased the SIP response (Leroy et al., 2017). Because the calcite surface charge and the solute concentration near the precipitation front cannot directly be observed in the experimental setup, this will need to be examined in more detail in future work.

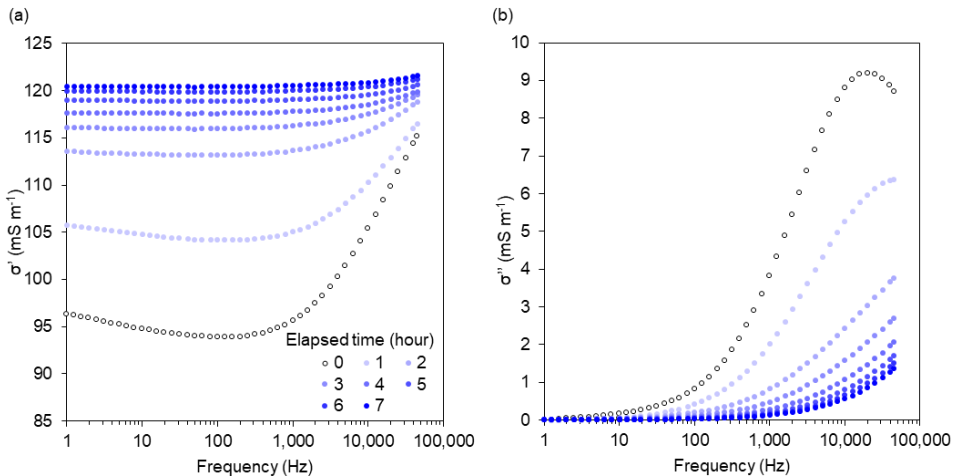


Figure 3.8. Development of (a) σ' and (b) σ'' when the injection rate of the Na_2CO_3 solution was reduced relative to that of the CaCl_2 solution. Darker colour represents longer elapsed time.

The results of the flow experiments in phase II, III and IV qualitatively showed that the SIP response of calcite precipitation depended on the solute concentration near the zone of calcite precipitation. A more quantitative analysis does not seem meaningful. One reason is that there was unexpected increase in maximum σ'' between the start of the phase II and III (3.5 mS m^{-1}) and between the start of phase III and IV (0.3 mS m^{-1}). This suggests that the amount of calcite precipitation increased after the start of phase II. It should be noted that σ'' decreased in each phase, thus the variation in σ'' was not attributed to the amount of calcite but to the solute concentration. The other reason is the unknown spatial distribution and kinetics of calcite precipitation in combination with the heterogeneity of the flow velocity field in the column. The most promising way forward towards a quantitative understanding of the SIP response of calcite precipitation requires a combination of reactive transport modelling with more advanced experimental setups that allow determining the distribution of calcite precipitation and solute concentration (e.g. a 2D millifluidic measurement set-up).

Despite the qualitative nature of the insights obtained here, it is interesting to evaluate the results of previous studies (Table 3.1) on the SIP response of calcite precipitation within the light of the current results. For example, Wu et al. (2011), Zhang et al. (2012) and Saneiyani et al. (2018) all reported significantly smaller SIP responses than presented in this study and Wu et al. (2010). Although part of the differences is certainly due to the different amounts of calcite precipitation in these studies, it is now clear that the concentration of Ca^{2+} and the carbonate species also need to be considered. In Wu et al. (2011), the Ca^{2+} and the total dissolved carbonate concentration in the influent solution were about 1 mM and 4 mM, respectively. These concentrations were much lower than the concentration of Ca^{2+} (29 mM) and dissolved carbonate concentration (26.2 mM) in the injected solutions in phase I of this study. Therefore, the concentration of Ca^{2+} and carbonate species in Wu et al. (2011) may not have been enough to generate a strong SIP response even in the presence of sufficient calcite precipitation. In Zhang et al. (2012), the concentration of Ca^{2+} and urea were 10 mM. Considering that the urease enzyme produces dissolved carbonate due to the decomposition of urea, the maximum concentration of carbonate species was 10 mM. However, Ca^{2+} adsorption on silica gel was strong as described in Zhang et al. (2012). Thus, the concentration of Ca^{2+} in the solution in contact with the precipitated calcite was probably not high enough to generate a significant SIP response. In the column experiment by Saneiyani et al. (2018), the distribution of calcite precipitation and solute concentration were not clear, and it may be possible that the calcite precipitation did not overlap with the mixing zone of the solutions. Based on this short survey of previous work, it seems likely that some of the observed weak SIP responses may be attributed to lower concentrations of Ca^{2+} and carbonate species in the solution in contact with the precipitated calcite in addition to potentially different amounts of calcite precipitation.

3.3. Conclusions

In this study, calcite precipitation was induced in a column by mixing Na_2CO_3 and CaCl_2 solutions and SIP measurements were made during a flow experiment composed of four phases. In phase I, a significant SIP response was observed due to the calcite precipitation induced in the column. In phase II, the column was flushed with solutions with a different saturation index and thus a different pore water conductivity. The results suggested that the SIP response of calcite has a stronger dependence on the solution conductivity than sand and sandstone. When the injection of both solutions was stopped in phase III, σ'' decreased. This was attributed to a decrease in the concentration of Ca^{2+} and CO_3^{2-} in contact with the calcite in the precipitation front. In phase IV, the injection rate of the Na_2CO_3 solution was reduced to shift the mixing zone away from the calcite precipitation front. Therefore, part of the calcite precipitation front generated in phase I was only in contact with the CaCl_2 solution. Despite a bulk increase in the electric conductivity of the pore water due to the more conductive CaCl_2 solution, it was observed that σ'' decreased. This was attributed to interactions between solute concentration and surface chemistry of the calcite. The experimental results presented here clearly highlighted the complex dependency of the SIP response of calcite precipitation on solute concentration. Based on the results, the previously observed relatively weak SIP responses of calcite precipitation (Sanciyan et al., 2018; Wu et al., 2011; Zhang et al., 2012) may be related to lower concentrations of Ca^{2+} and carbonate species in the solution in contact with calcite in addition to variable amounts of calcite precipitation. Future work should focus on obtaining a more quantitative understanding of the relationship between surface chemistry of calcite and SIP response. For this purpose, it is important to quantify how solute concentration affects the SIP response of calcite precipitation, which can only be obtained by a combination of advanced experimental set-ups, spatially resolved reactive transport modelling, and deterministic modelling of the SIP response.

Chapter 4

Millifluidic experiments to understand SIP response during calcite precipitation

In Chapter 3, column experiments were presented that suggest that the SIP response of calcite precipitation is largely controlled by the solute concentration near the calcite precipitation. One of the limitations of these column experiments is that essential information on the temporal development and spatial distribution of calcite precipitation is not available. Clearly, it would be beneficial if the calcite precipitation process could be observed directly to improve understanding of how calcite precipitation generates an SIP response. In this chapter, a novel SIP measurement set-up using a 2D millifluidic set-up will be used to investigate how the SIP response of calcite is controlled by the dynamic precipitation process. The main idea of this 2D millifluidic set-up is that the use of a 2D porous media makes it possible to visually observe calcite precipitation while making SIP measurements at the same time. Based on the obtained development of calcite precipitation, it is also possible to make electric field simulations for the 2D millifluidic set-up, which will help to understand the measured SIP response.

The organisation of this chapter is as follows. First, the design of the 2D millifluidic set-up including the visualization setup will be presented. After this, the experimental procedures, image calibration for precipitation height, and the electric field simulations will be introduced. Next, the development of calcite precipitation and the associated SIP response will be presented and interpreted using the electric field simulations. Finally, possible mechanisms explaining the polarization of calcite precipitation will be discussed.

4.1. Materials and methods

The novel SIP measurement set-up using a 2D millifluidic set-up consists of a sample holder with a 2D porous media, a SIP measurement system, and equipment for visualization of pore-scale processes (Figure 4.1a). In the following, each component of the setup is described in detail.

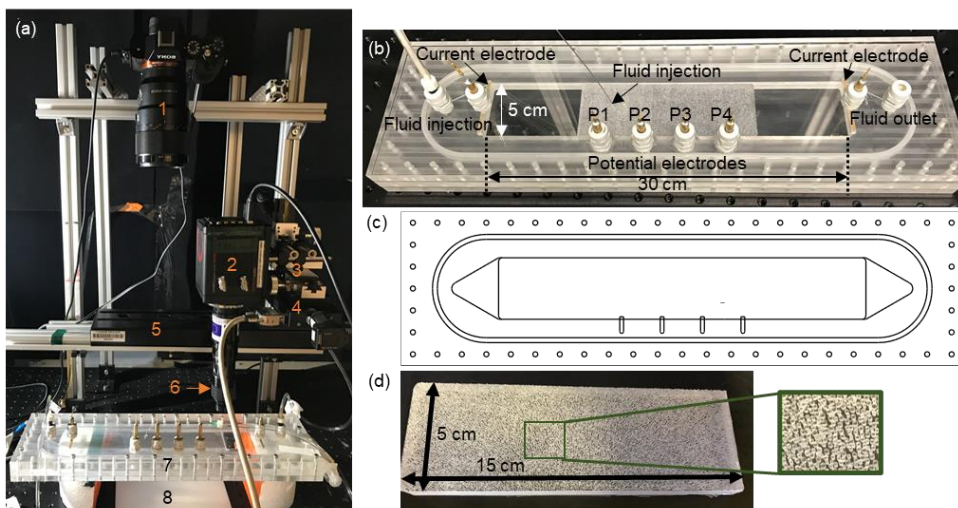


Figure 4.1. Overview of the experimental setup. (a) Entire setup including 1) overview camera, 2) high-zoom camera, 3,4) 3-axis stage, 5) 2-axis moving table, 6) lenses, 7) millifluidic set-up, 8) backlight, (b) sample holder with porous media and electrodes, (c) plan view of the middle plate of sample holder, and (d) 2D porous media made of PDMS.

4.2. Sample holder

A photo of the sample holder is shown in Figure 4.1b and technical drawings of the sample holder are shown in Figure 4.2. The sample holder was made of transparent poly(methyl methacrylate) (PMMA). The outer length, width and height of the sample holder were 450 mm, 125 mm and 33 mm, respectively. The sample holder consisted of three plates that were fixed together with screws using holes in all three plates. The bottom plate (height: 10 mm) was a flat plate. The middle plate (height: 11 mm) had a large rectangular cavity in the middle (length: 300 mm, width: 50 mm). This cavity was designed to hold the 2D porous media discussed in the next section. The top plate (height: 12 mm) covered the cavity holding 2D porous media. In the top plate, one hole with a diameter of 1 mm was positioned above the 2D porous media. A needle (diameter: 0.8 mm) was fixed in this hole with UV adhesive (Norland Optical Adhesive 68, Cranbury, NJ, USA) to inject fluid directly into the 2D porous media. To avoid that this

needle affects the SIP measurements, the top of the needle was cut off and the needle was retracted more than twice the inner diameter of the hole before it was fixed. The middle plate also had two triangular carved out areas (each side: 50 mm, depth: 1 mm) on both sides of the large rectangular cavity. An injection and outlet port were located near the end of this triangular area to ensure homogeneous fluid flow to the extent possible. When the top plate, middle plate and bottom plate were assembled together, a sample holder including a cavity, two fluid injection and one outlet port was obtained.

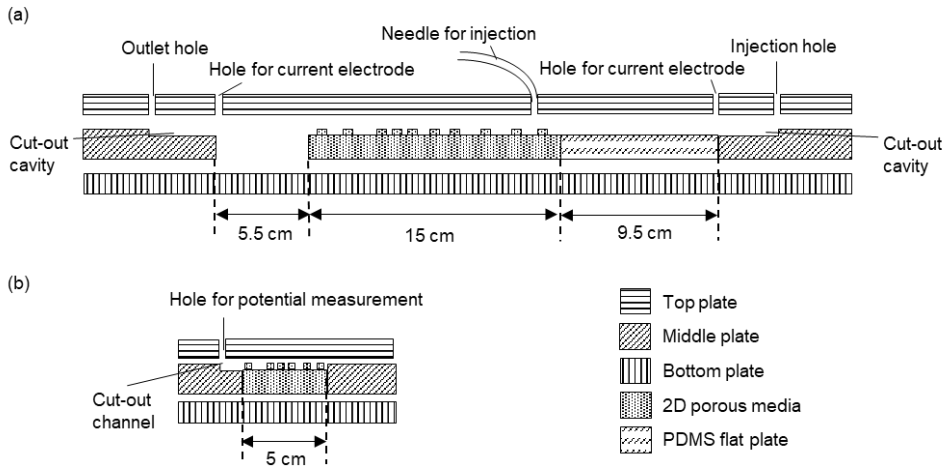


Figure 4.2. Cross-section of the sample holder in (a) flow direction and (b) perpendicular to the flow direction. The dimensions of the top plate, middle plate, bottom plate, PDMS flat plate and 2D porous media are given, and key features of the sample holder are also indicated. Please note that the vertical dimension is not to scale.

In order to make SIP measurements, two current electrodes and four potential electrodes were integrated in the sample holder design (Figure 4.2). The current electrodes were completely retracted in the top plate to avoid disturbance of the water flow and were positioned at both sides of the large rectangular cavity in the middle plate. The current electrodes were made of porous rectangular brass (length: 49.1 mm, width: 6.3 mm, depth: 3.7 mm). The use of rectangular (plate) electrodes instead of point electrodes for current injection ensures a more homogeneous electrical field distribution. Four potential electrodes were held in cable glands in the top plate to ensure water-tightness. The four potential electrodes were made of brass and had a diameter of 6.5 mm. The electrodes were positioned at one side of the porous media with equal spacing (33 mm) symmetrically distributed around the centre of the sample holder (see Figure 4.1c). To ensure an electrical connection between the cavity and the four potential electrodes through water-filled channels, the middle plate had four carved out channels (length: 12.5 mm, width: 2.5 mm, height: 1 mm) (see Figure 4.1c). To make sure that there is no electrode polarization during

4. Millifluidic experiments

the SIP measurements, the potential electrodes were retracted by 11 mm (twice the inner diameter of the inner small hole) following recommendations of Zimmermann et al. (2008) and Huisman et al. (2016). The measurement system of Zimmermann et al. (2008) (described in Chapter 2) was used for SIP measurements. The measurement frequency range was from 1 Hz to 45 kHz, and the injected voltage was 5V. With this set-up, the SIP response can be measured in different measurement zones by choosing different pairs of potential electrodes. The separation between the potential electrodes and the current electrodes was large enough to avoid capacitive coupling of the potential electrodes and effects of potentially heterogeneous contact impedances of the current electrodes.

4.3. 2D porous media

The soft lithography method was used to produce a 2D porous media made of Polydimethylsiloxane (PDMS) (SYLGARD 184 Silicone Elastomer Kit, Dow, Midland, MI, USA) in a similar way as in microfluidic experiments (e.g., Karadimitriou & Hassanizadeh, 2012). The PDMS liquid was first mixed with curing agent and then poured into a mold. The PDMS in the mold was cured at 60 to 70°C overnight. After the PDMS was solidified, the PDMS was taken out from the mold. The same mold was used to produce all 2D porous media used in this study. The obtained 2D porous media was composed of a base plate (length: 150 mm, width: 50 mm, height: 10.6 mm) and pillars (height: 1 mm). The grain size distribution, pore size distribution, and the pore throat length distribution of the 2D porous medium are shown in Figure 4.3. The porosity of the 2D porous medium was 0.59. The grain size ranged between 0.34 and 0.82 mm with a median grain size of 0.53 mm. The height of 1 mm for the pillars of the 2D porous media was carefully selected based on the following considerations. First, the electrical impedance of the 2D porous media should not be too high to avoid SIP measurement errors. For this reason, the height of the 2D porous media could not be too small. At the same time, it is important to ensure 2D water flow to the extent possible. Therefore, the height of the 2D porous media should be as small as possible. Based on the compromise between these two factors, a 2D porous medium height of 1 mm was selected. Importantly, the mean pore throat size was smaller than the height of the cylinders. Because of this unique aspect ratio, Taylor-Aris dispersion is expected to be dominant in horizontal rather than in vertical direction. Most previous studies with 2D porous media used a less favourable aspect ratio where dispersion in vertical direction dominated (e.g. de Anna et al., 2014). Therefore, it is anticipated that the flow field is closer to 2D than in many previous studies.

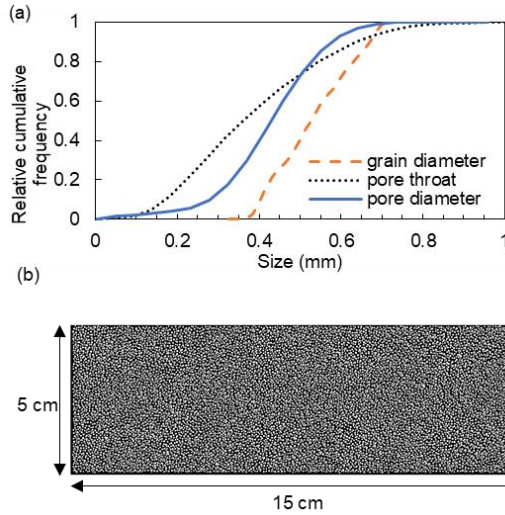


Figure 4.3. Cumulative distribution function for grain diameter, pore throat size and pore diameter size for the 2D porous media and (b) top view of 2D porous media (black: pore space, white: pillars).

4.4. Visualization of pore-scale processes

In order to monitor calcite precipitation at different spatial scales while measuring the SIP response, two different cameras were used (Figure 4.1). To improve image quality and achieve homogeneous lighting conditions, a light source (LFL-180BL2, CCS inc., Kyoto, Japan) was placed below the millifluidic set-up. The first camera was a regular mirrorless digital camera (14-bit, SONY alpha7s, SONY, Tokyo, Japan) equipped with a macro lens (MACRO GOSS F2.8/90, SONY, Tokyo, Japan) that was placed 40 cm above the millifluidic set-up, which resulted in a field of view of 16.6×11.0 cm and an image resolution of 0.03×0.03 mm per pixel. This (overview) camera was connected to a PC through a voltage output module (National Instruments, Austin, TX) to enable automatic image acquisition. The second camera was a high-zoom camera with high-sensitivity (16-bit, Hamamatsu ORCA flash 4.0, Hamamatsu Photonics K.K., Shizuoka, Japan) connected to the PC with a USB cable and a set of lenses (6.5X zoom lens with 2X extension tube and 1.5X lens attachment, Thorlab, Inc., Newton, MA, USA). This camera was fixed on a 3-axis table (Edmund Optics Ltd., Barrington, USA), which was mounted on a 2-axis motorized table. The 2-axis table was constructed by combining two 1-axis motorized tables (Edmund Optics Ltd., Barrington, USA and Thorlab, Inc., Newton, MA, USA) and allowed to automatically move the high-zoom camera in a horizontal plane 5.1 cm above the millifluidic set-up to monitor the entire measurement area between the potential electrodes ($5 \text{ cm} \times 10 \text{ cm}$). For this camera, the field of view was about $750 \times 750 \mu\text{m}$ and the image resolution was $0.37 \times 0.37 \mu\text{m}$ per pixel. Both cameras and the 2-axis motorized stage were controlled synchronously with a

4. Millifluidic experiments

custom-made program in Matlab (Mathworks, Natick, MA, USA). The composite images were created from the high-zoom images using an open source image processing program ImageJ with the plugin TrackEM2.

4.5. Experimental procedure

In order to perform flow and reactive transport experiments, the sample holder and 2D porous media were assembled. Due to the different size of the cavity in the middle plate and the 2D porous medium, an additional PDMS plate (length: 95 mm, width: 50 mm, height: 10.6 mm) was placed in the upstream part of the rectangular cavity before the 2D porous medium (Figure 4.2). This additional plate ensured a homogeneous flow field, decreased the volume of the cavity and made it easier to replace the solution in the porous media when needed, and ensured consistent positioning of the porous media in all experiments. The downstream cavity (11 mm height, 5.5 cm length) was not filled and served as space to collect mobile calcite precipitates that would otherwise clog the fluid outlet port. To avoid water and electric current flow outside the porous media, the gaps between the porous media and the side of the cavity in the middle plate were closed using UV adhesive. The gaps between the middle plate and top/bottom plate were filled with Vaseline. It should be noted that the height of the porous media (11.6 mm) was slightly larger than the height of the cavity in the sample holder (11.0 mm). This naturally caused a little compression of the porous media (5% of the total height) during assembly. Therefore, there was no gap between the top of the cylinders of the porous media and the bottom of the top plate of the sample holder.

Two replicate calcite precipitation experiments with a total duration of 70 and 80 hours, respectively, were performed. For each experiment, the measurement cell was first flushed with CO₂ gas and then filled with 26.2 mM CaCl₂ solution in all experiments. During filling of the porous media with the solution, some gas bubbles were trapped in the pore space. Since CO₂ easily dissolves in water, all gas bubbles disappeared after some minutes. After preparing the water-saturated measurement cell, the millifluidic set-up was placed on two pieces of styrene foam (height: 5.5 cm) in the visualization setup to avoid capacitive leakage currents between the millifluidic set-up and the metallic base plate during the SIP measurements. Next, 26.2 mM CaCl₂ solution was injected through the injection port at the side of the 2D porous medium and 29 mM Na₂CO₃ solution was injected through the injection port in the middle of the porous medium. Both solutions were injected with the same flow rate (4 mL h⁻¹) using a syringe pump (model 22, Harvard Apparatus, Inc., Holliston, MA, USA). It should be noted that a small amount of NaCl solution (~0.5 mL) was filled in the tube of the injection port in the middle of the porous medium before the start of the experiment to prevent mixing of Na₂CO₃ and CaCl₂ solution and associated precipitation before the start of the experiment.

As discussed in Chapter 3 already, mixing of Na₂CO₃ and CaCl₂ solution induced calcium carbonate precipitation according to:



Precipitation was expected to be mainly induced in the zone where the two injected solutions mixed. SIP measurements were made in three measurement zones, which will be referred to as the upstream, middle, and downstream measurement zone, using the electrode pairs P1 and P2, P2 and P3, and P3 and P4 respectively (Figure 4.4b). SIP measurements were made from 1 Hz to 45 kHz every 18 minutes in the upstream zone and every 8 hours in the other zones. Digital images were taken every 8 minutes with the overview camera with a large field-of-view for the entire measurement region and with the high-zoom camera for four selected positions. Two of these positions were located in the upstream zone and the other two positions were located in the middle and downstream zones. The four positions were all located on one side of the sample holder because of the expected symmetry in the mixing zone between the two solutions perpendicular to the flow direction. At each position, the high-zoom camera took 10×10 images with a regular space interval using the motorized stage. After stitching the images together, this resulted in a composite image with a size of about 7.5 mm×7.5 mm. At the end of the experiment, the high-zoom camera was also used to obtain images of calcite precipitation along the mixing front.

After the experiment, the 2D porous media was removed from the sample holder to measure the height of the precipitation using a profilometer (Altisurf 500, Altimet, France) with a vertical resolution of 5 μm and a horizontal resolution of 50 μm. These height measurements were used to establish a calibration function between image grey level and the height of the precipitation as described in detail in the next section. The calcite precipitation in the 2D porous media was also investigated by a microscope with 10X and 40X lenses after the experiment (Inverted Laboratory Microscope, Leica microsystems, Cambridge, United Kingdom).

The effect of solute concentration was not considered in this first set of replicate experiments, although the results in Chapter 3 suggested that solute concentration strongly influenced the SIP response of calcite precipitation. To obtain additional insights in this aspect, an additional experiment was performed. To prepare the solution for this experiment, 26.2 mM MgCl₂ solution and 29.0 mM Na₂CO₃ solution were mixed, which resulted in MgCO₃ precipitation that was removed by centrifugation. The supernatant solution was used in the additional experiment, and will be referred to as MgCO₃ solution in the following. This solution was selected for three reasons. First, the expected reactivity of Mg²⁺ with calcite is quite low. For example, magnesium-bearing calcite with Mg contents higher than 10 mol% is a thermodynamically unstable phase of calcium carbonate under ambient conditions (Yang et al., 2016), formation of dolomite and magnesite are virtually impossible at ambient temperature (Montes-Hernandez et al., 2016), and dissolution of calcite is inhibited by the presence of Mg²⁺ (Arvidson & Mackenzie, 2000). Second, Mg²⁺ is expected to adsorb on the surface of calcite with high affinity (Al Mahrouqi et al., 2017). Third, the solubility of amorphous MgCO₃ is substantially higher than that of amorphous CaCO₃ (Purgstaller et al., 2019). This results in higher concentration of Mg²⁺ and the carbonate species in the mixed solution of MgCl₂ and Na₂CO₃, compared to the Ca²⁺ and the carbonate

4. Millifluidic experiments

species in the mixed solution of CaCl_2 and Na_2CO_3 . From the second and third reasons, it can be expected that chargeability of calcite surface is high in MgCO_3 solution. This high chargeability is expected to induce a large SIP response according to the grain polarization model of calcite (Leroy et al., 2017, Chapter 2). At the start of the additional experiment, calcite precipitation was first induced in the same way as described above. The monitoring strategy for digital image collection and SIP measurements was also identical to the procedures described above. After 47 h and 87.5 h, the two injected solutions were changed to the MgCO_3 solution described above in the middle of the precipitation process. After the SIP response stabilized in response to the injection of MgCO_3 solution (after ~ 16 pore volumes), the original Na_2CO_3 and CaCl_2 solutions were injected again. About 27 pore volumes of Na_2CO_3 and CaCl_2 solution were sufficient to obtain a SIP response similar to that before the injection of MgCO_3 solution.

4.6. Image processing

Calcite precipitation was expected to build up from the bottom to the top. The height of the precipitation cannot be directly observed using the digital images acquired from the top view. However, the grey scale of the digital image was expected to be related to the height of the precipitation because calcite is partly transparent. In order to acquire the relationship between grey level of the image and the height of the precipitation, the spatial distribution of the height of the precipitation obtained with the profilometer was used. In particular, the height of the calcite precipitation and the grey level of the digital image acquired with the top-view camera were used to obtain a calibration relationship based on four selected areas. These areas were selected based on the following two criteria: i) precipitation was intact after opening of the measurement cell for profilometer measurements, ii) a wide range of precipitation height was present in the selected area. Within each selected area, the 3D geometry of the precipitates obtained with the profilometer was downscaled to obtain the same image resolution as the digital image. Because of the height of the porous media, the measured and predicted height of the precipitates should range between 0 mm and 1 mm. In order to achieve this, the following procedure was used to establish a calibration relationship. First, precipitation height h was converted using:

$$h' = \tan\left(\frac{h + 0.05}{2} \times \pi\right) \quad (4.2)$$

Here, h was increased by 0.05 in order to avoid values near $\pm\pi/2$, where the tangent function is extremely sensitive. Next, the relationship between h' and grey level (I), which ranged from 0 to 255, was fitted using a linear function:

$$h' = aI + b \pm \varepsilon \quad (4.3)$$

where a and b are the fitting parameters. The predictive uncertainty (ε) was obtained for this linear regression function. In order to obtain a function that relates grey level to height of the precipitates, the inverse formulation was used considering the error propagation:

$$h = \frac{\arctan(al + b)}{\pi} - 0.05 \pm \frac{\varepsilon}{\pi(1 + (al + b)^2)} \quad (4.4)$$

Here, h does not take a value over 1 nor below 0 if errors were not considered. This relationship was applied to all the photos taken by the overview camera during the experiment to obtain the temporal and spatial change in the height of the precipitation. Based on this information, the change in the total volume of calcite in the measurement zone, the distribution of calcite precipitation height, and the spatial distribution of the development of calcite in longitudinal direction (x direction) were derived. For the calculation of the development in longitudinal direction, the area was first discretised in slices of 0.03 mm based on the image resolution. Then, the sum of the volume of precipitation was calculated for each slice.

4.7. Simulation

In order to study how the distribution of calcite precipitation affects the SIP measurements, additional electrical field simulations were performed. For this, a custom-made finite-element modelling approach implemented in Matlab (Mathworks, Natick, MA, USA) was used. The governing equation that was solved was:

$$\nabla \cdot J = \nabla \cdot (\sigma^* \nabla \varphi^*) \quad (4.5)$$

where φ^* is the complex potential (V) and σ^* is complex conductivity ($S \cdot m^{-1}$). The modelling domain was the rectangular area between the current electrodes (30 cm \times 5 cm) (Figure 4.1b). Constant electric current was injected from right boundary and ejected from the left boundary. The domain was discretised in right-angled triangles with a leg length of 2 mm. Because it was not computationally feasible to use a mesh fine enough to resolve the pore scale, effective properties need to be assigned to different areas. For this reason, the simulations were only used to analyse qualitative trends in the following. For the effective electrical conductivity of the background, only a real conductivity ($S \cdot m^{-1}$) was used, which was determined based on the solute concentration and the formation factor. The shape of the area with calcite precipitation was obtained from images obtained with the overview camera. The effective complex conductivity of this area was described using the Cole-Cole model:

$$\sigma^* = (1 - m)R_\sigma \sigma_{bulk} \frac{1}{1 - m \left(1 - \frac{1}{1 + (2\pi f T i)^c} \right)} \quad (4.6)$$

where m is the chargeability, f is the frequency (Hz), T is characteristic time (s), c is a shape exponent, R_σ defines the ratio between the high-frequency limit of the conductivity, σ_∞ , and the bulk conductivity σ_{bulk} :

$$R_\sigma = \frac{\sigma_\infty}{\sigma_{bulk}} < 1 \quad (4.7)$$

4. *Millifluidic experiments*

The parameters of the Cole-Cole model were selected such that the simulation results were in reasonable agreement with the experimental results.

4.8. Results and discussion

4.8.1. Precipitation process

Figure 4.4 shows examples of digital images acquired with the overview camera and the high-zoom camera. The large-scale images (Figure 4.4, left column) clearly show that part of the images got darker over time. This is associated with calcite precipitation that was generated at the boundary of the two injected solutions. The shape of the boundary corresponds with the streamlines of Rankine half-body flow, as expected given that a point source was placed in a uniform background flow. The images also showed that the overall shape of the precipitation front did not change over time. This indicates that the flow was well controlled over the whole region and that there was no strong feedback of the calcite precipitation on the position of the reaction front. The composite images obtained from the high-zoom images show that some regions with calcite precipitation were darker than other regions (Figure 4.4, middle column) and that the position of these darker regions did not change during the experiment. This again confirms that the flow was well controlled, even at the pore scale. The high-zoom images successfully captured the development of individual crystals (Figure 4.4, right) and it can also be seen that more and larger calcite crystals were formed in the darker regions. The larger amount of reaction product suggests that reaction rates were higher in darker region. Figure 4.5 shows microscopic images from the darker region obtained after the experiment. Here, it seems that calcite precipitation created a solid wall (Figure 4.5a,b). Figure 4.5c shows microscopic images of this wall of calcite precipitation from the side. It has a wavy striped structure with grains of crystals at the bottom (Figure 4.5c in white circle). Even at this small scale, no pores can be observed in the precipitates. This lack of pores is likely related to the precipitation process. The solutions used in this study were strongly oversaturated with respect to calcite. This leads to instantaneous generation of amorphous calcium carbonate when the two solutions were mixed (Rodríguez-Navarro et al., 2016). This amorphous calcium carbonate likely settled on the bottom of the sample holder due to its higher density. According to Morse et al. (2007) and Rodríguez-Navarro et al. (2016), the amorphous phase of calcium carbonate is able to attach on calcite surfaces and allows calcite precipitates to grow further. In this process, it seems likely that calcite precipitation walls without pores were formed along the entire precipitation front. Based on the image analysis up to this point, it is concluded that the creation of a solid calcite precipitation front occurred along the mixing front, and that the position of calcite precipitation did not change with time, even at the pore scale.

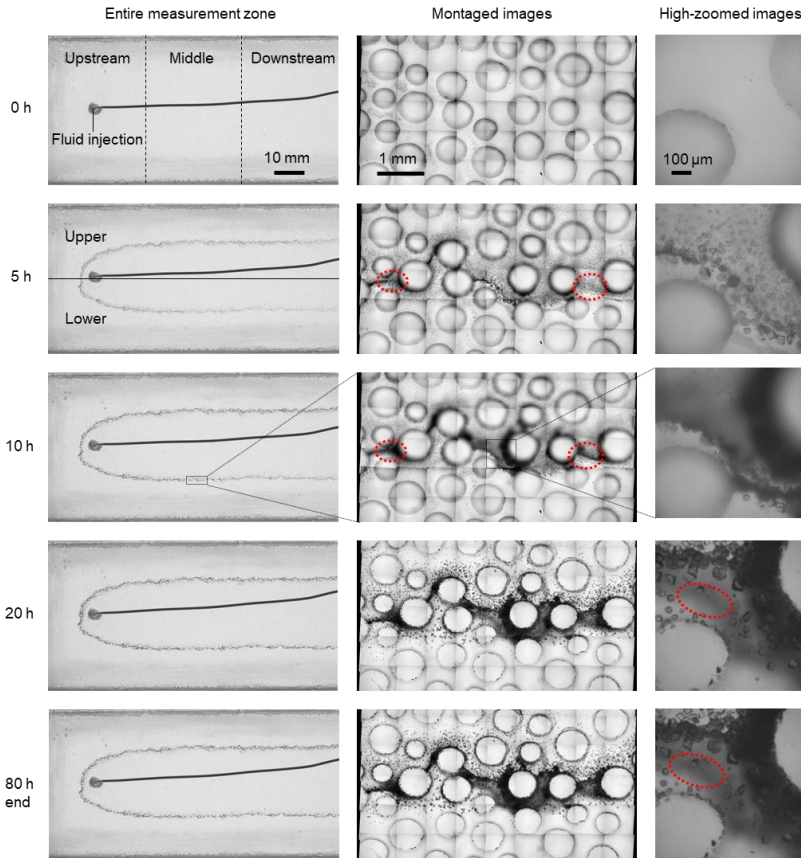


Figure 4.4. Digital images taken at different times for the entire measurement area (left column), a selected area along the calcite precipitation front in a composite image (center column) and calcite crystals in high-zoom images (right column).

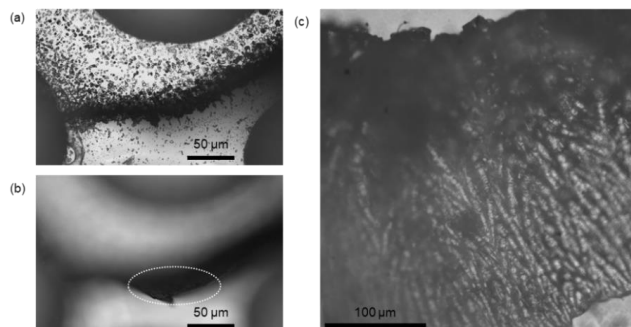


Figure 4.5. Microscopic images of calcite precipitates (a) top view with the focus set on the bottom of the 2D porous medium, (b) top view with the focus set on the top of the calcite precipitation and (c) side view.

4. Millifluidic experiments

In a next step, the relationship between the grey level of the image and the height of the precipitation from the profilometer was obtained (Figure 4.6). A large scatter was observed in this relationship. Considering that the calcite crystal was almost transparent, the grey level of the images was mostly determined by the amount of edges of the calcite grain that scattered light. The height of the precipitation was therefore only indirectly related to the grey level in the image, which likely explains the large scattering. The fitted calibration curve (equation (4.4)) and the associated prediction intervals are also shown in Figure 4.6. If it is assumed that the porosity of the calcite precipitation was negligible, this calibration curve can directly be used to obtain the spatial distribution of the precipitation volume from the grey level in the images.

After establishing the calibration relationship, it was first analysed how the total volume of calcite precipitation increased as a function of time (Figure 4.7a). It can be seen that the total volume of calcite precipitation strongly increased up to 20 hours, and only slowly increased afterwards. Image analysis suggested that the rate of calcite precipitation was higher in the upper half than in the lower half of the images (Figure 4.7a). This is important because the potential electrodes were located on the upper side of the images (see Figure 4.4, top left). Image analysis was also used to analyse the development and distribution of calcite precipitation height. Figure 4.8a shows the change in the sum of the volume from 0 mm to a given height as a function of time. This change in the cumulative volume of calcite precipitation suggests that the height of the precipitation increased mostly up to around 20 h and that the height did not change strongly afterwards. This suggests that there was no strong re-distribution of calcite though dissolution and precipitation after 20 h. This is consistent with the observed development of the total volume of calcite in Figure 4.7. Because of this consistent change in the development of calcite precipitation before and after 20 h, these two periods will be considered in more detail separately in the following.

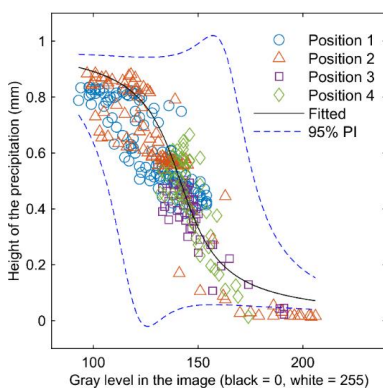


Figure 4.6. Relationship between image grey level and the height of the precipitation from the profilometer and the fitted calibration curve to calculate height of precipitation from image grey level with 95% prediction intervals.

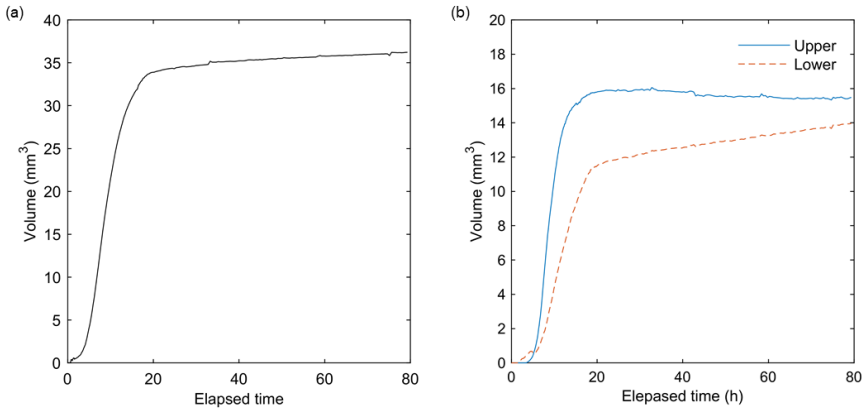


Figure 4.7 (a) Change in mass of precipitation over time in the entire measurement zone. (b) Change in mass of precipitation in the upper (near potential electrodes) and lower half of the measurement setup in Figure 4.4.

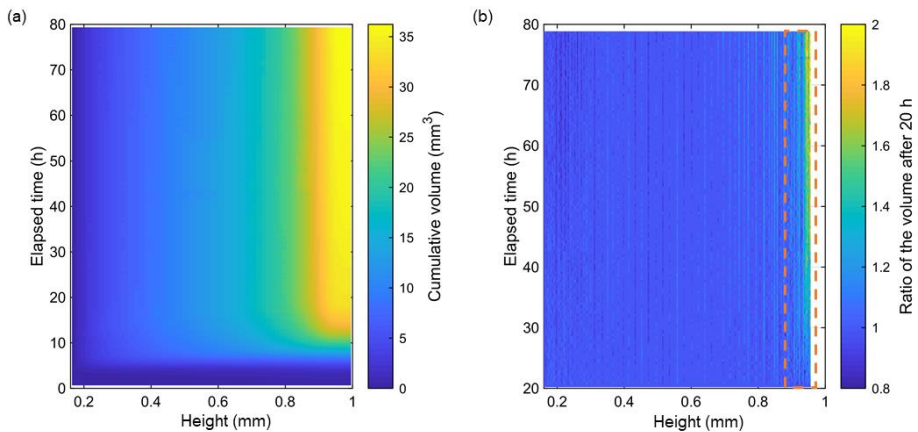


Figure 4.8 (a) Cumulative volume of calcite precipitation at a given height as a function of time. (b) Cumulative volume of calcite precipitation at a given height as a function of time normalized with the volume at 20 h.

The spatial distribution of the development of calcite before 20 h is shown in Figure 4.9, where the times when 50% and 95% of the volume at 20 h is reached is provided as a function of the distance from the upstream stagnation zone of the Rankine half-body flow (referred to as t_{50} and t_{95} afterwards). It can be seen that t_{50} and t_{95} were highly variable in space for both the upper and lower branch of the

4. Millifluidic experiments

precipitation front. This suggests that calcite precipitation happened heterogeneously at the pore scale. This was further confirmed using the high-zoom images. Figure 4.10 provides close-up images of the red circles in the composite images provided in Figure 4.4. It can be seen that the wall of calcite precipitation generally extended in downstream direction at the pore scale, but that the timing of this downstream extension was different in each pore.

The development of the height of the precipitation after 20 h was also investigated. Figure 4.8b shows the volume of calcite precipitation normalized with the volume at 20 h at a given precipitation height. This analysis shows that the volume only increased further in areas where a high wall of precipitation was already present after 20 h (i.e. continued vertical development of the calcite wall). This is also supported by the high-zoom images in Figure 4.10, where it can be seen that the grey level still increased after 20 h (Figure 4.10c). The high-zoom images also showed that the size of the crystals near the top of the flow domain did not change after 20 h (Figure 4.4), which suggests that the reaction was not very strong at this position after 20 h. Although direct observations of this slow development of the calcite wall were not possible because the high-zoom camera was not focused on the top of calcite wall continuously, the reduced speed of this process with time can be supported conceptually. In the selected experimental approach, the calcite precipitates divided the two injected fluids (Figure 4.11) and precipitation is expected to occur in the mixing zone. As the height of the calcite precipitation increases, the size of this mixing zone is reduced. This will lead to a decrease in the reaction rate and a reduced growth of the height of the calcite precipitation. This feedback mechanism between the reaction rate and the height of the calcite precipitation may thus lead to a slow but continuous growth of the volume of calcite precipitation even after 20 h (Figure 4.7a).

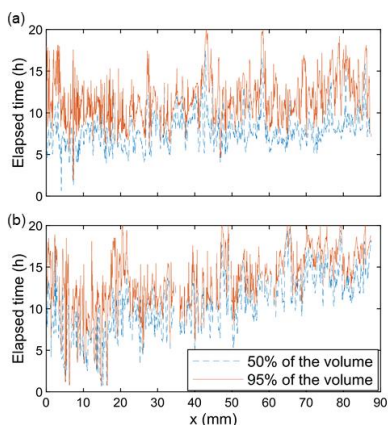


Figure 4.9. Spatial distribution of the development of calcite precipitation before 20 h as a function of distance along the precipitation front for the a) upper and b) lower branch of the precipitation front. The lines indicate the time required to reach a given percentage of the volume of calcite precipitation at 20 h.

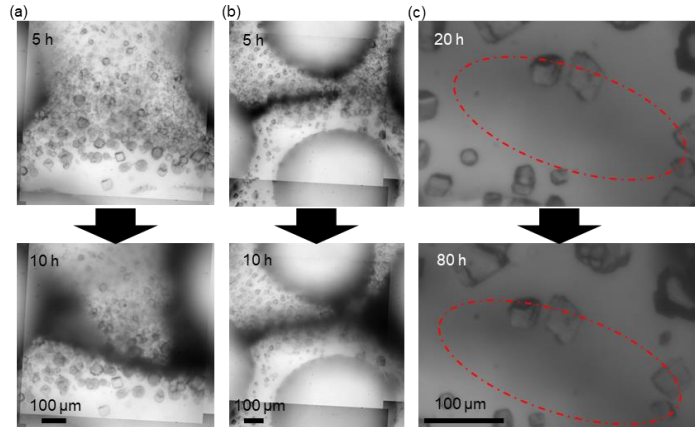


Figure 4.10. High-zoom images that exemplify calcite wall extended in downstream direction (a,b) and continued vertical development of the calcite wall (c).

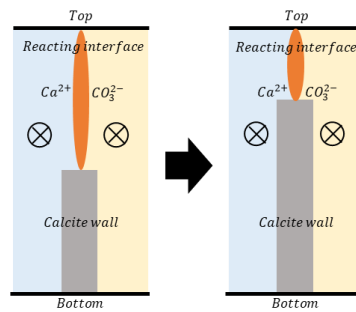


Figure 4.11. Conceptual model to explain reduced speed of calcite precipitation during the formation of the calcite wall. The colours represent the zone with CaCl_2 solution (blue), the zone with Na_2CO_3 solution (yellow), calcite wall (grey) and the mixing zone (orange).

The high-zoom images of the entire precipitation front taken at the end of the experiment showed that the size of the crystals was around $50\ \mu\text{m}$ in the entire measurement zone (Figure 4.12). This suggests that crystal nucleation proceeded equally along the precipitation front due to similar reaction rates and duration. Even though the timing of the start of calcite precipitation differed depending on the location as shown in Figure 4.9, it seems that this did not have a strong influence on the nucleation process and the final size of the calcite crystals.

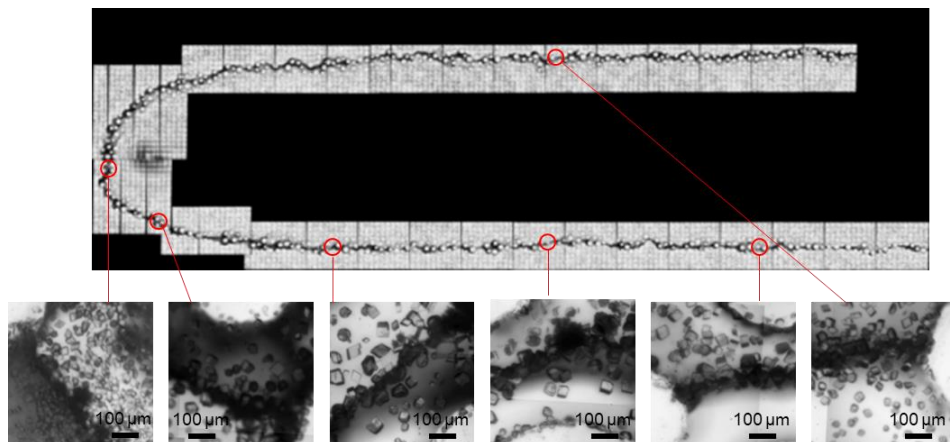


Figure 4.12. High-zoom images showing calcite crystals in different parts of the measurement domain.

4.8.2. SIP response

Figure 4.13 shows the real and imaginary part of the electrical conductivity (σ' and σ'' , respectively) as a function of time in different measurement zones (see Figure 4.4). It was found that σ' increased substantially with frequency, which indicates the occurrence of dielectric polarization processes. At the start of the experiment, the difference in σ' at 1 Hz of the three measurement zones was less than 5%. In addition, the σ'' was almost zero up to 10 kHz without any peak for all zones. In all three measurement zones, a clear peak in the σ'' appeared after about 16 h, which subsequently increased with time. The peak frequency was higher in the upstream measurement zone. It should be noted that relatively strong negative σ'' values were measured in the low frequency range in the upstream measurement zone. Such negative σ'' values are not physically possible for homogeneous samples, but can occur in the case of heterogeneous samples as will be shown in the numerical simulations presented later. In the case of σ' , larger changes were observed for lower frequencies than for the higher frequencies after 16 h. These temporal developments of the SIP response will be discussed later after a more detailed analysis of the data.

A duplicate experiment showed a similar SIP response as described above (Figure 4.14). In the middle and downstream measurement zones, the σ' and σ'' were very close to the values in the first experiment at the same elapsed time with differences below 10 mS m^{-1} and 1 mS m^{-1} for the real and imaginary part most of the time. The relatively large difference in σ' and σ'' for the upstream measurement zone are attributed to small difference in the flow field, which have the strongest impact in the upstream

measurement zone. However, the trend was also similar for the upstream measurement zone for the two experiments.

In order to analyse the SIP response in more detail, several characteristics were determined for further analysis. Figure 4.15a and Figure 4.15b provide the frequency and the associated value of σ'' for the observed peak in σ'' as a function of time for the three measurement zones for both the original and the duplicate experiment. The value of σ'' at the peak frequency strongly increased with time. It is important to note that although the volume of precipitation strongly increased up to 20 hours (Figure 4.7), the increase in σ'' was much smaller in that period. In fact, the value of σ'' at the peak frequency strongly increased after 24 h, but the volume of the precipitation changed only slightly. This clearly suggests that the SIP response is not only sensitive to the amount of calcite precipitation.

It was also found that the peak frequency was higher in the upstream measurement zone close to the injection point and that the peak frequency was relatively constant in time (Figure 4.15a). Based on previous theoretical studies (Leroy et al., 2017, Chapter 2), it is tempting to interpret such differences in peak frequency in terms of different size of the calcite crystal. However, the size of the crystals was similar in all three measurement zones according to the high-zoom images taken at the end of the experiment (Figure 4.12).

Figure 4.15c and Figure 4.15d show the change in σ' at 1 Hz and 10 kHz over time in the three measurement zones. The initial drop of σ' at time 0 h in all the measurement zones was due to the start of the injection of Na_2CO_3 solution, which has a lower electrical conductivity than the initial solution (CaCl_2). At the same time, the precipitation reaction started and also decreased the ion concentration and thus the electrical conductivity. Based on the flow rate of the injection, it only takes about 1.25 h to replace the background CaCl_2 solution with the Na_2CO_3 solution. Thus, the change in σ' between 1.25 and 20 h can only be attributed to the formation of the calcite precipitation. The formation of calcite precipitates may decrease σ' because calcite is non-conductive in the frequency range of SIP measurements. On the other hand, σ' may increase due to the lower reaction rate and the associated higher ion concentrations in the solution. Thus, the interpretation of σ' is challenging for the period before 20 h. After 20 h, there was no intensive reaction anymore, and a large increase in σ'' was observed. At the same time, the σ' at 10 kHz was almost constant and the σ' at 1 Hz decreased over time. These different trends of σ' between 1 Hz and 10 kHz after 20 h may be the key to understand how the SIP response increased, and this will be explored in more detail later.

4. Millifluidic experiments

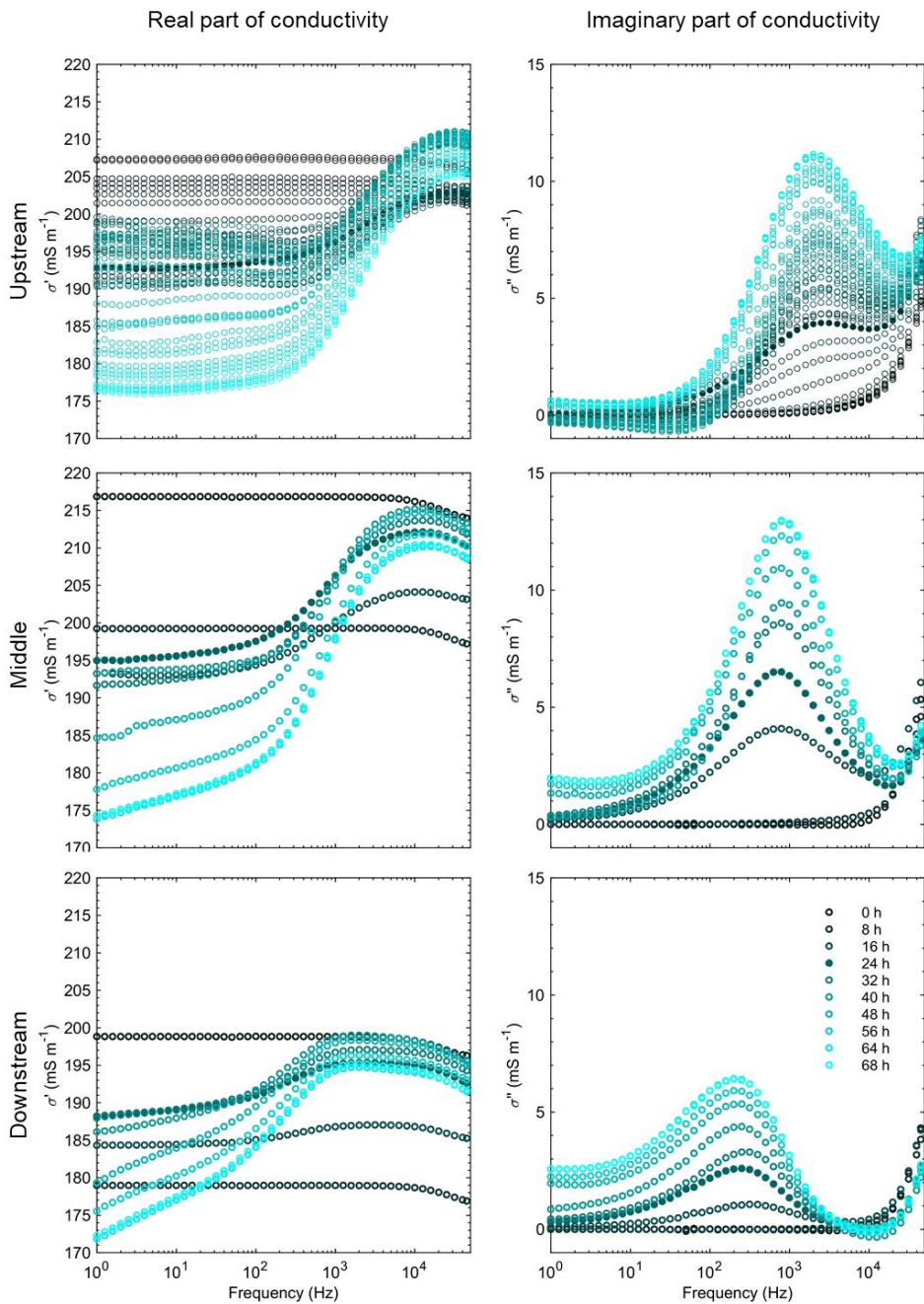


Figure 4.13. SIP response as a function of time for the three different measurement zones in experiment I.

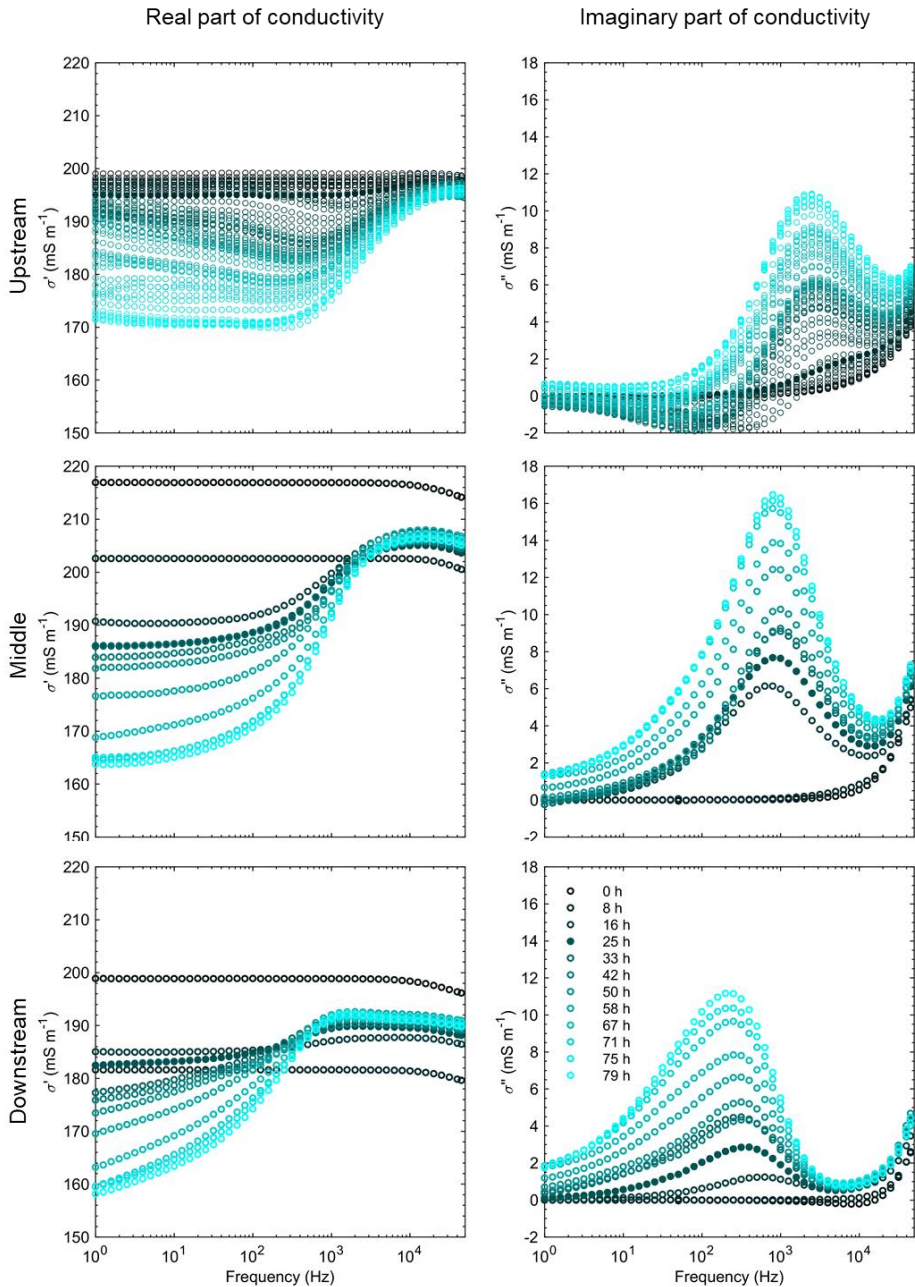


Figure 4.14. SIP response as a function of time for the three different measurement zones in the duplicate experiment II.

4. Millifluidic experiments

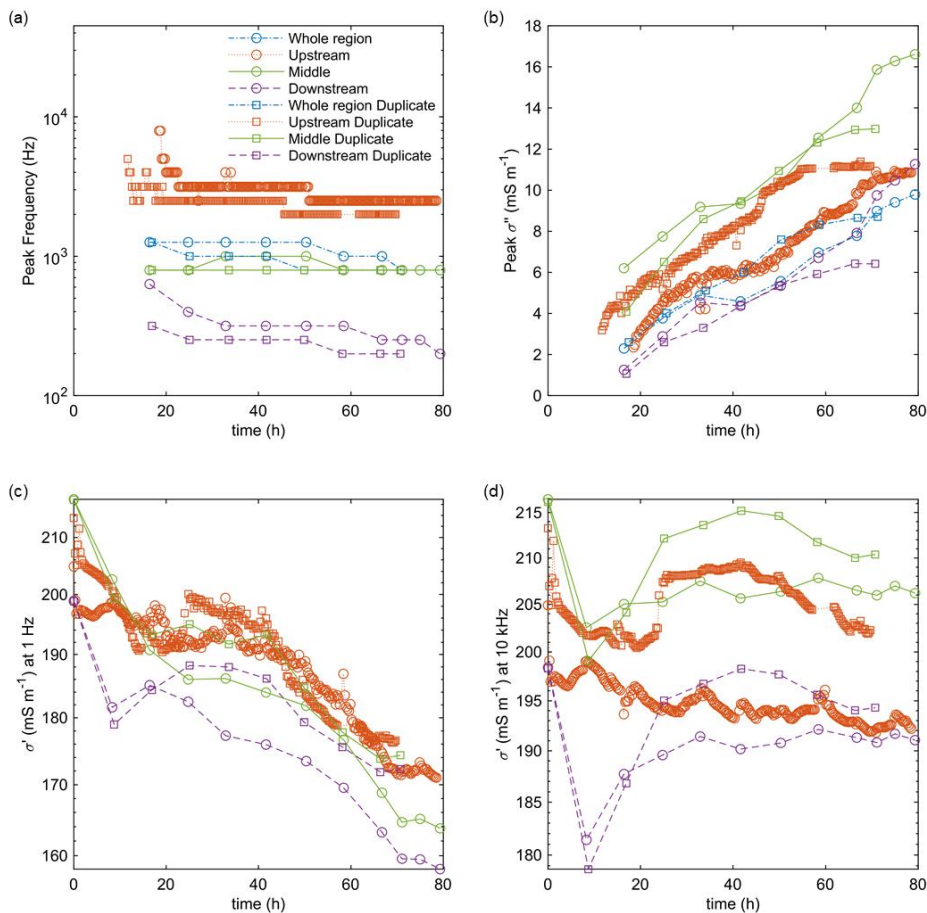


Figure 4.15. Key characteristics of the SIP response as a function of time for the three measurement zones: (a) peak frequency, (b) σ'' at peak frequency, (c) σ' at 1 Hz and (d) σ' at 45 kHz.

4.8.3. SIP response of calcite precipitation in homogeneous solution

The SIP response presented in the previous section was affected by spatial and temporal variations in solute concentration because of the ongoing precipitation reactions. In order to avoid such variations, an additional experiment was performed where the measurement cell was flushed twice with MgCO_3 solution after first generating calcite precipitation. The development of the image grey level followed a similar behaviour as in the previous experiment (Figure 4.16). It is assumed that this behaviour represents the same two stages of the calcite precipitation process as discussed in the previous sections. First, a continuous wall of calcite precipitation is created before 20 h. After this, there only is an increase

in the height of the already established calcite wall. Figure 4.17 shows the development of σ' and σ'' as a function time. It should be noted that periods when MgCO_3 solution was present in the measurement cell are not considered in this figure. It can be seen that both σ' and σ'' changed in a similar way as in the experiments presented in the previous section. As was already evident from the similarity of the duplicate experiments, this indicates that the experimental conditions in this experiment were sufficiently similar to the previous experiments. In addition, only small changes in σ' (less than 5%) and σ'' (less than 10% for peak magnitude of middle and downstream regions) were observed before and after injecting MgCO_3 solution. This suggests that the effect of the presence of MgCO_3 solution on the calcite surface properties was probably reversible and did not change the crystal properties. Also, the high-zoom images did not show much difference in crystal shape. This was expected because calcite reacts only slowly with magnesium ions (Arvidson & Mackenzie, 2000).

Figure 4.18 shows the σ' and σ'' for calcite precipitation in contact with MgCO_3 solution. The σ'' increased between the first and second injection of MgCO_3 solution, which suggests that σ'' increased with increasing calcite wall height after 20 h. Also, the peak frequency in the upstream region was higher after injecting MgCO_3 solution. These observations suggest that the SIP response of calcite precipitation is not only due to a heterogeneous distribution of solute concentration. In Chapter 3, it was already shown that the SIP response of calcite precipitation is sensitive to the solute concentration around it. The results presented here show that the SIP response of calcite precipitation is also sensitive to other factors, which will be discussed later.

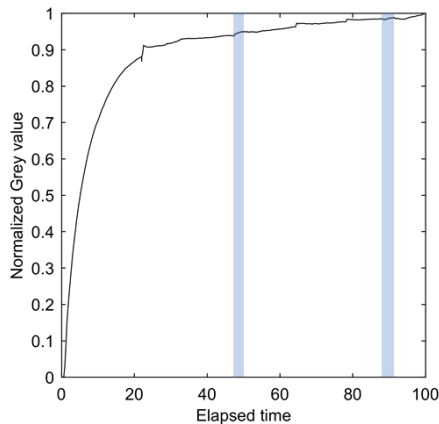


Figure 4.16. Change in normalized grey level in the entire measurement zone in the experiment with intermediate injections with MgCO_3 solution (blue zones).

4. Millifluidic experiments

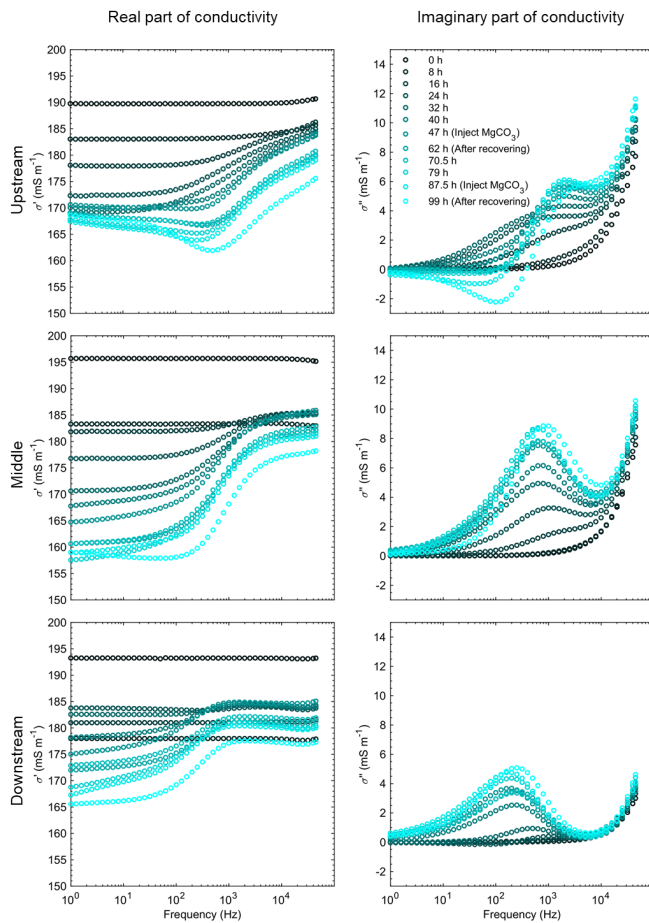


Figure 4.17. SIP response as a function of time for the three measurement zones in the experiment with intermediate injection of MgCO_3 solution.

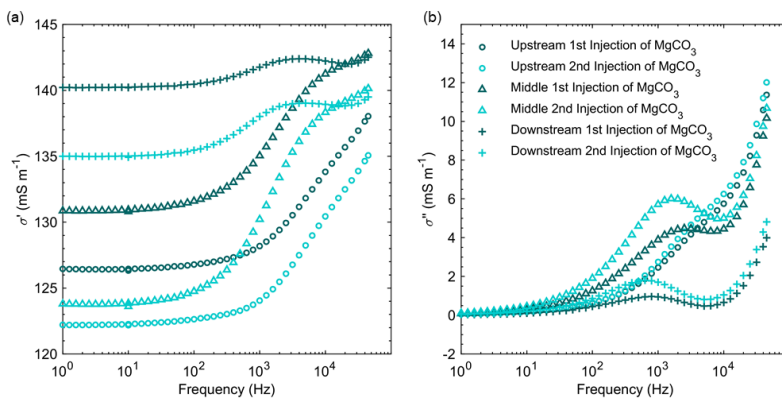


Figure 4.18. SIP response after the first and second injection of MgCO_3 solution.

4.8.4. Electrical field simulations

In the previous sections, the experimental results were shown including some unexplained features in the observed SIP responses. In particular, negative σ'' values and differences in peak frequency were observed for different measurement zones. In this section, it will be explored to what extent the spatial arrangement of the calcite precipitation affects the SIP response using electrical field simulations. Figure 4.19 shows the three simulation scenarios that will be considered. Figure 4.19a corresponds to the experimental period after 20 h where a clear and continuous precipitation front was observed. In this scenario, the background electrical conductivity was 0.162 S m^{-1} based on the measured formation factor and the solute conductivity. The complex electrical conductivity of the calcite was defined using a Cole-Cole model. To determine suitable Cole-Cole model parameters to reproduce the observed SIP response, simulations were run with varying chargeability m (0.5 to 0.999) and R_σ (0.005 to 0.99). The relaxation time was fixed to 10^{-3} s .

Figure 4.20 shows the simulated SIP response in the three measurement zones in response to different chargeability and conductivity ratio from 1 Hz to 100 MHz. The higher frequencies are also shown here in order to follow the change in peak frequency in all the simulations qualitatively. It can be seen that a chargeability of 0.995 and an R_σ equal to 0.9 times the background conductivity need to be specified for the calcite area to obtain a qualitatively similar response as in the experiments. The high chargeability is needed to obtain a similar magnitude for the SIP response. It should be noted that these chargeability and R_σ values are not necessarily close to the true value because of the limited spatial resolution of the simulation domain. In fact, the calcite area in the simulation domain consists of calcite precipitation and porous medium in the actual experiments.

A key finding of these simulation results was that the peak frequency can be different even if the complex electrical conductivity of the calcite precipitation is the same in all three measurement zones. In particular, this occurred when both m and R_σ values were high. This very likely explains why differences in peak frequency were observed between the three measurement zones. Also, it was found that multiple peaks in the σ'' can occur in the middle and downstream zones with high m and R_σ values even though the specified complex electrical conductivity for calcite only considered a single peak frequency. However, only the lower peak frequencies were in the frequency range used in the experiments. The higher peak frequencies consistently increase with increasing chargeability. This was expected from the Cole-Cole equation. This suggests that the lower peak frequencies cannot be attributed to the equation form of the Cole-Cole model when two peaks in σ'' are present. Another characteristic of the simulation result is that σ'' in the middle zone was larger than that of the other zones, which is consistent with the experimental results.

A second simulation scenario that was considered is presented in Figure 4.19b. It represents a relatively early time where the calcite precipitation front was not completely continuous. In this case, a small

4. Millifluidic experiments

fraction (33%) of the calcite precipitation was replaced by solution. With this discontinuous precipitation front, the simulated σ'' decreased substantially even though the area of calcite precipitation did not change much (Figure 4.21b). This clearly suggests that σ'' is sensitive to the continuity of the precipitation front. The small σ'' before 16 h in the experiments can thus be partly attributed to the discontinuity of the calcite wall.

In a third and final simulation scenario (Figure 4.19c), it was explored how a heterogeneous distribution of the complex electrical conductivity of calcite precipitation would influence the SIP response. Since the experimental results suggested that calcite precipitation was faster and more abundant near the electrodes than far from the electrodes (Figure 4.7), the chargeability was set higher near the electrodes (0.995) than far from the electrodes (0.4). Here, the experimental conditions after 16 h are considered again. In this case, the simulated σ'' partly showed negative values for the upstream measurement zone (Figure 4.21c). Thus, heterogeneous calcite properties likely explain the observed negative σ'' values obtained in the upstream measurement zone.

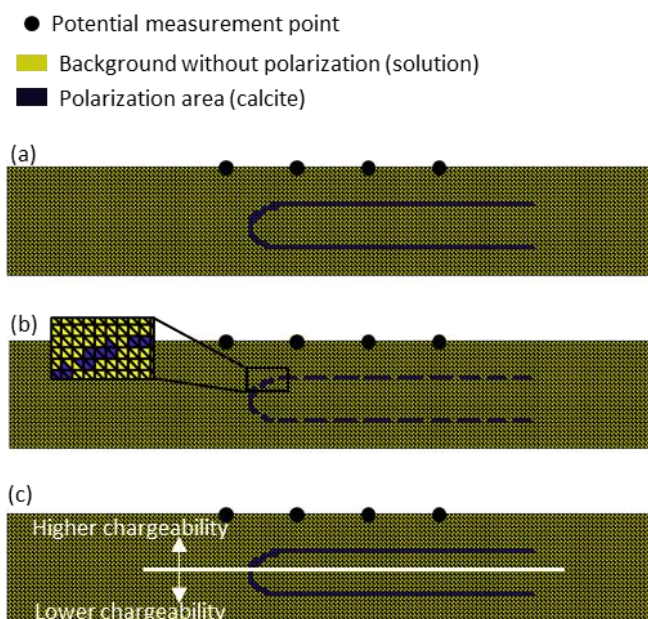


Figure 4.19. Simulation domains for three different scenarios: (a) continuous calcite precipitation front, (b) discontinuous calcite precipitation front, and (c) spatially variable complex electrical conductivity of calcite. The yellow colour represents the background and the blue colour represents the distribution of calcite precipitation.

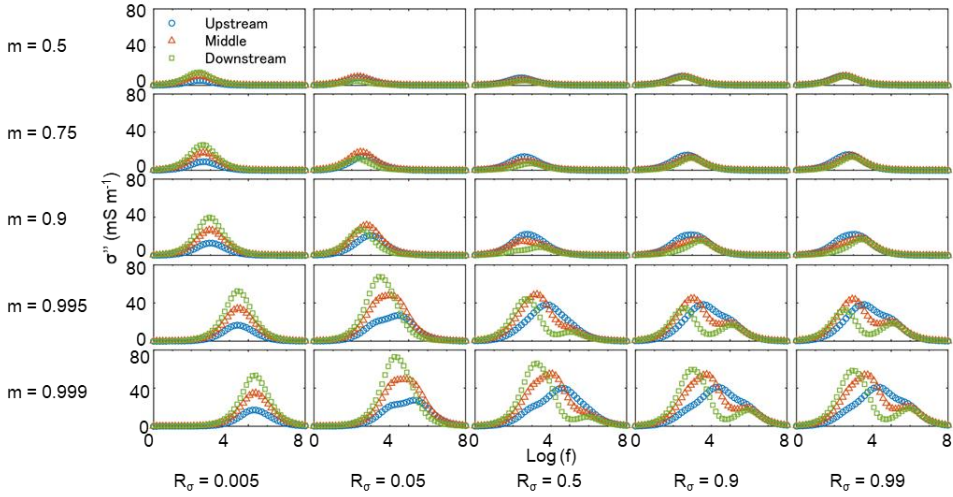


Figure 4.20. The simulated SIP responses in different measurement zones depending on chargeability and R_σ value.

To better understand the origin of the different peak frequencies, the normalized imaginary part of the electrical potential fields is shown in Figure 4.22 for two different sets of Cole-Cole parameters for the calcite zone. In a first simulation with $R_\sigma = 0.9$ and $m = 0.995$, the peak frequency differed between the measurement zones. In a second simulation with $R_\sigma = 0.005$ and $m = 0.995$, the peak frequency was identical for all three measurement zones. The key to interpreting these two simulations is to analyse the imaginary potential across the calcite wall. In the case of a R_σ of 0.9 (Figure 4.22a), there was a strong contrast for low frequencies (for example at 193 Hz), but this contrast was less strong at high frequencies (for example at 51 kHz). In this case, the semi-ellipsoidal shape of the calcite precipitation acted as a resistor for low frequencies because of the low electrical conductivity. In the high frequency range, calcite did not act as a resistor because it was more conductive. In contrast, for $R_\sigma = 0.005$ (Figure 4.22b), the contrast did not disappear for the higher frequencies because the calcite was assumed to have a low conductivity throughout the entire frequency range. From this comparison, it becomes clear that the relaxation of the imaginary potential across the calcite wall was key to understand different peak frequencies for the different measurement zones and that the shape of the calcite precipitation front resulted in different peak frequencies in different measurement zones. In the second scenario with discontinuous calcite precipitation, the imaginary potential differences across the calcite wall was much smaller than in the case with a continuous calcite wall (Figure 4.22c). This suggests that the contrast of the imaginary potential determines SIP response in measured frequency range. In the third scenario with heterogeneous calcite properties, it can be seen that the normalized imaginary potential was highest near the middle potential electrodes (Figure 4.22d). If the potential is measured on the left and right side of this local maximum, one measurement will show a positive imaginary potential and the other

4. Millifluidic experiments

measurement will show negative imaginary potential given that the sign of the potential depends on measurement direction. Thus, the negative σ'' values were introduced because of the local maximum in the imaginary potential associated with the heterogeneous distribution and properties of the calcite precipitation.

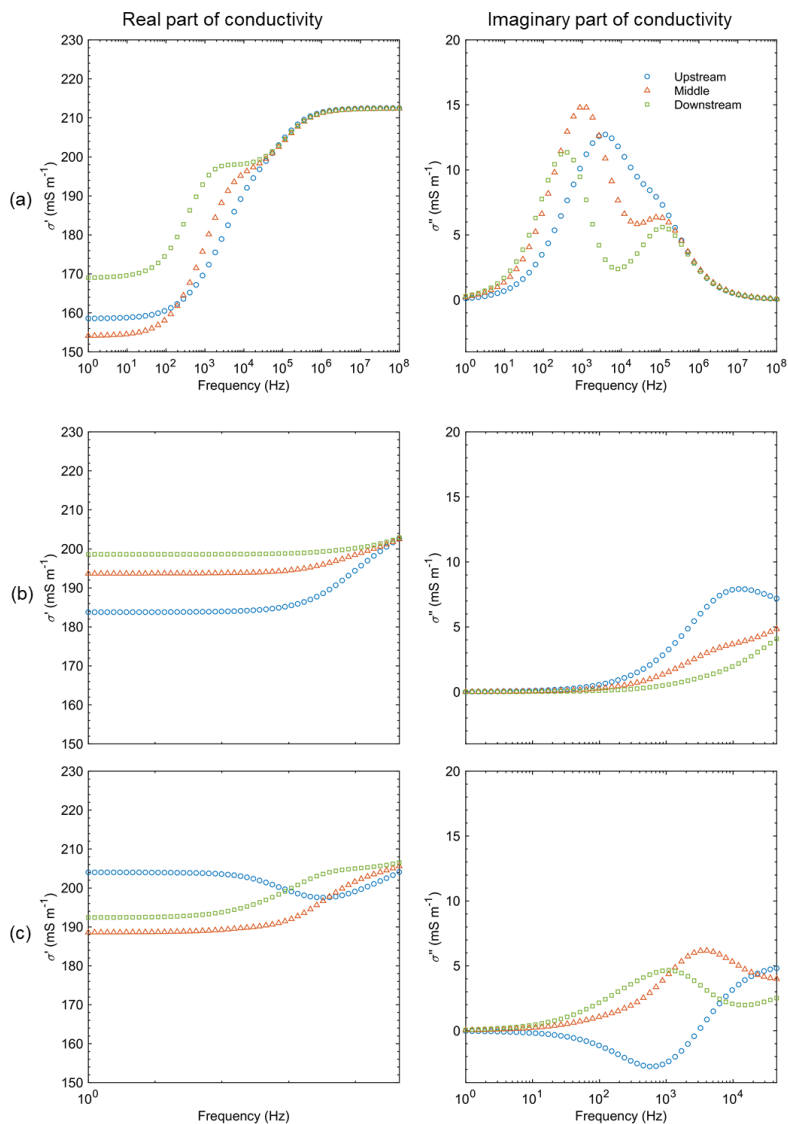


Figure 4.21. Simulated SIP response for different measurement zones for the three simulation scenarios shown in Figure 4.19: (a) continuous calcite precipitation front, (b) discontinuous calcite precipitation front, and (c) spatially variable complex electrical conductivity of calcite.

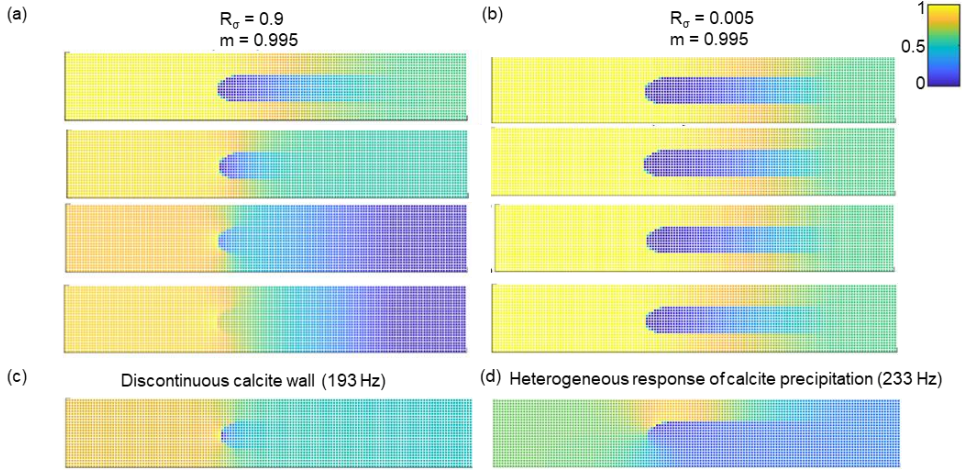


Figure 4.22. The normalized imaginary part of the potential field for different simulation scenarios: (a) continuous precipitation front with $m = 0.995$ and $R_\sigma = 0.9$ and (b) continuous precipitation front with $m = 0.995$ and $R_\sigma = 0.005$ (c) discontinuous precipitation front at 193 Hz, and (d) heterogeneous complex electrical properties of calcite at 233 Hz.

4.9. Discussion

The experimental results showed that the calcite precipitation process and the associated SIP response can be best understood by separating the experiment into two different periods. Before 20 h, a calcite precipitation front was established at the pore scale along the streamlines of Rankine half body flow and the associated σ'' was small. The simulation results showed that the low σ'' can at least partly be explained by the presence of a discontinuous precipitation front. In a similar manner, the result presented in Chapter 3 may be explained. As in this chapter, σ'' did not increase in the first several days of precipitation in the packed sand column. This highlights the need to consider the location and continuity of mixing when interpreting field and laboratory SIP measurements during precipitation processes (and reactive transport processes in general). It is important to realize that this continuity of precipitation is determined at the pore scale, and thus may be difficult to obtain beyond the experimental set-up used in this chapter.

After 20 hours, the observed σ'' strongly increased. The experimental observations suggest that this may be related to small increases in the height of the calcite precipitation. Peak frequencies were found to vary for different measurement zones, but this could not be attributed to differences in the size of the calcite crystals nor the variation in solute concentration. Using electrical field simulations, it was shown that this can potentially be explained by the shape of the precipitation front in combination with the electrical properties of calcite. For the given shape of the calcite precipitation, it was possible to obtain

4. Millifluidic experiments

different peak frequencies for the three measurement zones even when the properties of the calcite were assumed to be homogeneous. The simulations also showed that the observed negative σ'' values can be explained by a spatially variable complex electrical conductivity of calcite precipitation. In many laboratory SIP studies, negative σ'' values have been taken as a sign of poor measurement quality. This is certainly true when the investigated volume can safely be assumed to be homogeneous (e.g. a saturated sandstone sample). However, in the case of strong heterogeneity in the electrical properties a negative σ'' can easily be obtained. Considering that most biochemical reactions are heterogeneously distributed in space, negative σ'' values should thus not immediately be discarded as measurement errors when SIP is used to investigate reactive transport problems. The simulations also suggested that the peak frequency in the three measurement zones had smaller peak frequencies than expected from the Cole-Cole model. This suggests that heterogeneity possibly enables detecting material with higher peak frequency than the measurable range depending on its distribution in the measurement zone.

Leroy et al. (2017) suggested that polarization of calcite precipitation could be explained by the grain polarization model (Chapter 2). This model considers three components, (i.e. water, electric double layer of calcite and the body of calcite) that are all affected by calcite precipitation. In particular, the pore water conductivity and solute concentration increase when the precipitation front is being built due to the reduced mixing and the associated reduced reaction rates as discussed in the interpretation of the initial phase of the experiment. In response, higher concentration of solutes, specifically Ca^{2+} and CO_3^{2-} ions, lead to a larger amount of adsorbed ions on the calcite surface (Al Mahrouqi et al., 2017). This larger amount of positively/negatively charged adsorbed ions results in more electric charge in the Stern layer of the electric double layer. Also, the increase in the volume of calcite leads to a decrease in bulk conductivity. Such changes in the amount of calcite and the pore water conductivity are expected to change σ' both at 1 Hz and 10 kHz in this model. It should be noted that this expected change is independent of the size of the calcite precipitates. In the experimental results, the σ' was almost constant at 10 kHz (Figure 4.15d). In the context of the grain polarization model, this suggests that the change in solute concentration and the increase in the amount of calcite were small. In contrast, the observed σ' at 1 Hz consistently decreased after 20 h (Figure 4.15c). Because the difference in σ' at 1 Hz and 10 kHz is closely related to the chargeability, the experimental results indicate an increase in chargeability with time. The chargeability may increase due to an increase in surface area, changes in crystal size or increasing solute concentration. It seems unlikely that the observed increase in chargeability can be explained by an increase in surface area because changes in the volume of calcite precipitation were quite small after 20 h (Figure 4.7). In addition, the crystal size did not change (Figure 4.4). Therefore, the chargeability should have been extremely sensitive to the solute concentration if the experimental results need to be explained with the grain polarization model. The experimental results with well-defined solute concentrations at two different times during the precipitation process suggested that the solute concentration is at least not the only factor that controls the SIP response (Figure 4.18). Thus,

the possibility of extreme sensitivity to solute concentration cannot be fully excluded. However, there is another way to explain the experimental results that does not require the invocation of such extreme sensitivity.

An alternative explanation for the strong SIP response is that it is associated with Maxwell-Wagner polarization associated with the thin calcite precipitation front. For simplicity, pure calcite without an electric double layer is considered here. To verify the potential importance of this process, consider a simple conceptual model (Figure 4.23a) composed of a calcite wall (length 10^{-3} mm, width 1 mm, height 0.99-0.9999 mm), a mixing zone above the calcite wall (length 10^{-3} mm, width 1 mm, height 0.01-0.0001 mm), and the surrounding water (length 5 mm, width 1 mm, height 1 mm). The width of the calcite wall was based on the actual dimensions of the calcite precipitation front obtained from images acquired after the experiment (Figure 4.5). The water in the mixing zone is assumed to be in equilibrium with calcite (0.375 S m^{-1}), whereas the pore water conductivity was taken as the average of the injected solutions (0.50 S m^{-1}). The relative permittivity of calcite was assumed to be 12 (Arcone & Boitnott, 2010). This conceptual model can be simplified to an electric circuit model as shown in Figure 4.23b, in which the electrical properties (R_1 , R_2 , C) can be calculated based on the dimensions and parameters provided above.

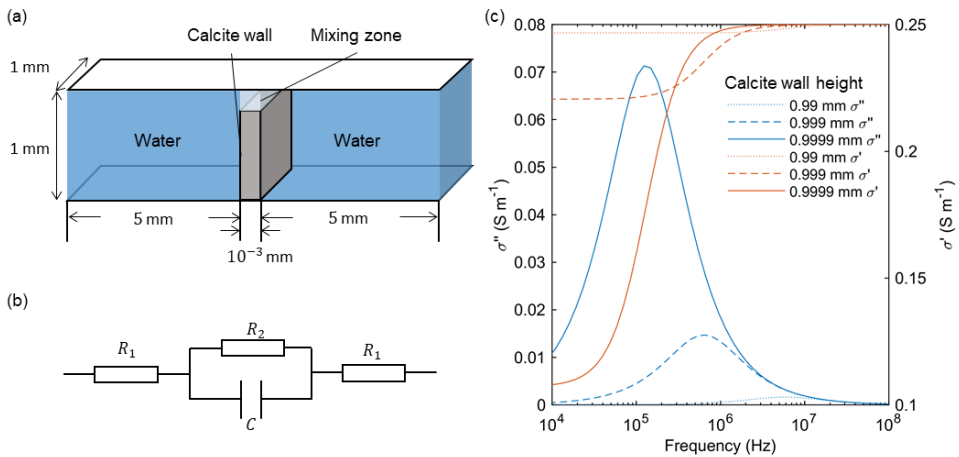


Figure 4.23. (a) Conceptual model to explain Maxwell-Wagner polarization associated with the calcite precipitation front, (b) equivalent electric circuit of the conceptual model, and (c) simulated σ' and σ'' as a function of the height of the calcite precipitation front.

4. Millifluidic experiments

Simulation results based on this simple conceptual model suggest that an increase in calcite wall height will lead to a lower peak frequency, an increase in the peak σ'' , a constant σ' at high frequency and a decrease in σ' at low frequency (Figure 4.23c). The peak frequency with the highest calcite wall was about 100 kHz, which is the same as the peak frequency of the Cole-Cole model used in the simulations shown in Figure 4.21a. This simple model thus captures some of the key characteristics of the experimental results. It is important to note that this conceptual model is highly sensitive to the size of the gap between the top of the calcite wall and the top plate, especially when the gap is nearly closed (high R_2). This may explain why small increases in the height of the calcite precipitation resulted in large increases in chargeability after 20 h in the experiment. Also, the small σ'' before 20 h can be partly attributed to the large gap between the top plate and the calcite wall, in addition to the discontinuity of the wall as explained earlier. However, the observed constant peak frequency (Figure 4.15a) could not be explained by only changing the height of the calcite wall in the model. Furthermore, an extremely small gap (1 μm) was required to obtain the expected peak frequency. Therefore, the conceptual model does not fully explain all experimental results. Clearly, it is possible that more processes play a role, for example the surface complexation of calcite. Adding these factors to the simple conceptual model may help to explain the change in peak frequency, as well as other previous experimental results obtained in column experiments (Saneiyani et al., 2018; Wu et al., 2010; Zhang et al., 2012, Chapter 3).

4.10. Conclusions

In this chapter, the SIP response was measured during spatially and temporally dynamic calcite precipitation processes using a newly developed millifluidic set-up. The millifluidic set-up enabled visual observation of calcite precipitation in porous media and numerical simulations were used to improve understanding of the obtained SIP responses. At the beginning of the experiment, the observed σ'' was low even though most of the precipitation occurred in this period. This apparently contradicting behaviour of σ'' and the volume of calcite precipitation was attributed to the discontinuity of the calcite precipitation front and the large gap between the top plate and the calcite wall. After 20 h, the observed σ'' started to increase. This increase was probably affected by the filling of the gap between the top plate and the calcite wall, and not only due to changes in solute concentration. The peak frequency varied depending on the considered measurement zone, although the observed size of the crystals was almost the same for all three measurement zones. Numerical simulations showed that the source of this difference in peak frequency was due to the shape of the calcite precipitation front within the measurement zone. In addition, these simulations showed that measured negative σ'' values can be explained by the heterogeneous development of the electrical properties of the calcite precipitates. Based on the experimental observations and numerical simulation results, a simple electric circuit model was derived that explains key characteristics of the SIP response observed in this chapter. The proposed model to explain the observed SIP response suggests that Maxwell-Wagner polarization is dominant in

the experiments. This polarization mechanism was able to partly explain the observed SIP response by focusing on the capacitive leakage associated with the gap between the top plate and the top of calcite wall. The experimental results agreed less with the previously suggested grain polarization model for calcite. This new and detailed understanding of the SIP response during the calcite precipitation process can be used to design new experiments to further improve understanding or to interpret field data. In future work, the quantitative dataset can be the base for numerical and theoretical studies for microscopic understanding of the source of SIP response of calcite. Further opportunities arise regarding the application of SIP for field studies of calcite precipitation and for laboratory studies investigating calcite nucleation and precipitation processes.

4. *Millifluidic experiments*

Chapter 5

Enhancement of mixing-induced reactions at stagnation points in pore scale flow fields

In Chapter 4, the millifluidic experiment highlighted that the SIP response of calcite precipitation in porous media largely depends on pore scale chemical reaction processes. In this chapter, the pore scale reaction process will be investigated in more detail to support the understanding of the SIP response of calcite precipitation in porous media.

This chapter will present the first experimental study of mixing and reaction at stagnation points in porous media. Changes in chemical reaction dynamics will be studied according to flow rate and reaction rate, which are represented by the Péclet number (Pe) and the Damköhler number (Da). First, scaling laws at stagnation points will be derived theoretically as a function of Pe and Da by combining the reactive lamella approach (Bandopadhyay et al., 2017; Ranz, 1979), the theoretical framework of reaction-diffusion fronts (Larralde et al., 1992), and the stretching dynamics at stagnation points (Villermaux, 2019). Next, reaction dynamics will be investigated experimentally in 2D flow fields of a Hele-Shaw cell with and without cylindrical columns (referred to as 2D porous medium and Hele-Shaw cell in the following). This will be achieved by imposing a background flow using fluid injection from one side and a point source of reactant in the middle of the flow (Figure 5.1a). This results in a flow field with one stagnation point upstream of the point source, which is generally referred to as Rankine-half body flow (White, 1998). For the porous medium, randomly positioned cylinders are considered with an aspect ratio between the height and the pore size, which is sufficient to ensure two-dimensional flow. The experiments will be performed both with conservative and reactive tracers producing chemiluminescence in order to quantify the reaction rate in the front (de Anna et al. 2014). Finally, pore scale flow and stretching will be investigated using numerical simulations.

5. Mixing-induced reactions at stagnation points

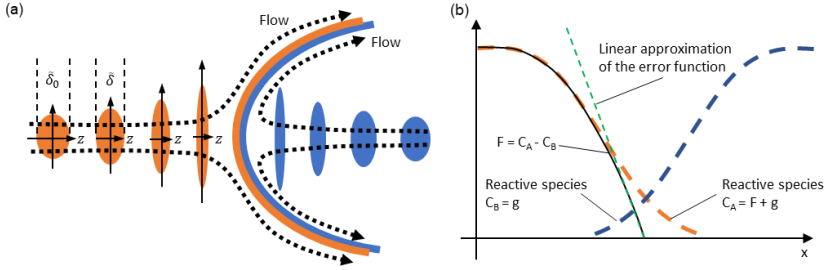


Figure 5.1. Schematic illustration showing (a) deformation of small fluid elements near the stagnation point where blue and orange represent different solutes (b) the concentration profile of species A (orange) and B (blue) near the stagnation point. The black line represents the conservative component F . The green line represents the linear approximation of the error function (F) near the stagnation point.

5.1. Theory

In this section, the lamellar theory of mixing is used (Le Borgne et al., 2015; Villiermaux, 2019) to derive approximate analytical solutions for coupled mixing and reaction at a stagnation point. Small incompressible fluid elements, called lamella, deform due to elongation and compression in the flow field. The compression rate γ is defined as:

$$\gamma = -\frac{1}{\tilde{\delta}} \frac{d\tilde{\delta}}{dt} \quad (5.1)$$

where $\tilde{\delta}$ is the width of lamella in the direction of compression. Stagnation points are characterized by a locally constant compression rate γ (Villiermaux, 2019), such that the lamella width decays exponentially close to the stagnation point,

$$\tilde{\delta} = \tilde{\delta}_0 e^{-\gamma t} \quad (5.2)$$

where $\tilde{\delta}_0$ is the initial lamella size. Exponential compression is a key characteristic of stagnation points that drives mixing and reaction properties (Hidalgo et al., 2015).

The width of a lamella of solute is governed by compression and diffusion. Solute diffusion acts to broaden the size of the lamella, whereas fluid compression acts to decrease the size (Le Borgne et al., 2015; Villiermaux, 2019). At long times, the diffusive expansion and compression rate balance as:

$$\frac{D}{\tilde{\delta}^2} \sim \gamma \quad (5.3)$$

where D is the diffusion coefficient. Inserting equation 5.2 into equation 5.3 allows to quantify the mixing time, which is the time required to balance the broadening due to diffusion and constant

compression. The lamella size $\tilde{\delta}$ after the mixing time is called Batchelor scale s_b (Batchelor et al., 1959):

$$s_b = \sqrt{\frac{D}{\gamma}} \quad (5.4)$$

In the case of laminar flow conditions, $\gamma \sim \nabla v \sim \bar{v}/L$, where ∇v is a characteristic velocity gradient at the stagnation point, L is the characteristic length of this gradient and \bar{v} is the average velocity. Hence,

$$s_b \sim \sqrt{\frac{D}{v}} \sim Pe^{-1/2} \quad (5.5)$$

where $Pe = DL/v$ is the Péclet number. This implies that the characteristic mixing width tends to be constant at stagnation points, which implies that concentration gradients, and therefore mixing rates are constant.

The lamella framework assumes that concentration gradients along the direction of elongation are negligible and that concentration distributions are thus mainly driven by mass transfer in the direction of compression. In a Lagrangian framework aligned with the directions of elongation and compression, the change in the concentration within the lamella can thus be quantified by the compression diffusion equation (Ranz, 1979):

$$\frac{\partial C_A}{\partial t} + \gamma x \frac{\partial C_A}{\partial x} = D \frac{\partial^2 C_A}{\partial x^2} \quad (5.6)$$

where x is the coordinate along the compression direction. In the presence of reactions, the above equation can be written as:

$$\frac{\partial C_A}{\partial t} + \gamma x \frac{\partial C_A}{\partial x} = D \frac{\partial^2 C_A}{\partial x^2} - k C_A C_B \quad (5.7)$$

where C_A and C_B are concentration of reactants, normalized by the initial concentration C_0 , k is the reaction constant for dimensionless concentrations $k = \tilde{k}C_0$ with \tilde{k} the rate constant in units of inverse of concentration and time. Nondimensional variables are defined as follows (Ranz, 1979):

$$\theta = \int_0^t d\tau D / \tilde{\delta}(\tau)^2, z = x / \tilde{\delta} \quad (5.8)$$

where θ is called the warped time and z represents the distance relative to the size of lamella. For exponential compression (equation 5.2), this results in:

$$\theta = \frac{D}{\gamma \tilde{\delta}_0^2} \frac{1}{2} (e^{2\gamma t} - 1) \quad (5.9)$$

In these non-dimensional variables, equation 5.7 reduces to a diffusion-reaction equation (Bandopadhyay et al., 2017):

5. Mixing-induced reactions at stagnation points

$$\frac{\partial C_A}{\partial \theta} = \frac{\partial^2 C_A}{\partial z^2} - \frac{k C_A C_B \tilde{\delta}^2}{D} \quad (5.10)$$

which can be written as:

$$\frac{\partial C_A}{\partial \theta} = \frac{\partial^2 C_A}{\partial z^2} - Da C_A C_B \delta^2 \quad (5.11)$$

with the Damköhler number Da defined as:

$$Da = \frac{k \tilde{\delta}_0^2}{D} \quad (5.12)$$

and $\delta = \tilde{\delta}/\tilde{\delta}_0$.

5.1.1. Derivations for $Da > 1$ regime

For $Da > 1$, the interpenetration of the two reactive solutes is small as the reaction is faster than diffusion. Therefore, in the domain where the concentration of substance A is larger, B can be considered as a small fluctuation. Following Larralde et al. (1992) and Bandopadhyay et al. (2017), the concentration of C_A and C_B are thus written in terms of a conservative component $F = C_B - C_A$ and a perturbation g , such that $C_A = F + g$ and $C_B = g$ (Figure 5.1b). F follows the conservative equation:

$$\frac{\partial F}{\partial \theta} = \frac{\partial^2 F}{\partial z^2} \quad (5.13)$$

which leads to the solution:

$$F = \text{erf}\left(\frac{z}{\sqrt{4\theta}}\right) \quad (5.14)$$

Inserting $C_A = F + g$ and $C_B = g$ into equation 5.8, it is obtained that:

$$\frac{\partial g}{\partial \theta} = \frac{\partial^2 g}{\partial z^2} - Da g \left(\text{erf}\left(\frac{z}{\sqrt{4\theta}}\right) + g \right) \delta^2 \quad (5.15)$$

Following Larralde et al. (1992), the term proportional to g^2 is neglected and the error function in the mixing zone is linearized (Figure 5.1b). This leads to the approximation:

$$\frac{\partial g}{\partial \theta} \approx \frac{\partial^2 g}{\partial z^2} - Da g \frac{z}{\sqrt{\pi\theta}} \delta^2 \quad (5.16)$$

For the stationary conditions that develop at the stagnation point, this equation becomes:

$$\frac{\partial^2 g}{\partial z^2} - Da g \frac{z}{\sqrt{\pi\theta}} \delta^2 = 0 \quad (5.17)$$

Using dimensional spatial coordinates, $x = \tilde{\delta}z$, this leads to:

$$\frac{\partial^2 g}{\partial x^2} - Da g \frac{x}{\tilde{\delta}_0^3 \delta \sqrt{\pi \theta}} = 0 \quad (5.18)$$

This is an Airy differential equation, whose solution is (Bandopadhyay et al., 2017):

$$g \sim f(\theta) Ai\left(\frac{\lambda z}{\theta^{1/6}}\right) \sim \frac{\tilde{\delta}_0^{-2} \delta^{-2/3} \theta^{-1/3}}{\lambda} Ai\left(\frac{\lambda x}{\tilde{\delta}_0 \delta^{1/3} \theta^{1/6}}\right) \quad (5.19)$$

where:

$$\lambda = \left(\frac{Da}{\sqrt{\pi}}\right)^{1/3} \quad (5.20)$$

where $Ai(x)$ is the Airy function. The reaction rate $R(x, \theta)$ can be calculated by inserting equation 5.19 into the second term of equation 5.17:

$$R(x, \theta) \approx \frac{\tilde{\delta}_0^{-4} \delta^{-4/3} \theta^{-2/3} Da}{\lambda^2} \left(\frac{\lambda x}{\tilde{\delta}_0 \delta^{1/3} \theta^{1/6}}\right) Ai\left(\frac{\lambda x}{\tilde{\delta}_0 \delta^{1/3} \theta^{1/6}}\right) \quad (5.21)$$

Hence, the reaction rates may be written as:

$$R(x) \approx R_{max} f\left(\frac{x}{s_r}\right) \quad (5.22)$$

with $R_{max} \sim \tilde{\delta}_0^{-4} \delta^{-4/3} \theta^{-2/3} Da / \lambda^2$ and $s_r \sim \tilde{\delta}_0 \delta^{1/3} \theta^{1/6} / \lambda$.

For large times $\delta = e^{-\gamma t}$ and $\theta = \frac{D}{\gamma \tilde{\delta}_0^2} e^{2\gamma t}$, it can be obtained that:

$$s_r \sim Da^{-1/3} P e^{-1/6} \quad (5.23)$$

and:

$$R_{max} \sim Da^{1/3} P e^{2/3} \quad (5.24)$$

The integral of the reaction rate over the length (the reaction intensity I_R) should thus scale as:

$$I_R \sim s_R R_{max} \sim P e^{1/2} \quad (5.25)$$

5.1.2. Derivations for $Da < 1$ regime

When $Da < 1$, the interpenetration of the two reactive solutes A and B is large and the assumptions made in the previous derivations do not hold. Since diffusion dominates over reaction for $Da < 1$, the concentration profiles for C_A and C_B are expected to be close to the conservative profiles, which are solutions of equation 5.5. This equation may be solved using the same change of variable as in equations 5.13 and 5.14, to yield the following expressions for C_A :

$$C_A = \frac{1}{2} \left(1 + erf\left(\frac{z}{\sqrt{4\theta}}\right) \right) \quad (5.26)$$

and for C_B :

5. Mixing-induced reactions at stagnation points

$$C_B = \frac{1}{2} \left(1 - \operatorname{erf} \left(\frac{z}{\sqrt{4\theta}} \right) \right) \quad (5.27)$$

The reaction rate can be estimated using,

$$R = Da C_A C_B \quad (5.28)$$

After inserting equations 5.26 and 5.27, this results in

$$R = Da \left(1 - \operatorname{erf} \left(\frac{z}{\sqrt{4\theta}} \right) \right)^2 \quad (5.29)$$

In dimensional coordinates, this gives,

$$R = Da \left(1 - \operatorname{erf} \left(\frac{x/\tilde{\delta}_0 e^{\gamma t}}{\sqrt{4 \frac{D}{\gamma \tilde{\delta}_0^2} \frac{1}{2} (e^{2\gamma t} - 1)}} \right) \right)^2 \quad (5.30)$$

At long times, it can be obtained that

$$R = Da \left(1 - \operatorname{erf} \left(\frac{x}{\sqrt{2} s_B} \right) \right)^2 \quad (5.31)$$

Hence, for $Da < 1$, the reaction width and maximum reaction rate are expected to scale as,

$$s_R \sim s_B \sim P e^{-1/2} \quad (5.32)$$

and:

$$R_{max} \sim Da \quad (5.33)$$

5.2. Experimental setup to investigate reaction dynamics

The millifluidic set-up developed in Chapter 4 was used to characterize mixing and reaction dynamics experimentally and to investigate the impact of porous media flow on these reactive dynamics. The overall setup is shown in Figure 5.2. Importantly, the pore throats of the 2D porous medium (median: 0.36 mm) were smaller than the height of the cylinders (1 mm). This large aspect ratio was chosen to ensure that the flow field may be considered as 2D because Taylor-Aris dispersion is expected to be dominant in horizontal direction. Using fluid injection ports at the side and in the middle of the porous medium, a point source in a uniform background flow was created. This configuration resulted in a Rankine half-body flow with one stagnation point upstream of the point source (Figure 5.2c). By replacing the porous medium with a flat plate made of PDMS (length: 150 mm, width: 50 mm, height: 10.4 mm), a Hele-Shaw cell configuration with a gap height of 0.6 mm was obtained.

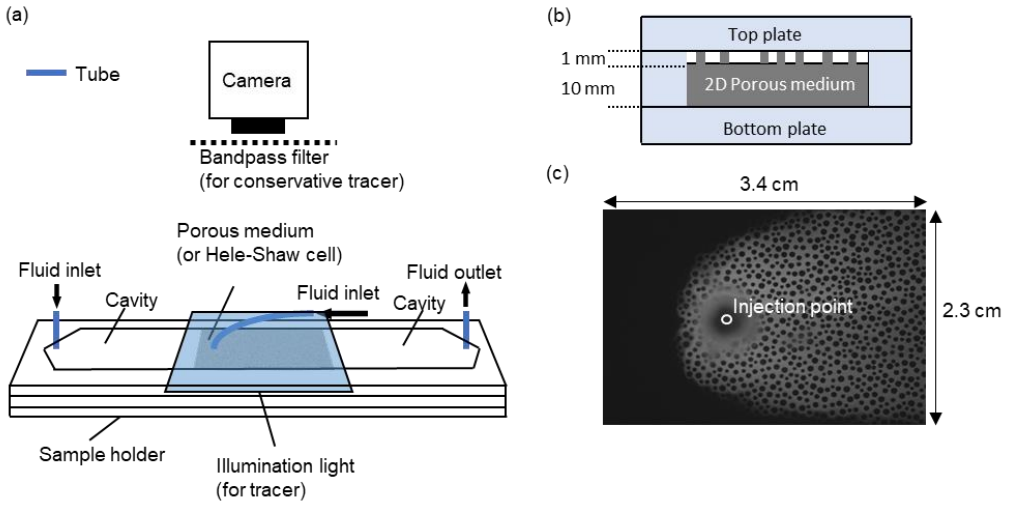


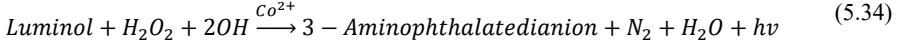
Figure 5.2. (a) Illustration of the overall experimental setup, (b) Cross-section of the millifluidic set-up, (c) Example of a photo of the porous medium taken during the conservative tracer experiment.

A mirrorless digital camera (14-bit, SONY alpha7s, SONY, Tokyo, Japan) with a macro lens (MACRO GOSS F2.8/90, SONY, Tokyo, Japan) was placed above the millifluidic set-up. The height of the camera was set to 12 cm for the conservative tracer experiments with porous medium, 13.5 cm for the reactive tracer experiments, or 28 cm for the conservative tracer experiments in the Hele-Shaw cell configuration. This resulted in an image resolution of 0.008 mm, 0.010 mm and 0.023 mm per pixel, respectively. These resolutions were selected to ensure that the mixing front can be fully resolved in each case. Images were taken after the mixing interface stabilized for each flow rate. The image intensity was normalized by the bit depth of the camera ($2^{14}-1$) for the reactive tracer experiments, and by the maximum pixel intensity for the conservative tracer experiments.

For the conservative tracer experiments, fluoresceine sodium salt solution (50 mg L^{-1}) and deionized water were injected from the side and from the middle with the same flow rate. A blue coloured light source (LFL-180BL2, CCS inc., Kyoto, Japan) illuminated the millifluidic set-up from below to excite the fluoresceine sodium salt tracer. A bandpass filter (Narrow Green Bandpass Filter, Midwest Optical Systems, Palatine, LI, USA) was attached to the lens to select the wave length emitted by the fluoresceine. For the reactive transport experiments, chemiluminescence was used to investigate the reaction rate in the porous medium and the Hele-Shaw cell configuration. To induce chemiluminescence, two different solutions were injected. The first solution was a mixture of 1 mM Luminol, 7 mM NaOH and 0.01 mM CoCl_2 , and the second solution was a mixture of 0.5 mM H_2O_2 and 3.9 mM NaCl. The luminol and H_2O_2 solutions were injected through the side and middle injection ports, respectively. The

5. Mixing-induced reactions at stagnation points

chemiluminescence reaction involves a catalytic reaction of H_2O_2 with Co^{2+} followed by an oxidation reaction of Luminol with OH and O_2^- radicals (Uchida et al., 2004). This chain reaction can be written as:



Luminol is thus oxidized to 3-Aminophthalatedianion with an emission of blue light ($\lambda = 420 - 460 \text{ nm}$). The reaction rate is proportional to the blue light intensity in the image. It has been shown that the reacting interface of this chemiluminescence reaction can be simulated with the bimolecular reaction term $kC_A C_B$ (Matsumoto & Matsuo, 2015). Because the emitted light intensity of the chemiluminescence was weak, 5 to 10 images were taken after stabilizing the reaction for each flow rate. By averaging the images for each flow rate, the background noise was reduced.

Different flow rates were investigated with a stepwise increase evenly distributed in log space. For conservative tracer experiments in the Hele-Shaw cell configuration, the investigated flow rates were 0.14, 0.28, 0.56, 1.11 and 2.22 $\text{mm}^3 \text{ s}^{-1}$. For all other experiments, the investigated flow rates were 0.14, 0.20, 0.28, 0.40, 0.56, 0.79, 1.11, 1.57 and 2.22 $\text{mm}^3 \text{ s}^{-1}$. The Péclet number was calculated as $Pe = vL/D$, where v is the average pore velocity, L is a characteristic length and $D = 10^{-9} \text{ m}^2 \text{ s}^{-1}$ is the molecular diffusion coefficient. The characteristic length was taken as the median pore throat size of the porous medium (0.363 mm). For the calculation of Pe in the Hele-Shaw cell configuration, the same characteristic length was used as in the porous medium in order to compare mixing and reaction in the two set ups for the same velocities. For a given flow rate, the pore velocity in the porous medium and the Hele-Shaw cell were approximately the same considering the porosity (0.59) and the relative height of the Hele-Shaw cell compared to the height of the porous medium (0.6). Using these assumptions, the Peclet numbers were $Pe = 1.7, 3.4, 6.8, 14$ and 27 for the conservative tracer experiments in the Hele-Shaw cell configuration. In all other cases, the Peclet numbers were $Pe = 1.7, 2.4, 3.4, 4.8, 6.8, 9.6, 14, 20$ and 27.

5.3. Numerical simulations

2D pore-scale simulations were performed to simulate flow and stretching statistics in the 2D porous medium used in the experiments. The simulation domain was defined to match the entire measurement area (100 mm by 50 mm) for the porous medium and the Hele-Shaw cell configuration. The flow field was simulated using a modified version of the Stokes equation implemented in the open source software OpenFOAM (<https://openfoam.org/>), which calculates the average velocity over the two plates (Lamb, 1906):

$$\nabla p = \mu \nabla^2 v - \frac{12\mu}{h^2} v \quad (5.35)$$

where p is pressure (N m^{-2}), μ is dynamic viscosity (N s m^{-2}), v is velocity (m s^{-1}) and h is channel height (m). A finite volume method with a square mesh size of $20 \mu\text{m}$ was used to solve this equation, which is small compared to the average pore throat ($360 \mu\text{m}$).

5.4. Results and discussion

5.4.1. Conservative mixing

To estimate the mixing front width from the conservative tracer experiments, an error function was fitted to the concentration profiles across the stagnation point (equation 5.26),

$$C = \frac{1}{2} \left(1 + \operatorname{erf} \left(\frac{x}{\sqrt{2}s_B} \right) \right) \quad (5.36)$$

where s_B is the Batchelor scale (equation 5.5). In addition, the concentration gradients were fitted with the derivative of equation 5.36,

$$\frac{dC}{dx} = \frac{1}{\sqrt{2}\pi s_B} \exp \left(-\frac{x^2}{2s_B^2} \right) \quad (5.37)$$

Examples of measured concentration profiles and fitted functions for different flow velocities are shown in Figure 5.3.

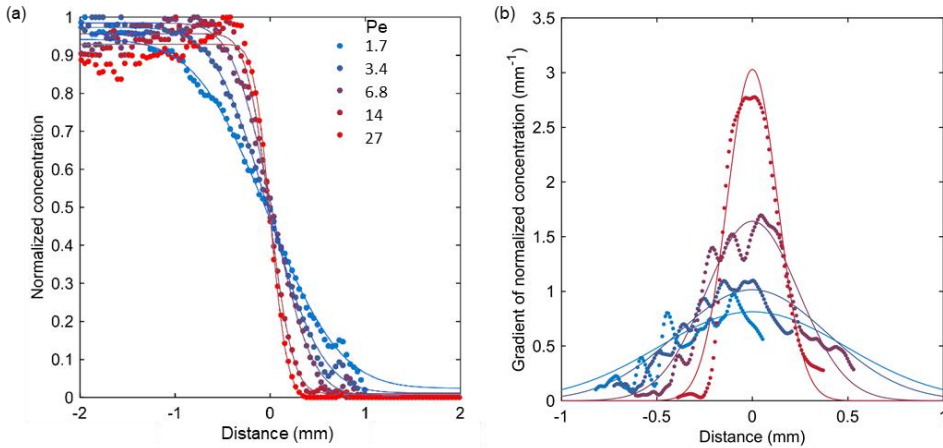


Figure 5.3. (a) Measured concentration profiles and fitted curves for conservative tracer experiments in the Hele-Shaw cell configuration and (b) measured concentration gradient profiles (dots) and fitted curves (lines) for conservative tracer experiments in the porous medium.

5. Mixing-induced reactions at stagnation points

The estimated mixing widths are shown in Figure 5.4 for the Hele-Shaw and porous medium experiments. For the experiments in the Hele-Shaw cell, the Batchelor scale is found to scale as $Pe^{-1/2}$ (Figure 5.4a), which is consistent with the theoretical expectations (equation 5.5). For the experiments in a porous medium, the results are more noisy due to the variability of the pore scale velocities and because of slight changes in the position of the front for the different flow rates. For the largest flow rate, there was an artifact related to the overly small size of the Batchelor scale because small fluctuations in the flow rate within the exposure time of the camera resulted in relatively large deviations of the width compared to the Batchelor scale. Thus, this data point was removed. After this, the mixing scale also approximately scaled as $Pe^{-1/2}$, as expected from the theoretical predictions (Figure 5.4a). The mixing width was smaller for the porous medium than for the Hele-Shaw cell in most cases, which suggests a larger compression rate in the porous medium. Assuming that the mixing scale was related to the compression rate following equation 5.4, the ratio α of the compression rate in the porous medium (γ_p) and the compression rate in the Hele-Shaw cell (γ_H) can be calculated,

$$\gamma_p = \alpha\gamma_H \quad (5.38)$$

Using equation 5.4, the Batchelor scale can be written as:

$$s_{b,p} = \alpha^{-1/2}s_{b,H} \quad (5.39)$$

The compression rate in the porous medium was larger in all cases (Figure 5.4). The maximum ratio was about 1.6.

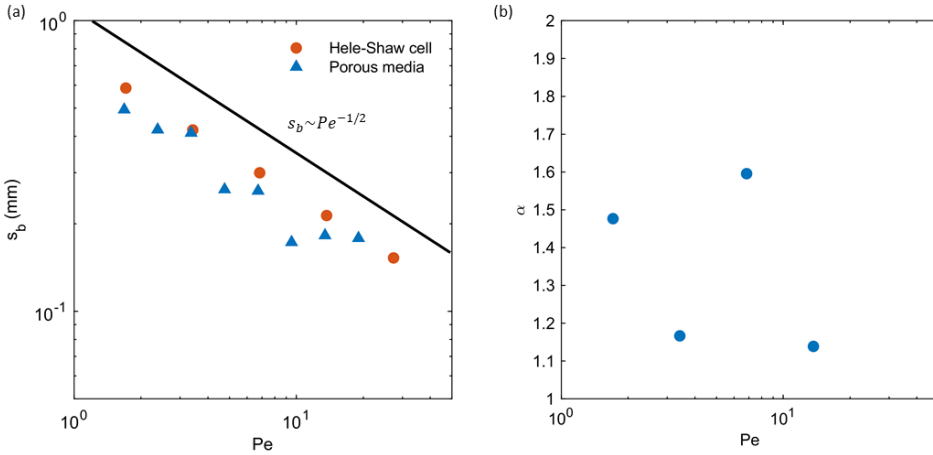


Figure 5.4. (a) Scaling of the conservative mixing width as a function of Pe for Hele-Shaw cell and porous medium experiments. (b) Calculated ratio of the compression rate in the porous medium compared to the Hele-Shaw cell based on the measured Batchelor scale.

5.4.2. Reactive mixing

To quantify the reaction width and maximum reaction rate at the stagnation point, the reaction intensity was measured along the line perpendicular to the mixing front (Figure 5.5). To reduce noise, the intensity was averaged over 1 pixel on each side of the line. Since the front was more regular and the intensity of the light was smaller for the Hele-Shaw cell, this averaging distance was increased to 30 pixels on each side of the line in this case. A Gaussian function was fitted to the light intensity across the front to estimate the width and maximum reaction rate (Figure 5.6). In addition, the image intensity was integrated over the measured line to estimate the total reaction rate at the stagnation point. In case of the porous medium, two stagnation points were analyzed (Figure 5.5b).

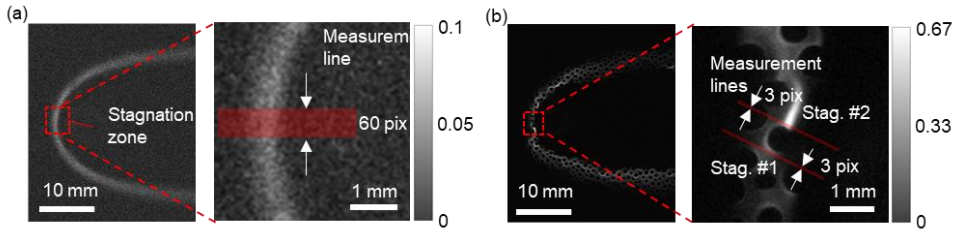


Figure 5.5. Examples of images around the stagnation point at the maximum Pe for reactive tracer experiments and the measured lines for analysis of the stagnation points in the (a) Hele-Shaw cell and (b) porous medium (both $Pe = 14$). The scale bars show the normalized reaction rate.

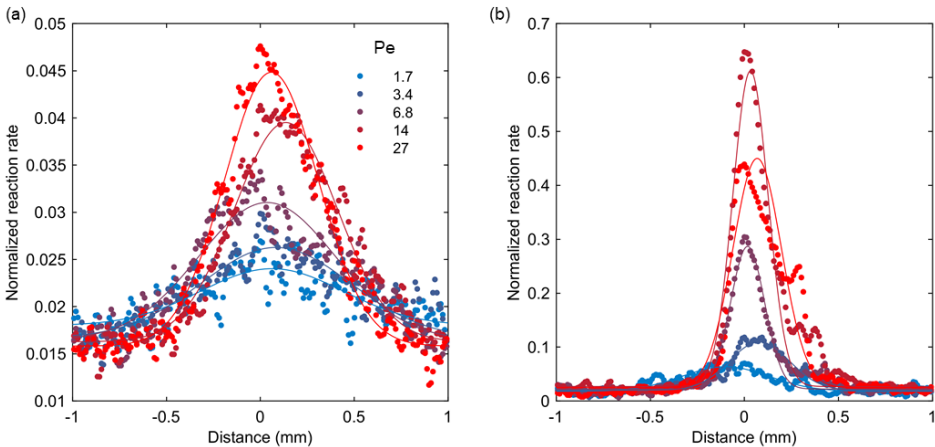


Figure 5.6. Reaction rate profiles across the stagnation points (dots) for different flow conditions in the (a) Hele-Shaw cell and (b) porous medium. Fitted Gaussian curves are shown as continuous lines.

5. Mixing-induced reactions at stagnation points

For the Hele-Shaw cell, the experimental results matched well with the theoretical scaling laws (Figure 5.7) for the reaction width (equation 5.23), the maximum reaction rate (equation 5.24) and the integrated reaction rate (equation 5.25). In the presence of a porous medium, the experimental results were more noisy because of the flow heterogeneity. Different behaviors were observed for the two stagnation points (Figure 5.5.b) because of the strong fluctuation of the compression in the pore space. However, the general tendencies were also compatible with the theoretical predictions for the porous medium experiments. As for the conservative case, the reaction width was significantly smaller in the porous medium compared to the Hele-Shaw cell (Figure 5.7a), resulting in larger gradients and enhanced reaction rates (Figure 5.7b,c).

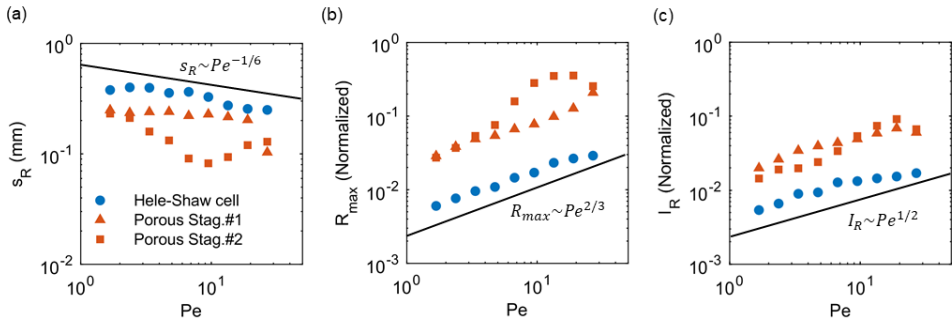


Figure 5.7. Scaling of the reaction front in the chemiluminescence experiments as a function of Pe . (a) Width of the reaction front, (b) maximum reaction rate normalized by the depth of the images (c) Reaction intensity normalized by the depth of the images.

As for the conservative tracer experiments, the ratio of the compression rates was estimated to explain the difference between the Hele-Shaw cell and porous medium experiments. Assuming that the reaction width, maximum reaction rate and integrated reaction follow equations 5.23, 5.24 and 5.25, it can be obtained that:

$$s_{R,p} = \alpha^{-1/6} s_{R,H} \quad (5.40)$$

for the reaction width,

$$R_{max,p} = \alpha^{2/3} R_{max,H} \quad (5.41)$$

for the maximum reaction rate, and

$$I_{R,p} = \alpha^{1/2} I_{R,H} \quad (5.42)$$

for the integrated intensity, where the subscripts p and H indicate the porous medium and the Hele-Shaw cell, respectively. The compression ratio α estimated from the maximum reaction rate and the reaction intensity were close and have a similar trend (Figure 5.8). The geometric mean of α was 13 at

stagnation point 1 and 80 at stagnation point 2. The values of α estimated from the mixing width fluctuated much more because of the high sensitivity of α to small changes in $s_{R,p}/s_{R,H}$ according to equation 5.40.

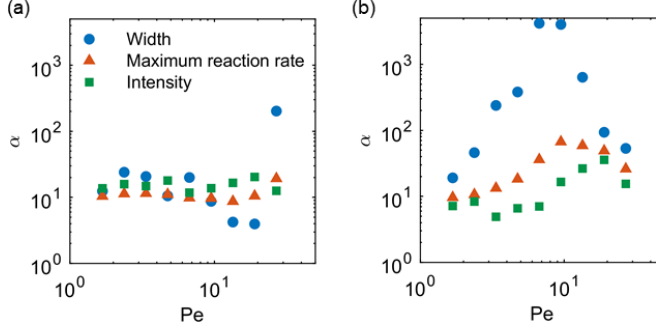


Figure 5.8. Calculated ratio of the compression rate in the porous medium and the Hele-Shaw cell for (a) stagnation point 1 and (b) stagnation point 2.

5.4.3. Stretching and compression

To explain the differences in compression rates estimated from the conservative and reactive mixing experiments, flow in the experimental geometries was simulated (Figure 5.9a,b). The compression rate was calculated in a streamline coordinate system following the method of Dentz et al. (2016). The evolution of the distance of two adjacent particles $z(t)$ can be written as:

$$\frac{dz(t)}{dt} = \epsilon(t)z(t) \quad (5.43)$$

where $\epsilon(t) = \nabla v(t)^T$ is the velocity gradient tensor. In the streamline coordinate system, $z(t)$ is transformed to $z'(t) = A^T z(t)$, where $A(t) = [v(t), w(t)]/v(t)$ with $v(t) \cdot w(t) = 0$ and $|w(t)| = v(t)$. Thus, in the streamline coordinate system it can be obtained that (Dentz et al. 2016):

$$\frac{dz'(t)}{dt} = [Q(t) + \tilde{\epsilon}(t)]z'(t) \quad (5.44)$$

where $\tilde{\epsilon} = A^T(t)\epsilon(t)A(t)$ and $Q(t) = \frac{dA^T(t)}{dt}A(t)$. The compression rate can be estimated from the component $\tilde{\epsilon}_{11}(t)$, which is equal to $dv_s[s(t)]/ds$, where v_s is the streamline velocity and $s(t)$ is the distance that a particle travelled along the streamline.

5. Mixing-induced reactions at stagnation points

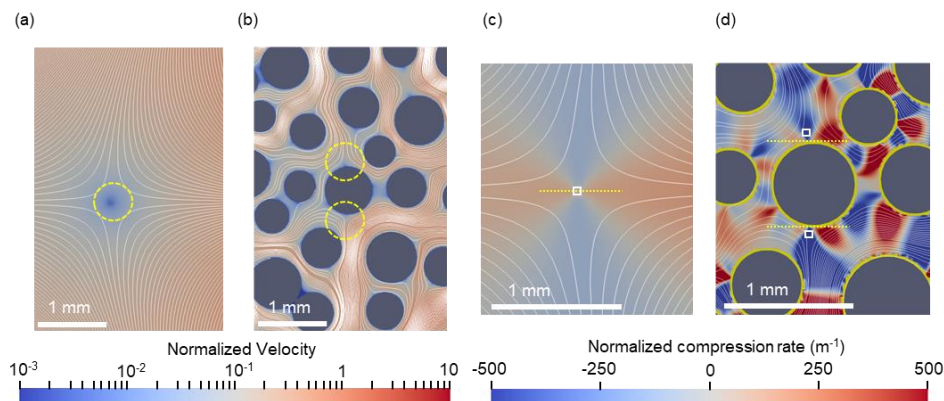


Figure 5.9. Simulated streamlines and velocity fields normalized by the total injection flow velocity in the (a) Hele-Shaw cell and (b) porous medium near the stagnation points. The yellow circles indicate the stagnation points. In addition, the calculated compression rate field around stagnation points normalized by the total injection flow velocity is shown for the (c) Hele-Shaw cell and (d) porous medium, where negative compression rates indicate stretching. The yellow dotted lines represent the position where the concentration profiles for the two stagnation points were determined in the experiments. The yellow lines around the grains indicate the absence of a calculated compression rate. The white squares represent the positions where the average compression rate was calculated for the reactive transport experiment.

The obtained pore scale compression rate maps are shown in Figure 5.9c,d. For the Hele-Shaw cell, the compression rate is very regular and follows the typical saddle point pattern. In the porous medium, stretching and compression are very heterogeneous and act intermittently along a given streamline. The maps qualitatively show that the compression rate appears to be generally higher in porous media. The average compression rate in the area at the stagnation point (white box in Figure 5.9c,d, $60\mu\text{m} \times 60\mu\text{m}$) was determined for the Hele-Shaw cell and the porous medium. As expected, the compression rate was approximately proportional to Pe (Figure 5.10a). The average compression rate in the porous medium was respectively 70 and 40 times larger than in the Hele-Shaw cell for the two selected stagnation zones (Figure 5.10b). The higher compression rate in the porous medium was interpreted as the result of flow channelling that developed in the porous medium, leading to large velocities at the stagnation points (Figure 5.11). Such channelling was also observed when the point injection was moved to a different position (Figure 5.11b,c,d) and has also been widely reported in other studies (e.g. de Anna et al. 2013, Alim et al. 2017). At the convergence point between two flows, high velocity channels meet the opposing flow leading to highly compressed mixing fronts at stagnation points. Because low velocity

zones typically develop between grains, the stagnation points at the convergence zone do not develop in these areas.

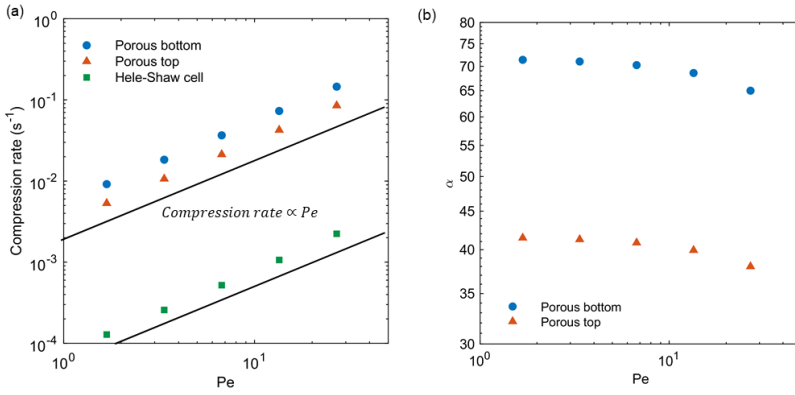


Figure 5.10. (a) Calculated compression rate based on the simulations at the stagnation point. (b) Calculated ratio of compression rate relative to Hele-Shaw cell.

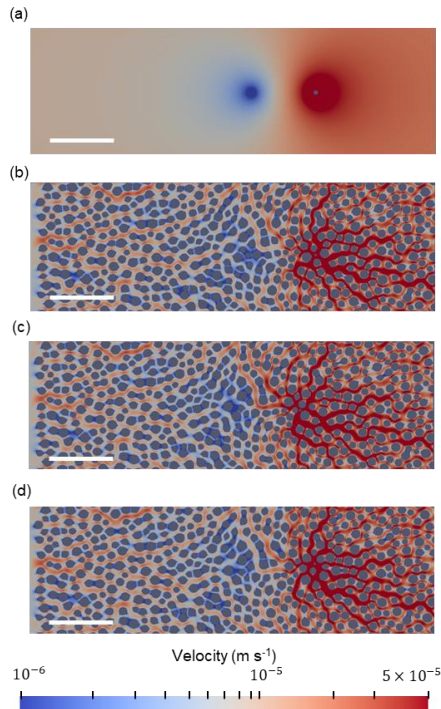


Figure 5.11. (a) The velocity field in the Hele-Shaw cell and (b-d) in the porous medium with different positions of the point injection. The background flow is from left to right. The point injection is located at the center of the high flow velocity zone. The white bar represents 5 mm.

5. *Mixing-induced reactions at stagnation points*

The ratio of compression rates in porous media compared to the Hele-Shaw cell obtained in these simulations is consistent with those estimated for the reactive tracer experiments, and thus explain the difference in reaction width, maximum reaction rate and integrated reaction rates. The estimated ratio of compression rates was however much smaller for the conservative tracer (Figure 5.4b). This difference might be due to averaging effects associated with the imperfect two-dimensional velocity field in the porous medium. This highlights the interest of reactive mixing experiments, which appear to be less sensitive to concentration averaging effects.

5.5. Conclusions

The dynamics of mixing and reaction in stagnation points were investigated using theoretical derivations, conservative and reactive tracer experiments and numerical simulations. The theoretical results allowed predicting the control of the mixing width, the reaction width, the maximum reaction rate and the integrated reaction rate at the stagnation point as a function of the dimensionless parameters Pe and Da . These results were successfully verified for both the Hele-Shaw cell and a porous medium, although the results for the porous medium were more noisy due to strong fluctuations of the pore water velocity. In relation to the SIP response of calcite, these findings suggest that temporal dynamics of the SIP response will be a function of Pe following the scaling of the maximum reaction rate ($\propto Pe^{2/3}$) because this reaction rate controls the closing of the pore space.

The compression rate was found to be much larger in the porous medium than in the Hele-Shaw cell for a given average velocity, which leads to much larger reaction rates. This enhanced compression was confirmed by numerical simulations and linked to the strong flow channeling that develops in porous media. In future work, it may be possible to predict this enhanced compression from the statistics of pore scale velocities, which are expected to follow an exponential probability density function in porous media (Alim et al. 2017).

These findings provide new insights into coupled mixing and reaction at stagnation points, which are hot spots of reaction in porous media (Bresciani et al., 2019; Dentz et al., 2016; Hester et al., 2017; Hidalgo et al., 2015). Future investigations will consider variations in the reaction rate to investigate the derived dependency of the reaction width and rates on the Damköhler number.

Chapter 6

Conclusions and Outlook

In this chapter, the general conclusions for the thesis will be presented first. Based on these conclusions, an outlook for future research will be provided.

6.1. Conclusions

Previous studies have shown that SIP has potential to detect and monitor subsurface biochemical reactions. However, the interpretation of the SIP response often remained qualitative because many experimental setups have limited resolution in time and space even though biochemical reactions are spatially highly variable and temporally dynamic. In addition, many of these previous studies relied on indirect information (e.g. fluid samples) and assumed that processes occur homogeneously in the measurement zone. Among the various applications of SIP measurements, the in-situ detection and monitoring of calcite precipitation in a non-destructive manner is important for a range of engineering applications. In this context, the overall aim of this thesis was to improve understanding of how spatially variable and temporally dynamic calcite precipitation affects the SIP response. In order to address this overall aim, three sub-objectives were formulated.

The first sub-objective was to investigate the effect of solute concentration on the SIP response of calcite precipitation and was addressed in Chapter 3. This objective was motivated by inconsistent results for the SIP response during calcite precipitation in previous studies. For example, the SIP response did not increase with an increasing amount of calcite precipitation in Zhang et al. (2012), and the increase in imaginary conductivity during calcite precipitation varied by an order of magnitude in different studies (Saneiyani et al., 2018; Wu et al., 2010, 2011). Furthermore, mechanistic models developed to describe the SIP response of calcite were parameterized by assuming that solute concentration was homogenous within the column (Leroy et al., 2017), which is typically not valid in the case of reactive transport problems. In order to address the first sub-objective, a four-phase experiment with SIP measurements on a column filled with sand was performed. In phase I, calcite precipitation was generated for a period

6. Conclusions and Outlook

of 12 days by co-injecting Na_2CO_3 and CaCl_2 solutions through two different ports. Because the resulting mixture was highly oversaturated with respect to calcite, this resulted in a well-defined calcite precipitation front and an associated increase in the imaginary part of the conductivity. In phase II, diluted (but still oversaturated) solutions were injected into the column. This resulted in a clear decrease in imaginary part and real part of the conductivity. The analysis of the relationship between imaginary part and real part of the conductivity showed that the SIP response of calcite has a stronger dependence on the solute conductivity than sand and sandstone. In phase III, the injection of the two solutions was stopped while calcite precipitation continued, which resulted in a decrease in the solute concentrations in the mixing zone. Again, this decreased imaginary part of the conductivity while real part of the conductivity varied by $\pm 5\%$ only. Finally, the injection rate of the Na_2CO_3 solution was reduced relative to that of the CaCl_2 solution in phase IV. This resulted in a shift of the mixing zone away from the calcite precipitation front established in phase I and an associated decrease of imaginary part of conductivity. These results imply that the SIP response of calcite is highly sensitive to the solute concentration near the precipitates. Based on this conclusion, the relatively large SIP response reported by Wu et al. (2010) compared to other studies (Saneiyani et al., 2018; Wu et al., 2011; Zhang et al., 2012) is attributed to the high solute concentration used in this study. In particular, Wu et al. (2011) used much lower concentrations of Ca^{2+} and dissolved carbonate concentrations. Zhang et al. (2012) used silica gel that strongly adsorbed Ca^{2+} and also used lower concentrations of Ca^{2+} and dissolved carbonate. In the study of Saneiyani et al. (2018), the calcite precipitation may not have overlapped with the mixing zone of the two solutions because of the unclear calcite distribution. Overall, this column experiment demonstrated that the SIP response of calcite precipitation strongly depends on the solute concentration in the vicinity of the calcite precipitation.

The second sub-objective was to develop a laboratory experimental setup that enables direct visual observation of calcite precipitation processes while making SIP measurements, and to use this set-up to investigate how spatial variation and temporal dynamics of calcite precipitation affect the SIP response. This sub-objective was addressed in Chapter 4. A novel millifluidic experimental set-up was successfully developed, which enabled visual observation of calcite precipitation processes in 2D porous media while making SIP measurements. The millifluidic set-up consisted of a 2D porous medium and a sample holder. The 2D porous medium had pillars with a height of 1 mm on a transparent base manufactured with the soft lithography method. The sample holder was made of three transparent poly(methyl methacrylate) (PMMA) plates. Using these three plates and the 2D porous medium, a millifluidic set-up was obtained with two fluid injection ports, one fluid outlet port and current and potential electrodes for SIP measurements. Process visualization was achieved with two types of cameras. The first type of camera was a regular mirrorless camera with a resolution of 0.03×0.03 mm per pixel that allowed to capture the entire measurement region. The second type of camera was a high-zoom camera with a resolution of 0.37×0.37 μm per pixel, which was sufficient to image individual

calcite crystals. This high-zoom camera was mounted on a two-axis moving table to take time-lapse images at selected positions. In a first experiment using this novel experimental set-up, calcite precipitation was induced by co-injecting the Na_2CO_3 and CaCl_2 solutions already used in Chapter 3 while making SIP measurements in three distinct regions and taking large-scale images as well as high-zoom images. After the experiment, the height of the calcite precipitation was measured to establish a calibration function between image grey level and the height of the precipitation. This calibration was then used to estimate the total mass of precipitates and the distribution of the height of the precipitates as a function of time. Based on the image analysis and SIP measurements, the experimental results could be divided in two distinct phases. In the first phase, the mass of calcite precipitates increased due to the creation of a wall-like calcite precipitation front along the zone where the two solutions mixed. During this first phase, the SIP response did not substantially increase. This is consistent with the results presented in Chapter 3, where the SIP response only started to increase after four days despite significant amounts of calcite precipitation. In the second phase, the mass of calcite increased only slightly in the area with the calcite precipitation front, but the SIP response strongly increased. Specifically, an increase in total calcite mass of only 2% was associated with a more than twofold increase in the imaginary part of the conductivity. During the second phase, the real part of the electrical conductivity decreased at 1Hz, while it was almost constant at 10kHz. Negative values for the imaginary part of the conductivity were also observed, which is usually attributed to measurement errors. Additionally, the peak frequency of the SIP response was higher for the upstream measurement region. From the experimental results, it was concluded that the most important mechanism determining the increase in the SIP response was associated with the closing of the gap space between the top of the calcite precipitation and the inner wall of the sample holder (i.e. the height of the calcite precipitation). This was confirmed by a simplified electrical circuit model, where the calcite precipitation front was modeled as a capacitance and the water above the calcite wall and the water on both sides of the calcite was modeled as resistances. In this simple model, a small increase in the height of the calcite wall results in a large increase in the imaginary part of the electrical conductivity when the height of calcite wall is very close to the height of the porous media. In addition, electric field simulations based on the imaged distribution of calcite precipitation were performed to further improve interpretation of the SIP measurements. Based on the simulation results, it was concluded that the observed differences in peak frequency between the different measurement regions are due to the shape of the calcite precipitation front. In addition, it was concluded from these simulations that the imaginary part of the measured electrical conductivity values can become negative when the strength of the polarization varies along the calcite precipitation. It was also found that the strength of the SIP response is sensitive to the continuity of the calcite precipitation front. In previous studies, the origin of the SIP response of calcite has often been attributed to grain polarization associated with the electric double layer. The experimental results, the electric field simulations, and the simplified electric circuit model presented in this chapter highlight the importance of considering the shape and position of the calcite precipitation

6. Conclusions and Outlook

front and suggest that Maxwell-Wagner polarization played an important role in determining the SIP response of calcite precipitation. Nevertheless, it was not possible to exclude a contribution from grain polarization. Overall, it was concluded that the SIP response of calcite precipitation was not simply determined by the mass of calcite, but that the spatial distribution and temporal dynamics of calcite precipitation were important factors that determined the SIP response.

Chapter 4 showed the importance of understanding the spatial distribution of chemical reactions in porous media for the improved interpretation of the SIP response during calcite precipitation. Specifically, stagnation points play an important role for precipitation reactions in porous media because they act to elongate mixing interfaces and increase chemical gradients. Therefore, the third and final sub-objective was to investigate the scaling of the width, maximum reaction rate and reaction intensity at the stagnation point for different Péclet (Pe) numbers, and to explore the difference of these reaction characteristics at the stagnation point with and without the presence of a porous medium. This sub-objective was addressed in Chapter 5. First, scaling laws at the stagnation point were theoretically derived by applying mixing theory to a bimolecular reaction system. The derivation started by considering the deformation of incompressible small fluid elements called lamella. The lamella is compressed exponentially as a function of time when the fluid element is transported close to the stagnation point. By considering the diffusion of solutes in the lamella, the mixing width is expected to follow $Pe^{-1/2}$ for the conservative case. For the reactive case, the compression-diffusion-reaction equation was considered in a local Lagrangian frame moving with the lamella. This equation can be simplified by introducing non-dimensional time and length scales defined using the size of lamella that changed over time. The simplified equation had a similar form as the diffusion-reaction equation in biomolecular reaction systems, which allowed the use of the solution method of Larralde et al. (1992) for bimolecular reaction systems to obtain the required scaling laws. In particular, the following scaling laws were obtained for the reactive case in the case of a Damköhler number $Da > 1$: 1) the reaction width follows $Pe^{-1/6}Da^{-1/3}$, 2) the maximum reaction rate follows $Pe^{2/3}Da^{1/3}$ and 3) the reaction intensity follows $Pe^{1/2}$. In a next step, these theoretical derivations were compared with experimental results obtained in the millifluidic set-up already used in Chapter 4. Experiments using a conservative tracer in a Hele-Shaw configuration without porous medium showed that the mixing width followed the theoretically derived scaling law. Similar experiments with porous medium showed that the mixing width also globally followed the scaling law in this case. However, large fluctuations and stronger compression were observed. Next, reactive transport experiments with a $Da > 1$ were performed in the millifluidic set-up. The experimental results for the Hele-Shaw configuration without porous media followed the theoretically derived scaling laws as a function of Pe , and the scaling laws were also globally applicable in the presence of a 2D porous media. It was also found that the reaction front in porous media showed larger fluctuations and stronger compression than in the Hele-Shaw configuration. These tendencies were qualitatively consistent with the conservative case. To understand the difference

between the results in the absence and presence of a porous medium, a compression rate map was calculated based on a numerically simulated velocity field. The larger fluctuations in the porous medium were attributed to the large spatial variation of this compression rate. Such variations resulted in large changes in the compression rate even with small shifts of the stagnation point. Additionally, it was considered that the stronger compression associated with the grains in the porous medium created a channel with high flow velocity toward the stagnation point, which worked to preserve the flow velocity toward the stagnation point based on the numerically simulated velocity field. In conclusion, this chapter described the theoretical derivation and experimental validation of novel scaling laws of chemical reaction dynamics at stagnation points as a function of Pe .

Overall, this thesis provided five key findings about the SIP response associated with spatially variable and temporally dynamic calcite precipitation. First, it was found that the solute concentration near the calcite precipitation largely affects the SIP response. In particular, the imaginary part of the electrical conductivity changed by a factor of 10 depending on the solute concentration near the calcite precipitation. Second, the closing of the pore space largely increased the SIP response because an increase of only 2% in total mass of calcite precipitation increased the imaginary conductivity by a factor of 2. Third, the spatial distribution of the calcite precipitation resulted in different peak frequencies in different measurement regions and a negative imaginary part of the electrical conductivity. Fourth, Maxwell-Wagner polarization played an important role in determining the strength of the SIP response. Finally, mathematical analysis and numerical simulations suggest that the temporal dynamics of the SIP response will be a function of Pe following the scaling of the maximum reaction rate ($\propto Pe^{2/3}$) because this reaction rate controls the closing of the pore space. Taken together, these five findings describe key factors controlling the SIP response of calcite, and help to understand previously reported inconsistent experimental results. Therefore, this thesis provides substantial progress for research dealing with the SIP response of calcite.

6.2. Outlook

There is a wide range of additional opportunities for future research based on the results presented in this thesis. This thesis highlighted the importance of considering the spatially variable and temporally dynamic calcite precipitation process in the interpretation of the SIP response. However, the development of calcite precipitation in this thesis was monitored in one flow condition only where a point source resulted in a U-shaped precipitation front. In addition, calcite precipitation was only induced chemically in highly oversaturated conditions without involving biological processes. Clearly, it would be worthwhile to perform additional experiments with the millifluidic set-up developed in this thesis. One interesting case would be to inject two fluids in parallel so that the mixing front will be just a line without curvature, ideally in a Hele-Shaw configuration without porous medium. By creating a

6. *Conclusions and Outlook*

mixing and precipitation front perpendicular to the electric current flow, it may be possible to investigate how the direction of electric current relative to the orientation of the calcite precipitation affects the bulk SIP response. The use of highly oversaturated solutions in this thesis resulted in metastable amorphous calcium carbonate precipitates before calcite formation (Rodriguez-Navarro et al., 2016). This can be avoided by injecting solutions with lower concentrations, although it will then take more time to establish the calcite precipitation front. This would allow to compare the SIP response of calcite formed in different conditions. In addition, it would be interesting to investigate the SIP response associated with the dissolution of calcite. This has not been investigated yet in previous SIP studies on calcite. Furthermore, calcite precipitation induced by enzymes (Wu et al., 2011) or microbes may also be investigated using the millifluidic set-up. Results from Wu et al. (2011) suggest that microbially-induced calcite precipitation (MICP) also induced a SIP response, but that the magnitude of this response was too small to detect in field conditions. Zhang et al. (2012) also investigated MICP in laboratory conditions and did not observe a significant SIP response. On the other hand, Saneiyani et al. (2019) successfully used SIP to detect MICP in field conditions. It is worthwhile to investigate these contradicting results using the novel experimental approach developed in this thesis. For example, the chemical conditions in the field could be reproduced in the millifluidic set-up, which would make it possible to evaluate whether there can be other types of mineral precipitation as a result of MICP.

Besides the SIP response of calcite, this thesis also intensively investigated flow dynamics at the stagnation point both theoretically and experimentally. There is a range of interesting follow-up research topics relying on the millifluidic set-up. This includes further study of enhanced compression in porous media. It was found in Chapter 4 that this enhanced compression was due to the flow channel with high flow velocity. It might be possible to predict this enhanced compression in relation to the statistics of the pore connectivity, which is found to follow exponential probability density function (Alim et al., 2017). Many previous studies about pore scale solute spreading and reaction have investigated 2D domains (e.g. de Anna et al., 2014; Jiménez-Martínez et al., 2015; Zhang et al., 2010), where compression and elongation are normally algebraic except at stagnation points where they are exponential. In 3D porous media, compression and elongation are always exponential (Lester et al., 2013) and thus much stronger than in 2D. Hence, the investigation of stagnation points in 2D is of interest to study compression and elongation in 3D. For example, the millifluidic set-up can be used to monitor the growth of crystals or bacteria at the stagnation point for different flow conditions. This would allow to investigate how exponential compression affects crystal or bacteria growth. It is also interesting to theoretically and experimentally investigate reactivity and adsorption phenomena at solid interfaces (e.g. dissolution of calcite) as a function of flow velocity. In addition, the compression rate map used in Chapter 5 can be further used to investigate patterns of compression and elongation in relation to pore geometry. In previous studies, the intermittent compression and elongation was investigated along stream lines only (de Anna et al., 2013). The 2D or 3D maps of the compression rate

field make it possible to study the spatial correlation of the compression rate and thus to characterize patterns of compression and elongation. Finally, biochemical processes in porous media can be systematically investigated using microfluidic or millifluidic set-ups. It would be particularly interesting to design a microfluidic chip with a flow channel that includes several stagnation points. With such a configuration, it would be possible to focus on investigating the effects of deformation of fluid elements and it would eliminate the effects of pore space geometry and grain boundaries.

In addition to future research directly derived from the work presented in this thesis, there are ample additional opportunities to apply the novel millifluidic set-up. Obviously, the setup is not restricted to investigating calcite precipitation and also holds great promise to investigate the origins of the SIP response of other biochemical reactions in future experiments. For example, it has been shown that SIP is sensitive to the formation of conductive minerals such as iron-oxides and that the transformation of iron minerals influences the SIP response (Ntarlagiannis et al., 2010; L. Slater et al., 2007). The millifluidic set-up would allow monitoring of the mineral formation, and could provide supporting information on size, shape and mineral type. Given that SIP is highly sensitive to the presence of conductive materials, the SIP response should be strong and relatively easy to interpret without detailed consideration of potential measurement errors. In the same context, conductive biologically induced mineral precipitation can be also investigated in the millifluidic set-up. For example, it would be interesting to investigate the iron-oxidizing bacteria *Gallionella* (Bochet et al., 2020), which is known to induce precipitation of iron minerals in the fractured rock of the Ploemeur observatory, France. The millifluidic set-up can also be used to investigate the effect of saturation on the SIP response, particularly in the context of biochemical reactions. Most previous studies in this direction focused either on biochemical reactions or saturation (e.g. Breede et al., 2011), and the combined effects of saturation and biochemical reactions have rarely been investigated. Clearly, the distribution of water and the availability of gas species such as oxygen and carbon dioxide will affect the biochemical reactions, and thus likely also the SIP response. It has been shown that the saturation in the type of millifluidic set-ups used in this thesis can be controlled by flowing air and water at the same time (Jiménez-Martínez et al., 2017). Thus, the millifluidic set-up can be used to monitor the distribution of water and air as well as biochemical reactions while making SIP measurements.

The laboratory studies presented in this thesis are also useful to obtain new insights for field applications of SIP. A straightforward approach for this is to establish quantitative relationships between the SIP response and biochemical reactions in laboratory experiments using the millifluidic set-up, and to use these relationships for the interpretation of field measurements. The experiments in this thesis showed promising results in this direction. For example, it may be possible to reproduce field conditions in the millifluidic set-up and to investigate how the bulk SIP response changes with the distribution and total intensity of the biochemical reactions. Laboratory investigations are also important to investigate how unresolved spatial variation below the resolution of field measurements affects the SIP response. For

6. Conclusions and Outlook

example, the millifluidic experiments showed that the shape of the precipitation front influenced the peak frequency, which may be of importance in the interpretation of field data.

In addition to the SIP response, the millifluidic set-up used in this thesis also successfully captured the details of the precipitation process down to the formation of individual crystals. Visual observations of crystallization in porous media have been used in several studies already (Zhang et al., 2010) and has recently also been implemented in microfluidics (Kim et al., 2020). Thus, another interesting research topic related to precipitation processes in porous media is to investigate the effects of crystallization pressure on porous media properties (Desarnaud et al., 2016). For this, crystallization could be induced by injecting a solution radially in a porous medium composed of movable grains in a millifluidic or microfluidic setup. Using this approach, it should be possible to observe patterns of wave fronts that may have a similar shape as the patterns observed in Hele-Shaw configurations (Schusztter et al., 2016). It is also interesting to experimentally investigate salt precipitation in the context of evaporation processes using millifluidic or microfluidic setups. This would allow to simultaneously observe the development of the water distribution and salt precipitation. Even though there are a few studies in this direction (e.g. Rufai & Crawshaw, 2017), the pore-scale processes controlling salt precipitation during evaporation have not been investigated in detail yet.

A range of studies have investigated subsurface processes associated with bacteria growth using SIP (e.g. Ntarlagiannis et al., 2005). The millifluidic set-up developed in this study is also expected to improve understanding of the SIP response of bacteria. In order to illustrate the potential of the millifluidic set-up in this context, a preliminary experiment was performed. The target bacteria species was *Shewanella oneidensis*, which has the potential for soil decontamination of metals (Mellage et al., 2018). The SIP response of this bacteria has already been studied by Mellage et al. (2018), where *Shewanella* was grown in a column experiment in anoxic conditions. The column was filled with a layer of iron-coated sand and a layer of pure quartz sand. SIP measurements during growth showed an increase in the imaginary part of the conductivity (σ'') in both the iron-coated and the quartz sand layer. Following this work, the aim of this preliminary experiment was to understand the relationship between the growth of bacteria and the SIP response in porous media. For this, a bacteria solution in exponential growth phase was prepared. This bacteria solution was diluted with Lysogeny broth (LB) to adjust the concentration to 10^8 cells per ml. In a next step, the millifluidic set-up was first filled with LB solution, and then the LB solution was replaced by the diluted bacteria solution. The development of the SIP response was monitored without flow in the cell, and large-scale images were taken at regular intervals. After 90 h, the bacteria solution was replaced by LB solution again using a high flow velocity in an attempt to flush the bacteria from the porous media. After the experiment, part of the porous media was removed from the flow cell to acquire scanning electron microscope (SEM) images. The imaging results from this experiment showed an increase in grey level over time, which was clearly related to bacterial growth (Figure 6.1). The SIP response increased up to around 20 h, which corresponded well with the

increase in normalized image grey value that represents the concentration of bacteria (Figure 6.2). After flushing, the grey value decreased. This suggests that the concentration of bacteria decreased. Unexpectedly, the SIP response did not change after flushing. SEM images showed the existence of bacteria on the porous media, but byproducts of the bacteria (e.g. biofilm) were not observed (Figure 6.3). These results indicate that the growth of the bacteria increased the SIP response, but that this cannot be fully attributed to the increase in the concentration of bacteria. These preliminary results highlight that the millifluidic set-up can be applied to investigate the SIP response of bacterial activity. However, a major limitation of the experimental set-up used in this thesis is the inability to directly monitor biological processes, such as the increase in the number of bacteria cells or biofilm formation.

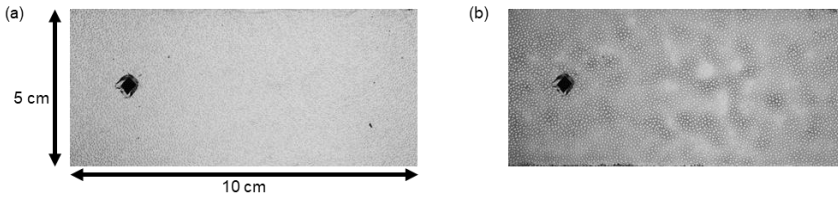


Figure 6.1. Photos of porous media (a) at the start of the experiment and (b) just before flushing.

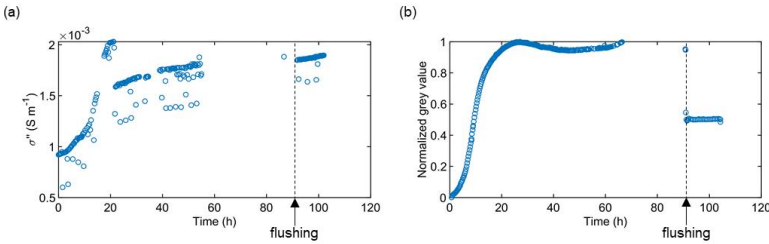


Figure 6.2. Change in (a) σ'' and (b) normalized grey value of the porous media. The dotted line indicates the time when the millifluidic set-up was flushed. It should be noted that the SIP measurements showed a sudden jump in σ'' at 22 hours due to an unknown error.

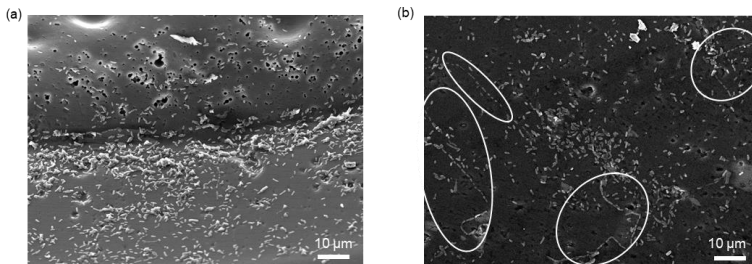


Figure 6.3. SEM images of flushed porous media after the experiment (a) near the grain and (b) on the bottom of the sample holder where some bacteria streamers can be observed.

6. *Conclusions and Outlook*

In order to improve the ability to directly observe biological processes, further miniaturization of the millifluidic set-up is desirable. This would allow the use of techniques developed for microfluidic applications that allow the monitoring of biological processes using microscopes (Son et al., 2015). Given the design considerations for accurate SIP measurements in the millifluidic set-up discussed in Chapter 2, further reductions in size seem feasible. Future work with such an SIP-microfluidic set-up could consist of two steps. First, the microfluidic set-up should be tested using colloid particles of different size in order to confirm that accurate SIP measurements can be achieved. In a second step, the effect of the growth of bacteria, biofilms and biomineralization can be investigated. Since the peak frequency of the SIP response is expected to depend on the size of the polarization object, bacteria cells, biofilms and biominerals are expected to have different peak frequencies as a first approximation. In such experiments, it may be helpful to use different types of bacteria, mutants, or even other types of cells in addition to variable flow and nutrient conditions in order to better pinpoint the source of the SIP response. For example, it would be beneficial to use cells whose behavior is well known and simple, such as yeast (a fungi). Such research might even have impact beyond the geosciences when low frequency AC currents used in SIP measurements can be used to investigate microbial processes or to determine characteristics of bacterial cells. There are already some studies that investigated the dielectric properties of bacteria cells in the frequency range of SIP measurements, but they used two electrode systems (Prodan et al., 2004; Zhang et al., 2013) where it was difficult to make precise measurements due to electrode polarization. Four electrode systems have been rarely used (Mazzeo, 2009; Pilawski, 2019; Zhang et al., 2014), but likely provide better measurement precision in the mHz to kHz frequency range.

The SIP-microfluidic set-up proposed above can potentially also be used to further investigate and validate fundamental theories related to the source of the SIP response using microscopic observations. For example, it is widely accepted that the SIP response is associated with the polarization of electric double layers present in porous media. However, the experimental validation of this theory using non-conductive materials is quite limited, and should be improved. One attempt using SIP measurements on packed glass beads was presented in Leroy et al. (2008). However, the possibility of membrane polarization cannot be ignored in such packed systems. In order to address this challenge, systematic SIP measurements using varying materials, size of the samples and different solutions in a wide frequency range (1 mHz – 1 kHz) can be performed using the SIP-microfluidic setup. This setup is especially useful for this purpose because the requirements for the amount of sample is small. Thus, it is possible to use micrometer-sized materials with a well-controlled size range, which would be too expensive to investigate in classical SIP measurement set-ups with a much large sample volume. In addition, it would be possible to visually confirm that particles are not aggregated. It is also interesting to fabricate 2D porous media with high surface area for such microfluidic experimental setups and to consider techniques to modify the surface charge of the 2D porous media. Such 2D artificial porous

media would be particularly suitable for validating grain surface polarization models because the positions of the grains are defined and separated. Finally, a broader database for model testing would also be beneficial to explore how the number of free parameters in the grain polarization model can be reduced.

The theoretical framework developed in Chapter 5 used a lamella description to investigate the reaction dynamics at the stagnation point. In future work, the lamella description of mixing can also be used to improve understanding of dispersivity in geological materials. One of the common drawbacks of the classical advection-dispersion equation applied to geological media is that the dispersivity is assumed to be constant. In reality, dispersivity is known to increase with increasing observation scale (Gelhar et al., 1992). In addition, the scaling of the dispersion coefficient as a function of Pe is known to change at $Pe = 1$ (Delgado, 2007). In conditions with high Pe , the dispersion coefficient increases with Pe , whereas it is constant for low Pe . Dispersivity can be defined as the length scale of a perfectly mixed cell, in which gradients in solute have vanished when the porous media is discretized in 1D (Aris & Amundson, 1957). An increasing dispersivity with observation scale thus suggests that the solute is not mixed perfectly. Also, an increasing dispersivity with Pe suggests that the length scale of the perfectly mixed cell depends on Pe . This is consistent with a lamella description of mixing, where the concentration gradient in lamella can be high in high Pe conditions. In these conditions, it is possible that distinct lamellas are present and that solutes are not perfectly mixed, or that a large length scale is needed for perfect mixing of solutes. When the Pe is low, the concentration gradients in the lamella are also small, and lamella coalesce. In these conditions, it may thus be possible to reach the length scale representing perfectly mixed cells. Therefore, the interpretation of dispersivity as a function of Pe and observation scale could be improved if the development of lamella around $Pe = 1$ is investigated.

In addition to the experimental and theoretical studies suggested above, there also is potential to extend the presented research using pore-scale simulations. In this thesis, electrical field simulations were restricted to the REV scale with effective electrical properties for the calcite and background. Given the importance of pore scale processes as revealed in Chapter 4, simulations with higher resolution and a resolved pore would be beneficial to further improve understanding of the SIP response in porous media. The higher resolution required to resolve the pore scale of the millifluidic set-up can be achieved using OpenFOAM (Figure 6.4). This will make it possible to run simulations where the water phase and calcite precipitation are fully resolved. Such a model can then be used to systematically investigate how heterogeneity in calcite precipitation influences the SIP response by changing the shape of the precipitation front, not only in 2D but also in 3D. For example, it is interesting to investigate how the creation of a flow barrier for electric current influences the SIP response based on the discussion in Chapter 4. In particular, the simulations could be used to investigate the critical wall height required to increase the bulk SIP response as discussed in Chapter 4. In addition to electric flow field simulations, it may also be possible to simulate the development of calcite precipitation and the resulting SIP

6. Conclusions and Outlook

response by combining reactive transport simulations, as already presented in Chapter 5, and electric field simulations. Of course, such pore-scale simulations would still be a simplified representation because it will not be possible to model polarization of the electrical double layers directly. Such a combined modelling has not been attempted before, and will thus provide new opportunities to further investigate how pore scale processes and pore geometry influence the SIP response. It is also feasible to perform such simulations in 3D, which would help to overcome some of the experimental limitations of the 2D millifluidic set-up.

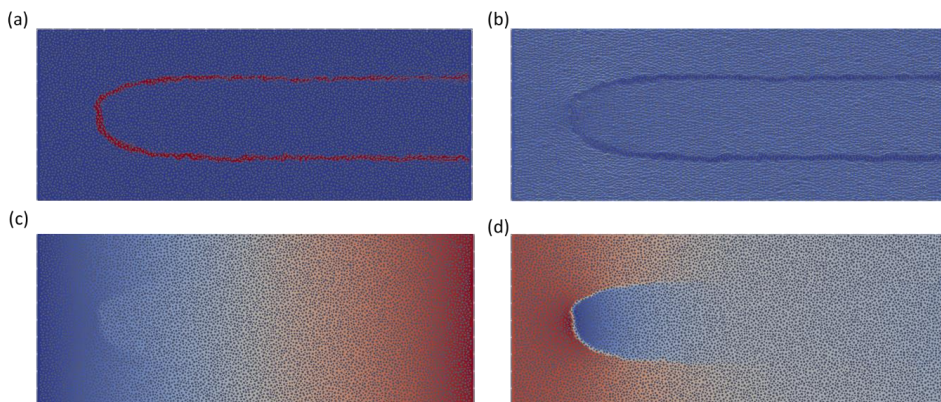


Figure 6.4. Example of pore scale electric field simulation using OpenFOAM, where electric current was injected from right boundary. (a) red part has non-zero imaginary conductivity, representing the shape of calcite precipitation front. (b) Simulated electric current flow, where brighter color represents higher current. Simulated (c) real part and (d) imaginary part of the electric potential where the red color represents larger absolute values.

Overall, it is clear that the research presented in this thesis can be a starting point for many applications of the novel millifluidic set-up. Such possibilities are based on the successful development of the experimental setup and rigorous interpretation of the results in combination with numerical simulations. The wide range of suggested future research reflects the interdisciplinary nature of this thesis.

References

- Abdel Aal, G. Z., Slater, L. D., & Atekwana, E. A. (2006). Induced-polarization measurements on unconsolidated sediments from a site of active hydrocarbon biodegradation. *Geophysics*, *71*(2), H13–H24.
- Abdel Aal, G. Z., Atekwana, E. A., & Atekwana, E. A. (2010). Effect of bioclogging in porous media on complex conductivity signatures. *Journal of Geophysical Research*, *115*, 1–10. <https://doi.org/10.1029/2009JG001159>
- Abdel Aal, G. Z., Atekwana, E. A., Slater, L. D., & Atekwana, E. A. (2004). Effects of microbial processes on electrolytic and interfacial electrical properties of unconsolidated sediments. *Geophysical Research Letters*, *31*(12). <https://doi.org/10.1029/2004GL020030>
- Alim, K., Parsa, S., Weitz, D. A., & Brenner, M. P. (2017). Local Pore Size Correlations Determine Flow Distributions in Porous Media. *Physical Review Letters*, *119*(14), 1–5. <https://doi.org/10.1103/PhysRevLett.119.144501>
- de Anna, P., Le Borgne, T., Dentz, M., Tartakovsky, A. M., Bolster, D., & Davy, P. (2013). Flow Intermittency, Dispersion, and Correlated Continuous Time Random Walks in Porous Media. *Physical Review Letters*, *110*(18), 184502. <https://doi.org/10.1103/PhysRevLett.110.184502>
- de Anna, P., Jimenez-Martinez, J., Tabuteau, H., Turuban, R., Borgne, T. Le, Derrien, M., & Méheust, Y. (2014). Mixing and Reaction Kinetics in Porous Media: An Experimental Pore Scale Quantification. *Environmental Science and Technology*, *48*, 508–516. <https://doi.org/10.1021/es403105b>
- Appelo, C. A. J., & Postma, D. (2007). *Geochemistry, groundwater and pollution 2nd edition*. Leiden, The Netherlands: Balkema Publishers.
- Archie, G. E. (1942). The electrical resistivity log as an aid in determining some reservoir characteristics. *Transactions of the AIME*, *146*(01), 54–62. <https://doi.org/10.2118/942054-G>
- Arcone, S. A., & Boitnott, G. E. (2010). Complex permittivity of common minerals and one soil at low water contents. In *Proceedings of the XIII International Conference on Ground Penetrating Radar* (pp. 1–6). IEEE. <https://doi.org/10.1109/ICGPR.2010.5550133>
- Aris, R., & Amundson, N. R. (1957). Some remarks on longitudinal mixing or diffusion in fixed beds. *AIChE Journal*, *3*(2), 280–282. <https://doi.org/10.1002/aic.690030226>
- Arvidson, R. S., & Mackenzie, F. T. (2000). Temperature dependence of mineral precipitation rates along the CaCO₃-MgCO₃ join. *Aquatic Geochemistry*, *6*(2), 249–256.

References

- <https://doi.org/10.1023/A:1009619426406>
- Bandopadhyay, A., Le Borgne, T., Méheust, Y., & Dentz, M. (2017). Enhanced reaction kinetics and reactive mixing scale dynamics in mixing fronts under shear flow for arbitrary Damköhler numbers. *Advances in Water Resources*, *100*, 78–95. <https://doi.org/10.1016/j.advwatres.2016.12.008>
- Batchelor, G. K., Howells, I. D., & Townsend, A. A. (1959). Small-scale variation of convected quantities like temperature in turbulent fluid Part 2. The case of large conductivity. *Journal of Fluid Mechanics*, *5*(01), 134. <https://doi.org/10.1017/S0022112059000106>
- Bochet, O., Bethencourt, L., Dufresne, A., Farasin, J., Pédrot, M., Labasque, T., ... Le Borgne, T. (2020). Iron-oxidizer hotspots formed by intermittent oxic–anoxic fluid mixing in fractured rocks. *Nature Geoscience*, *13*(2), 149–155. <https://doi.org/10.1038/s41561-019-0509-1>
- Le Borgne, T., Dentz, M., & Villiermaux, E. (2015). The lamellar description of mixing in porous media. *Journal of Fluid Mechanics*, *770*, 458–498. <https://doi.org/10.1017/jfm.2015.117>
- Borgne, Tanguy Le, Ginn, T. R., & Dentz, M. (2014). Impact of fluid deformation on mixing-induced chemical reactions in heterogeneous flows. *Geophysical Research Letters*, *41*(22), 7898–7906. <https://doi.org/10.1002/2014GL062038>
- Breede, K., Kemna, A., Esser, O., Zimmermann, E., Vereecken, H., & Huisman, J. A. (2011). Joint Measurement Setup for Determining Spectral Induced Polarization and Soil Hydraulic Properties. *Vadose Zone Journal*, *10*(2), 716–726. <https://doi.org/10.2136/vzj2010.0110>
- Bresciani, E., Kang, P. K., & Lee, S. (2019). Theoretical Analysis of Groundwater Flow Patterns Near Stagnation Points. *Water Resources Research*, *55*(2), 1624–1650. <https://doi.org/10.1029/2018WR023508>
- Briggs, M. A., Lautz, L. K., & Hare, D. K. (2014). Residence time control on hot moments of net nitrate production and uptake in the hyporheic zone. *Hydrological Processes*, *28*(11), 3741–3751. <https://doi.org/10.1002/hyp.9921>
- Burbank, M. B., Weaver, T. J., Green, T. L., Williams, B. C., & Crawford, R. L. (2011). Precipitation of calcite by indigenous microorganisms to strengthen liquefiable soils. *Geomicrobiology Journal*, *28*(4), 301–312. <https://doi.org/10.1080/01490451.2010.499929>
- Bussian, A. E. (1983). Electrical conductance in a porous medium. *Geophysics*, *48*(9), 1258–1268. <https://doi.org/10.1190/1.1441549>
- Chapelle, F. H. (2001). *Ground-water microbiology and geochemistry* (2nd ed). New York: Wiley.
- Chen, J., Hubbard, S. S., & Williams, K. H. (2013). Data-driven approach to identify field-scale

- biogeochemical transitions using geochemical and geophysical data and hidden Markov models : Development and application at a uranium-contaminated aquifer. *Water Resources Research*, *49*, 6412–6424. <https://doi.org/10.1002/wrcr.20524>
- Cuthbert, M. O., McMillan, L. A., Handley-Sidhu, S., Riley, M. S., Tobler, D. J., & Phoenix, V. R. (2013). A field and modeling study of fractured rock permeability reduction using microbially induced calcite precipitation. *Environmental Science and Technology*, *47*, 13637–13643. <https://doi.org/10.1021/es402601g>
- Davis, C. A., Atekwana, E., Atekwana, E., Slater, L. D., Rossbach, S., & Mormile, M. R. (2006). Microbial growth and biofilm formation in geologic media is detected with complex conductivity measurements. *Geophysical Research Letters*, *33*, 1–5. <https://doi.org/10.1029/2006GL027312>
- DeJong, J. T., Soga, K., Kavazanjian, E., Burns, S., Van Paassen, L. A., Al Qabany, A., ... Weaver, T. (2013). Biogeochemical processes and geotechnical applications: progress, opportunities and challenges. *Géotechnique*, *63*(4), 287–301. <https://doi.org/10.1680/geot.SIP13.P.017>
- Delgado, J. M. P. Q. (2007). Longitudinal and transverse dispersion in porous media. *Chemical Engineering Research and Design*, *85*(9 A), 1245–1252. <https://doi.org/10.1205/cherd07017>
- Dentz, M., Lester, D. R., Le Borgne, T., & de Barros, F. P. J. (2016). Coupled continuous-time random walks for fluid stretching in two-dimensional heterogeneous media. *Physical Review E*, *94*(6), 061102. <https://doi.org/10.1103/PhysRevE.94.061102>
- Desarnaud, J., Bonn, D., & Shahidzadeh, N. (2016). The Pressure induced by salt crystallization in confinement. *Scientific Reports*, *6*(1), 30856. <https://doi.org/10.1038/srep30856>
- Eriksson, R., Merta, J., & Rosenholm, J. B. (2007). The calcite / water interface I . Surface charge in indifferent electrolyte media and the influence of low-molecular-weight polyelectrolyte. *Journal of Colloid and Interface Science*, *313*, 184–193. <https://doi.org/10.1016/j.jcis.2007.04.034>
- Flores Orozco, A., Williams, K. H., Long, P. E., Hubbard, S. S., & Kemna, A. (2011). Using complex resistivity imaging to infer biogeochemical processes associated with bioremediation of an uranium - contaminated aquifer. *Journal of Geophysical Research*, *116*, G03001. <https://doi.org/10.1029/2010JG001591>
- Fu, F., Dionysiou, D. D., & Liu, H. (2014). The use of zero-valent iron for groundwater remediation and wastewater treatment: A review. *Journal of Hazardous Materials*, *267*, 194–205. <https://doi.org/10.1016/j.jhazmat.2013.12.062>
- Fujita, Y., Taylor, J. L., Gresham, T. L. T., Delwiche, M. E., Colwell, F. S., McIning, T. L., ... Smith, R. W. (2008). Stimulation of microbial urea hydrolysis in groundwater to enhance calcite

References

- precipitation. *Environmental Science and Technology*, 42(8), 3025–3032. <https://doi.org/10.1021/es702643g>
- Fujita, Y., Taylor, J. L., Wendt, L. M., Reed, D. W., & Smith, R. W. (2010). Evaluating the potential of native ureolytic microbes to remediate a 90Sr contaminated environment. *Environmental Science and Technology*, 44(19), 7652–7658. <https://doi.org/10.1021/es101752p>
- Gagnon, Z. R. (2011). Cellular dielectrophoresis: Applications to the characterization, manipulation, separation and patterning of cells. *Electrophoresis*, 32(18), 2466–2487. <https://doi.org/10.1002/elps.201100060>
- Gálfi, L., & Rácz, Z. (1988). Properties of the reaction front in an $A+B\rightarrow C$ type reaction-diffusion process. *Physical Review A*, 38(6), 3151–3154. <https://doi.org/10.1103/PhysRevA.38.3151>
- Gelhar, L. W., Welty, C., & Rehfeldt, K. R. (1992). A critical review of data on field-scale dispersion in aquifers. *Water Resources Research*, 28(7), 1955–1974. <https://doi.org/10.1029/92WR00607>
- Gomez, M. G., Martinez, B. C., DeJong, J. T., Hunt, C. E., deVlaming, L. A., Major, D. W., & Dworatzek, S. M. (2015). Field-scale bio-cementation tests to improve sands. *Proceedings of the Institution of Civil Engineers - Ground Improvement*, 168(G13), 206–216. <https://doi.org/10.1680/grim.13.00052>
- Gu, C., Anderson, W., & Maggi, F. (2012). Riparian biogeochemical hot moments induced by stream fluctuations. *Water Resources Research*, 48(9), 1–17. <https://doi.org/10.1029/2011WR011720>
- Hanai, T. (1960). Theory of the dielectric dispersion due to the interfacial polarization and its application to emulsions. *Kolloid-Zeitschrift*, 171(1), 23–31. <https://doi.org/10.1007/BF01520320>
- Havlin, S., Araujo, M., Larralde, H., Shehter, A., & Stanley, H. E. (1995). Anomalous kinetics in $A + B \rightarrow C$ with initially-separated reactants. *Chaos, Solitons & Fractals*, 6(94), 157–169. [https://doi.org/10.1016/0960-0779\(95\)80024-B](https://doi.org/10.1016/0960-0779(95)80024-B)
- Heberling, F., Bosbach, D., Eckhardt, J., Fischer, U., Glowacky, J., Haist, M., ... Schäfer, T. (2014). Applied geochemistry reactivity of the calcite – water-interface , from molecular scale processes to geochemical engineering. *Applied Geochemistry*, 45, 158–190. <https://doi.org/10.1016/j.apgeochem.2014.03.006>
- Hester, E. T., Cardenas, M. B., Haggerty, R., & Apte, S. V. (2017). The importance and challenge of hyporheic mixing. *Water Resources Research*, 53(5), 3565–3575. <https://doi.org/10.1002/2016WR020005>
- Hidalgo, J. J., Dentz, M., Cabeza, Y., & Carrera, J. (2015). Dissolution patterns and mixing dynamics in unstable reactive flow. *Geophysical Research Letters*, 42(15), 6357–6364.

- <https://doi.org/10.1002/2015GL065036>
- Hilley, G. E., & Porder, S. (2008). A framework for predicting global silicate weathering and CO₂ drawdown rates over geologic time-scales. *Proceedings of the National Academy of Sciences*, *105*(44), 16855–16859. <https://doi.org/10.1073/pnas.0801462105>
- Hubbard, C. G., West, L. J., Odriguez-Blanco, J. D., & Shaw, S. (2014). Laboratory study of spectral induced polarization responses of magnetite-Fe²⁺ redox reactions in porous media. *Geophysics*, *79*(1), D21–D30.
- Huisman, J. A., Zimmermann, E., Esser, O., Haegel, F., Treichel, A., & Vereecken, H. (2016). Evaluation of a novel correction procedure to remove electrode impedance effects from broadband SIP measurements. *Journal of Applied Geophysics*, *135*, 466–473. <https://doi.org/10.1016/j.jappgeo.2015.11.008>
- Izumoto, S., Huisman, J. A., Wu, Y., & Vereecken, H. (2019). Effect of solute concentration on the spectral induced polarization response of calcite precipitation. *Geophysical Journal International*, *220*, 1187–1196. <https://doi.org/10.1093/gji/ggz515>
- Jiménez-Martínez, J., Anna, P. De, Tabuteau, H., Turuban, R., Borgne, T. Le, & Méheust, Y. (2015). Pore-scale mechanisms for the enhancement of mixing in unsaturated porous media and implications for chemical reactions. *Geophysical Research Letters*, *42*(13), 5316–5324. <https://doi.org/10.1002/2015GL064513>
- Jiménez-Martínez, J., Le Borgne, T., Tabuteau, H., & Méheust, Y. (2017). Impact of saturation on dispersion and mixing in porous media: Photobleaching pulse injection experiments and shear-enhanced mixing model. *Water Resources Research*, *53*(2), 1457–1472. <https://doi.org/10.1002/2016WR019849>
- Karadimitriou, N. K., & Hassanizadeh, S. M. (2012). A Review of Micromodels and Their Use in Two-Phase Flow Studies. *Vadose Zone Journal*, *11*(3), vzj2011.0072. <https://doi.org/10.2136/vzj2011.0072>
- Kemna, A., Binley, A., Cassiani, G., Niederleithinger, E., Revil, A., Slater, L., ... Zimmermann, E. (2012). An overview of the spectral induced polarization method for near-surface applications. *Near Surface Geophysics*, *10*, 453–468. <https://doi.org/10.3997/1873-0604.2012027>
- Kim, D. H., Mahabadi, N., Jang, J., & Paassen, L. A. (2020). Assessing the Kinetics and Pore-Scale Characteristics of Biological Calcium Carbonate Precipitation in Porous Media using a Microfluidic Chip Experiment. *Water Resources Research*, *56*(2), 1–16. <https://doi.org/10.1029/2019WR025420>

References

- Koch, K., Kemna, A., Irving, J., & Holliger, K. (2011). Impact of changes in grain size and pore space on the hydraulic conductivity and spectral induced polarization response of sand. *Hydrology and Earth System Sciences*, 15(6), 1785–1794. <https://doi.org/10.5194/hess-15-1785-2011>
- Kolbe, T., de Dreuzy, J.-R., Abbott, B. W., Aquilina, L., Babey, T., Green, C. T., ... Pinay, G. (2019). Stratification of reactivity determines nitrate removal in groundwater. *Proceedings of the National Academy of Sciences*, 116(7), 2494–2499. <https://doi.org/10.1073/pnas.1816892116>
- Koo, Y. E. L., & Kopelman, R. (1991). Space-and time-resolved diffusion-limited binary reaction kinetics in capillaries: experimental observation of segregation, anomalous exponents, and depletion zone. *Journal of Statistical Physics*, 65(5–6), 893–918. <https://doi.org/10.1007/BF01049588>
- Lamb, H. (1906). *Hydrodynamics* (3rd editio). Cambridge: Chambridge University Press.
- Larralde, H., Araujo, M., Havlin, S., & Stanley, H. E. (1992). Reaction front for $A + B \rightarrow C$ diffusion-reaction systems with initially separated reactants. *Physical Review A*, 46(2), 855–859. <https://doi.org/10.1103/PhysRevA.46.855>
- Leroy, P., Revil, A., Kemna, A., Cosenza, P., & Ghorbani, A. (2008). Complex conductivity of water-saturated packs of glass beads. *Journal of Colloid and Interface Science*, 321(1), 103–117. <https://doi.org/10.1016/j.jcis.2007.12.031>
- Leroy, P., Li, S., Jougnot, D., Revil, A., & Wu, Y. (2017). Modeling the evolution of complex conductivity during calcite precipitation on glass beads. *Geophysical Journal International*, 209(1), ggx001. <https://doi.org/10.1093/gji/ggx001>
- Lesmes, D. P., & Frye, K. M. (2001). Influence of pore fluid chemistry on the complex conductivity and induced polarization responses of Berea sandstone. *Journal of Geophysical Research: Solid Earth*, 106(B3), 4079–4090. <https://doi.org/10.1029/2000JB900392>
- Lester, D. R., Trefry, M. G., & Metcalfe, G. (2016). Chaotic advection at the pore scale: Mechanisms, upscaling and implications for macroscopic transport. *Advances in Water Resources*, 97, 175–192. <https://doi.org/10.1016/j.advwatres.2016.09.007>
- Lester, D. R., Metcalfe, G., & Trefry, M. G. (2013). Is Chaotic Advection Inherent to Porous Media Flow? *Physical Review Letters*, 111(17), 174101. <https://doi.org/10.1103/PhysRevLett.111.174101>
- Li, S., Leroy, P., Heberling, F., Devau, N., Jougnot, D., & Chiaberge, C. (2016). Influence of surface conductivity on the apparent zeta potential of calcite. *Journal of Colloid and Interface Science*, 468, 262–275. <https://doi.org/10.1016/j.jcis.2016.01.075>

- Liang, L., Sullivan, A. B., West, O. R., Moline, G. R., & Kamolpornwijit, W. (2003). Predicting the precipitation of mineral phases in permeable reactive barriers. *Environmental Engineering Science*, 20(6). <https://doi.org/10.1089/109287503770736159>
- Lyklema, J., Dukhin, S. S., & Shilov, V. N. (1983). The relaxation of the double layer around colloidal particles and the low-frequency dielectric dispersion. *Journal of Electroanalytical Chemistry and Interfacial Electrochemistry*, 143, 1–21. [https://doi.org/10.1016/S0022-0728\(83\)80251-4](https://doi.org/10.1016/S0022-0728(83)80251-4)
- Al Mahrouqi, D., Vinogradov, J., & Jackson, M. D. (2017). Zeta potential of artificial and natural calcite in aqueous solution. *Advances in Colloid and Interface Science*, 240, 60–76. <https://doi.org/10.1016/j.cis.2016.12.006>
- Marshall, D. J., & Madden, T. R. (1959). Induced polarization, a case study of its cause. *Geophysics*, 24(4), 790–816. <https://doi.org/10.1190/1.1438659>
- Matsumoto, R., & Matsuo, R. (2015). Measurement of local chemical reaction rate in a microchannel by using luminol chemiluminescence. *Experimental Thermal and Fluid Science*, 67, 88–95. <https://doi.org/10.1016/j.exptthermflusci.2014.11.013>
- Mazzeo, B. A. (2009). Parasitic capacitance influence of potential-sensing electrodes on four-electrode liquid impedance measurements. *Journal of Applied Physics*, 105(9), 094106. <https://doi.org/10.1063/1.3124365>
- McClain, M. E., Boyer, E. W., Dent, C. L., Gergel, S. E., Grimm, N. B., Groffman, P. M., ... Pinay, G. (2003). Biogeochemical Hot Spots and Hot Moments at the Interface of Terrestrial and Aquatic Ecosystems. *Ecosystems*, 6(4), 301–312. <https://doi.org/10.1007/s10021-003-0161-9>
- Mellage, A., Smeaton, C. M., Furman, A., Atekwana, E. A., Rezanezhad, F., & Van Cappellen, P. (2018). Linking Spectral Induced Polarization (SIP) and Subsurface Microbial Processes: Results from Sand Column Incubation Experiments. *Environmental Science & Technology*, 52(4), 2081–2090. <https://doi.org/10.1021/acs.est.7b04420>
- Merriam, J. B. (2007). Induced polarization and surface electrochemistry. *Geophysics*, 72(4), 157–166. <https://doi.org/10.1190/1.2732554>
- Mewafy, F. M., Werkema Jr., D. D., Atekwana, E. A., Slater, L. D., Abdel Aal, G., Revil, A., & Ntarlagiannis, D. (2013). Evidence that bio-metallic mineral precipitation enhances the complex conductivity response at a hydrocarbon contaminated site. *Journal of Applied Geophysics*, 98, 113–123. <https://doi.org/10.1016/j.jappgeo.2013.08.011>
- Montes-Hernandez, G., Findling, N., & Renard, F. (2016). Dissolution-precipitation reactions controlling fast formation of dolomite under hydrothermal conditions. *Applied Geochemistry*, 73,

References

- 169–177. <https://doi.org/10.1016/j.apgeochem.2016.08.011>
- Morse, J. W., Arvidson, R. S., & Lüttge, A. (2007). Calcium carbonate formation and dissolution. *Chemical Reviews*, *107*(2), 342–381. <https://doi.org/10.1021/cr050358j>
- Mujah, D., Shahin, M. A., & Cheng, L. (2017). State-of-the-art review of biocementation by microbially induced calcite precipitation (MICP) for soil stabilization. *Geomicrobiology Journal*, *34*(6), 524–537. <https://doi.org/10.1080/01490451.2016.1225866>
- Ntarlagiannis, D., Williams, K. H., Slater, L., & Hubbard, S. (2005). Low-frequency electrical response to microbial induced sulfide precipitation. *Journal of Geophysical Research*, *110*, G02009. <https://doi.org/10.1029/2005JG000024>
- Ntarlagiannis, D., Yee, N., & Slater, L. (2005). On the low-frequency electrical polarization of bacterial cells in sands. *Geophysical Research Letters*, *32*, L24402. <https://doi.org/10.1029/2005GL024751>
- Ntarlagiannis, D., Doherty, R., & Williams, K. H. (2010). Spectral induced polarization signatures of abiotic FeS precipitation. *Geophysics*, *75*(4), F127–F133. <https://doi.org/10.1190/1.3467759>
- Park, S. H., Parus, S., Kopelman, R., & Taitelbaum, H. (2001). Gel-free experiments of reaction-diffusion front kinetics. *Physical Review E*, *64*(5), 055102. <https://doi.org/10.1103/PhysRevE.64.055102>
- Parkhurst, D. L., & Appelo, C. A. J. (2013). *Description of input and examples for PHREEQC Version 3 — a computer program for speciation, batch-reaction, one-dimensional transport, and inverse geochemical calculations. U.S. Geological Survey Techniques and Methods, book 6, chapter A43, 497 p.* [https://doi.org/10.1016/0029-6554\(94\)90020-5](https://doi.org/10.1016/0029-6554(94)90020-5)
- Pavelic, P., Dillon, P. J., Barry, K. E., Vanderzalm, J. L., Correll, R. L., & Rinck-Pfeiffer, S. M. (2007). Water quality effects on clogging rates during reclaimed water ASR in a carbonate aquifer. *Journal of Hydrology*, *334*(1–2), 1–16. <https://doi.org/10.1016/j.jhydrol.2006.08.009>
- Phillips, A. J., Cunningham, A. B., Gerlach, R., Hiebert, R., Hwang, C., Lomans, B. P., ... Spangler, L. (2016). Fracture sealing with microbially-induced calcium carbonate precipitation: a field study. *Environmental Science and Technology*, *50*, 4111–4117. <https://doi.org/10.1021/acs.est.5b05559>
- Pilawski, T. (2019). *On the impact of bacteria on spectral induced polarization measurements.*
- Placencia-gómez, E., Slater, L., Ntarlagiannis, D., & Binley, A. (2013). Laboratory SIP signatures associated with oxidation of disseminated metal sulfides. *Journal of Contaminant Hydrology*, *148*, 25–38. <https://doi.org/10.1016/j.jconhyd.2013.02.007>
- Prodan, C., Mayo, F., Claycomb, J. R., Miller, J. H., & Benedik, M. J. (2004). Low-frequency, low-field dielectric spectroscopy of living cell suspensions. *Journal of Applied Physics*, *95*(7), 3754–

3756. <https://doi.org/10.1063/1.1649455>
- Purgstaller, B., Goetschl, K. E., Mavromatis, V., & Dietzel, M. (2019). Solubility investigations in the amorphous calcium magnesium carbonate system. *CrystEngComm*, *21*(1), 155–164. <https://doi.org/10.1039/C8CE01596A>
- Ranz, W. E. (1979). Applications of a stretch model to mixing, diffusion, and reaction in laminar and turbulent flows. *AIChE Journal*, *25*(1), 41–47. <https://doi.org/10.1002/aic.690250105>
- Regenspurg, S., Feldbusch, E., Byrne, J., Deon, F., Driba, D. L., Henninges, J., ... Schubert, C. (2015). Mineral precipitation during production of geothermal fluid from a Permian Rotliegend reservoir. *Geothermics*, *54*, 122–135. <https://doi.org/10.1016/j.geothermics.2015.01.003>
- Revil, A., & Skold, M. (2011). Salinity dependence of spectral induced polarization in sands and sandstones. *Geophysical Journal International*, *187*(2), 813–824. <https://doi.org/10.1111/j.1365-246X.2011.05181.x>
- Revil, A., Atekwana, E., Zhang, C., Jardani, A., & Smith, S. (2012). A new model for the spectral induced polarization signature of bacterial growth in porous media. *Water Resources Research*, *48*(9), W09545. <https://doi.org/10.1029/2012WR011965>
- Rodriguez-Navarro, C., Cara, A. B., Elert, K., & Putnis, C. V. (2016). Direct nanoscale imaging reveals the growth of calcite crystals via amorphous nanoparticles. *Crystal Growth & Design*, *16*, 1850–1860. <https://doi.org/10.1021/acs.cgd.5b01180>
- Rolle, M., & Le Borgne, T. (2019). Mixing and Reactive Fronts in the Subsurface. *Reviews in Mineralogy and Geochemistry*, *85*(1), 111–142. <https://doi.org/10.2138/rmg.2018.85.5>
- Rufai, A., & Crawshaw, J. (2017). Micromodel observations of evaporative drying and salt deposition in porous media. *Physics of Fluids*, *29*(12), 126603. <https://doi.org/10.1063/1.5004246>
- Saneiyani, S., Ntarlagiannis, D., Ohan, J., Lee, J., Colwell, F., & Burns, S. (2019). Induced polarization as a monitoring tool for in-situ microbial induced carbonate precipitation (MICP) processes. *Ecological Engineering*, *127*, 36–47. <https://doi.org/10.1016/j.ecoleng.2018.11.010>
- Saneiyani, S., Ntarlagiannis, D., & Colwell, F. (2020). Complex conductivity signatures of microbial induced calcite precipitation, field and laboratory scales. *Geophysical Journal International*, 51–87. <https://doi.org/10.1093/gji/ggaa510>
- Saneiyani, S., Ntarlagiannis, D., Werkema, D. D., & Ustra, A. (2018). Geophysical methods for monitoring soil stabilization processes. *Journal of Applied Geophysics*, *148*, 234–244. <https://doi.org/10.1016/j.jappgeo.2017.12.008>
- Schuszter, G., Brau, F., & De Wit, A. (2016). Calcium Carbonate Mineralization in a Confined

References

- Geometry. *Environmental Science & Technology Letters*, 3(4), 156–159. <https://doi.org/10.1021/acs.estlett.6b00074>
- Schwarz, G. (1962). A theory of the low-frequency dielectric dispersion of colloidal particles in electrolyte solution. *The Journal of Physical Chemistry*, 66(12), 2636–2642. <https://doi.org/10.1021/j100818a067>
- Sen, P. N., Scala, C., & Cohen, M. H. (1981). A self-similar model for sedimentary rocks with application to the dielectric constant of fused glass beads. *Geophysics*, 46(5), 781–795. <https://doi.org/10.1190/1.1441215>
- Slater, L. D., Ntarlagiannis, D., & Wishart, D. (2006). On the relationship between induced polarization and surface area in metal-sand and clay-sand mixtures. *Geophysics*, 71(2), A1–A5. <https://doi.org/10.1190/1.2187707>
- Slater, L. D., Choi, J., & Wu, Y. (2005). Electrical properties of iron-sand columns: Implications for induced polarization investigation and performance monitoring of iron-wall barriers. *Geophysics*, 70(4), G87–G94.
- Slater, L., Ntarlagiannis, D., Personna, Y. R., & Hubbard, S. (2007). Pore-scale spectral induced polarization signatures associated with FeS biomineral transformations. *Geophysical Research Letters*, 34, L21404. <https://doi.org/10.1029/2007GL031840>
- Slater, L., & Sandberg, S. (2000). Resistivity and induced polarization monitoring of salt transport under natural hydraulic gradients. *GEOPHYSICS*, 65(2), 408–420. <https://doi.org/10.1190/1.1444735>
- Son, K., Brumley, D. R., & Stocker, R. (2015). Live from under the lens: exploring microbial motility with dynamic imaging and microfluidics. *Nature Reviews Microbiology*, 13(12), 761–775. <https://doi.org/10.1038/nrmicro3567>
- Tanaka, M., & Sato, M. (2007). Microwave heating of water, ice, and saline solution: Molecular dynamics study. *The Journal of Chemical Physics*, 126(3), 034509. <https://doi.org/10.1063/1.2403870>
- Tarasov, A., & Titov, K. (2013). On the use of the Cole–Cole equations in spectral induced polarization. *Geophysical Journal International*, 195(1), 352–356. <https://doi.org/10.1093/gji/ggt251>
- Uchida, S., Satoh, Y., Yamashiro, N., & Satoh, T. (2004). Determination of Hydrogen Peroxide in Water by Chemiluminescence Detection, (II). *Journal of Nuclear Science and Technology*, 41(9), 898–906. <https://doi.org/10.1080/18811248.2004.9715562>
- Valocchi, A. J., Bolster, D., & Werth, C. J. (2019). Mixing-Limited Reactions in Porous Media. *Transport in Porous Media*, 130(1), 157–182. <https://doi.org/10.1007/s11242-018-1204-1>

- Villiermaux, E. (2019). Mixing Versus Stirring. *Annual Review of Fluid Mechanics*, 51(1), 245–273. <https://doi.org/10.1146/annurev-fluid-010518-040306>
- Weller, A., & Slater, L. (2012). Salinity dependence of complex conductivity of unconsolidated and consolidated materials: Comparisons with electrical double layer models. *Geophysics*, 77(5), D185–D198. <https://doi.org/10.1190/geo2012-0030.1>
- White, F. M. (1998). *Fluid Mechanics* (4th ed.). Boston, Ma, Et Al.: McGraw-Hill Education.
- Wolthers, M., Charlet, L., & Van Cappellen, P. (2008). The surface chemistry of divalent metal carbonate minerals; a critical assessment of surface charge and potential data using the charge distribution multi-site ion complexation model. *American Journal of Science*, 308(8), 905–941. <https://doi.org/10.2475/08.2008.02>
- Wu, Y., Hubbard, S., Williams, K. H., & Ajo-Franklin, J. (2010). On the complex conductivity signatures of calcite precipitation. *Journal of Geophysical Research: Biogeosciences*, 115(G2), G00G04. <https://doi.org/10.1029/2009JG001129>
- Wu, Y., Slater, L. D., & Korte, N. (2005). Effect of precipitation on low frequency electrical properties of zerovalent iron columns. *Environmental Science and Technology*, 39(23), 9197–9204.
- Wu, Y., Ajo-Franklin, J. B., Spycher, N., Hubbard, S. S., Zhang, G., Williams, K. H., ... Smith, R. (2011). Geophysical monitoring and reactive transport modeling of ureolytically-driven calcium carbonate precipitation. *Geochemical Transactions*, 12(7). <https://doi.org/10.1186/1467-4866-12-7>
- Yang, H., Chai, S., Zhang, Y., & Ma, Y. (2016). A study on the influence of sodium carbonate concentration on the synthesis of high Mg calcites. *CrystEngComm*, 18(1), 157–163. <https://doi.org/10.1039/C5CE01821H>
- Zhang, C., Dehoff, K., Hess, N., Oostrom, M., Wietsma, T. W., Valocchi, A. J., ... Werth, C. J. (2010). Pore-Scale Study of Transverse Mixing Induced CaCO₃ Precipitation and Permeability Reduction in a Model Subsurface Sedimentary System. *Environmental Science & Technology*, 44(20), 7833–7838. <https://doi.org/10.1021/es1019788>
- Zhang, C., Ntarlagiannis, D., Slater, L., & Doherty, R. (2010). Monitoring microbial sulfate reduction in porous media using multipurpose electrodes. *Journal of Geophysical Research*, 115, 1–11. <https://doi.org/10.1029/2009JG001157>
- Zhang, C., Slater, L., Redden, G., Fujita, Y., Johnson, T., & Fox, D. (2012). Spectral Induced Polarization Signatures of Hydroxide Adsorption and Mineral Precipitation in Porous Media. *Environmental Science & Technology*, 46(8), 4357–4364. <https://doi.org/10.1021/es204404e>

References

- Zhang, C., Slater, L., & Prodan, C. (2013). Complex Dielectric Properties of Sulfate-Reducing Bacteria Suspensions. *Geomicrobiology Journal*, 30(6), 490–496. <https://doi.org/10.1080/01490451.2012.719997>
- Zhang, C., Revil, A., Fujita, Y., Munakata-marr, J., & Redden, G. (2014). Quadrature conductivity: A quantitative indicator of bacterial abundance in porous media. *Geophysics*, 79(6), D363–D375.
- Zimmermann, E., Kemna, A., Berwix, J., Glaas, W., Münch, H. M., & Huisman, J. A. (2008). A high-accuracy impedance spectrometer for measuring sediments with low polarizability. *Measurement Science and Technology*, 19, 1–9. <https://doi.org/10.1088/0957-0233/19/10/105603>
- Zoback, M. D., & Gorelick, S. M. (2012). Earthquake triggering and large-scale geologic storage of carbon dioxide. *Proceedings of the National Academy of Sciences*, 109(26), 10164–10168. <https://doi.org/10.1073/pnas.1202473109>

Band / Volume 554

Characterisation of the effect of redox potential on the emission of greenhouse gases using wireless sensing techniques

J. Wang (2021), XIV, 104 pp

ISBN: 978-3-95806-581-9

Band / Volume 555

Stability assessment of variably saturated hillslopes using coupled hydromechanical models

S. Moradi (2021), xxxii, 123 pp

ISBN: 978-3-95806-583-3

Band / Volume 556

Catalytic-doping of Silicon Alloys for the Use in Silicon Heterojunction Solar Cells

Y. Liu (2021), 126 pp

ISBN: 978-3-95806-591-8

Band / Volume 557

Formation of highly oxygenated organic molecules from α -pinene photochemistry

S. Kang (2021), xvii, 156 pp

ISBN: 978-3-95806-596-3

Band / Volume 558

Synthese von Cr_2AlC MAX-Phasen Kompositen und Bestimmung ihrer oxidativen Eigenschaften

T. Go (2021), ii, 119 pp

ISBN: 978-3-95806-598-7

Band / Volume 559

Distribution of Relaxation Times for Analysis of Solid Oxide Fuel Cell Stacks

K. Fitzek (2021), 237 pp

ISBN: 978-3-95806-599-4

Band / Volume 560

Machine Learning in Modeling of the Dynamics of Polymer Electrolyte Fuel Cells

W. Zou (2021), vii, 139 pp

ISBN: 978-3-95806-601-4

Band / Volume 561

Introduction Strategies for Hydrogen Infrastructure

S. Cerniauskas (2021), viii, 179 pp

ISBN: 978-3-95806-602-1

Band / Volume 562

Noble Metal Coated Porous Transport Layers for Polymer Electrolyte Membrane Water Electrolysis

C. Liu (2021), 139 pp

ISBN: 978-3-95806-603-8

Band / Volume 563

Modeling and Diagnosis of the Stratospheric Circulation

E. J. Charlesworth (2021), v, 103, A2 pp

ISBN: 978-3-95806-605-2

Band / Volume 564

Potentialfeldmessungen zur Qualitätsbewertung von Bipolarplatten

M. Sietmann (2021), ix, 160 pp

ISBN: 978-3-95806-606-9

Band / Volume 565

Sequential and coupled inversion of time-lapse borehole GPR measurements for vadose zone model parameterization

Y. Yu (2022), XX, 121 pp

ISBN: 978-3-95806-607-6

Band / Volume 566

Cirrus clouds in the extratropical tropopause and lowermost stratosphere region

I. Bartolomé García (2022), iii, 155 pp

ISBN: 978-3-95806-610-6

Band / Volume 567

Stationary and Transient Behaviour of Polymer Electrolyte Fuel Cells

Y. Shi (2022), viii, 172 pp

ISBN: 978-3-95806-611-3

Band / Volume 568

14th Carolus Magnus Summer School on Plasma and Fusion Energy Physics

D. Reiser (Ed.), (2022), 207 pp

ISBN: 978-3-95806-613-7

Band / Volume 569

Spectral induced polarization of calcite precipitation in porous media

S. Izumoto (2022), xviii, 106 pp

ISBN: 978-3-95806-614-4

Energie & Umwelt / Energy & Environment
Band / Volume 569
ISBN 978-3-95806-614-4